Inverse Design of Huygens' Metasurfaces for 2D and 3D Power Pattern Synthesis

by

Tianke Qiu

Submitted to the Graduate Faculty of
University of Manitoba in partial fulfilment
of the requirements for the degree of

Master of Science

Department of Electrical and Computer Engineering
University of Manitoba
Winnipeg, Manitoba, Canada

2022

Abstract

Electromagnetic (EM) metasurfaces are quasi two-dimensional structures that consist of artificial "atoms", typically referred to as meta-atoms. These meta-atoms, also known as unit cells, are small compared to the operational wavelength. The whole metasurface consists of many unit cells; thus, although the size of the unit cells is small compared to the wavelength of operation, the total size of the metasurface is a few wavelengths. Based on their properties, the unit cells can locally affect the amplitude, phase, and polarization of the EM wave that impinges on them. When properly designed and arranged, the accumulated effect of the unit cells allows the metasurface to alter the incident wave at will through transmission, reflection and absorption of the EM wave. Thus, EM metasurfaces can be used as a systematic means for beam shaping.

The design of a metasurface includes two main steps: macroscopic and microscopic design steps. The macroscopic design aims to determine the required surface properties of the unit cells, such as surface polarizabilities or surface susceptibilities, to support the desired field transformation. Once the macroscopic properties are determined, the microscopic design focuses on the practical design of the unit cells (which is typically copper trace design in microwave and mm-wave frequencies) to physically realize the required surface properties.

The work presented in this thesis focuses on the macroscopic design of metasurfaces, and the formulation is presented in terms of surface susceptibilities of metasurfaces. As will be seen, based on the generalized sheet transition conditions (GSTCs), the tangential fields on the two sides of the metasurface are required to calculate the required surface susceptibility values to support the desired field transformation. In practice, these tangential fields, especially the transmitted fields, might not be directly known. For example, one can be asked to design a metasurface to transform a given incident field (e.g., a plane wave or the field of a horn antenna) to a desired far-field power pattern. In this case, the known quantity is the desired power pattern in the far-field zone, and therefore the complex (magnitude and phase) tangential field on the output side of the metasurface is not known. Thus, this

unknown tangential field, which supports the required power (magnitude-only) pattern, needs to be first determined for the metasurface design process.

To this end, an inversion algorithm based on the nonlinear conjugate-gradient (CG) method was previously developed to infer the tangential fields on the transmitted side of the metasurface from the desired power pattern with some additional side constraints such as Love's equivalence principle and the local power conservation constraint. This thesis builds on this prior work and extends it in the following ways. Firstly, it provides an analytical expression for the nonlinear CG step length. This was not previously available and thus the inversion algorithm required an *ad hoc* choice for the step length. In this thesis, the analytical expression for the step length is derived. This will make the CG algorithm automated, and also drastically decreases the computational time. In addition, the nonlinear CG requires that the step length changes at each iteration of the algorithm. The *ad hoc* step length choice, previously used for this inverse design algorithm, was not able to support a changing step length as a function of iteration.

Secondly, the prior work on this inversion algorithm was for the two-dimensional (2D) case which required the metasurface to be fully periodic in one direction. In this thesis, this inversion frame is extended to the three-dimensional (3D) configuration, allowing the designed metasurface to spatially vary along the two orthogonal directions along the metasurface. Based on this 3D implementation, the user can provide the desired power patterns on two perpendicular far-field cuts along with the incident field impinging on the metasurface, and then the inversion algorithm finds the macroscopic properties of the metasurface to achieve this transformation. Thirdly, a brief discussion on the existence of the surface waves in the formulation is presented which can assist with satisfying the local power conservation constraint in the design of passive and lossless metasurfaces.

Contributions

This thesis includes the following contributions in the form, of conference and submitted journal papers.

Refereed Journal Papers

1. **T. Qiu**, M. Phaneuf, and P. Mojabi, "Inverse Metasurface Design from 3D Desired Power Patterns on Two Cuts," Submitted, 2022.

   – Tianke Qiu: Manuscript preparation, development of the 3D inversion algorithm and metasurface design, and simulation in Ansys HFSS.

   – Mario Phaneuf: Verification of the existence of the surface waves in the inverse source formulation.

   – Puyan Mojabi: Advisory role

Refereed Conference Papers

1. **T. Qiu**, Trevor Brown, and P. Mojabi, "Choice of Optimization Parameters in an Inverse Metasurface Design Algorithm," *IEEE International Symposium on Antennas and Propagation and USNC-URSI Radio Science Meeting*, pp.1-2, Singapore, 2021.

   – Tianke Qiu: Manuscript preparation, derivation and implementation of the analytical step length, discussion of the weighting parameters, and Ansys HFSS simulation.

   – Trevor Brown: 2D inversion algorithm for metasurface design (without the analytical step length)

   – Puyan Mojabi: Advisory role

2. M. Phaneuf, **T. Qiu**, and P. Mojabi, "On the Importance of the Love's Condition for Inverse Equivalent-Source Metasurface Design," *IEEE International Symposium*

on Antennas and Propagation and USNC-URSI Radio Science Meeting, pp. 1-2, Singapore, 2021.

- Mario Phaneuf: Manuscript preparation and metasurface design
- Tianke Qiu: 2D inversion algorithm for metasurface design with the analytical step length
- Puyan Mojabi: Advisory role

Acknowledgements

First and foremost, I would like to express my sincere gratitude to my supervisor Prof. Puyan Mojabi, for his patience, enthusiasm and dedication. The completion of this work is based on his constant help and inspiration. He has been a remarkable mentor for me over the two years of my graduate studies.

I would like to acknowledge Prof. Joe LoVetri and Prof. Amine Mezghani for examining this thesis and their valuable comments.

Also, I would like to thank all Puyan's group members, in particular Dr. Trevor Brown, for all the discussions and collaborations. It has been a pleasure working with them.

Lastly, I want to give my special thank to my families for their moral support over the years.

Table of Contents

List of Abbreviations

Abbreviation	Description
EM	Electromagnetic
GSTCs	Generalized sheet transition conditions
CG	Conjugate-gradient
2D	Two-dimensional
3D	Three-dimensional
EBG	Electromagnetic band gap
PBG	Photonic band gap
LPC	Local power conservation
TV	Total variation
TE	Transverse electric
TM	Transverse magnetic
ROI	Region of interest
FF	Far-field
PEC	Perfect electric conductor
PMC	Perfect magnetic conductor

List of Symbols

Symbol	Description
$\boldsymbol{E}$	Electric field
$\boldsymbol{H}$	Magnetic field
$\boldsymbol{P}^e$	Electric polarization
$\boldsymbol{P}^m$	Magnetic polarization
$\boldsymbol{D}$	Electric flux density
$\boldsymbol{B}$	Magnetic flux density
ε_0	Free space permittivity
μ_0	Free space permeability
j	Imaginary unit ($j^2 = -1$)
$\boldsymbol{\nabla}$	Gradient operator
Δ	Difference
$\overline{\overline{\chi}}$	Surface susceptibility tensor
c_0	Free space speed of light
η_0	Free space characteristic impedance
av	Average
k_0	Free space wavenumber
$\boldsymbol{S}$	Poynting vector
$\boldsymbol{\nabla}\cdot$	Divergence operator
$\boldsymbol{J}$	Electric current density
$\boldsymbol{M}$	Magnetic current density
$\langle\cdot,\cdot\rangle$	Inner product operator
$\|\cdot\|$	L_2-norm operator
$\|\cdot\|$	absolute value operator

Chapter 1

Introduction

The will to control electromagnetic (EM) waves was of significant interest since the establishment of the Maxwell's equations. For example, in 1967, Dr. Veselago theoretically analyzed the effect of having negative values for permittivity (ϵ) and permeability (μ) simultaneously for a given medium [1]. (This paper was translated into English in 1968.) This property will then result in negative refraction index. Several counter-intuitive phenomena, like the reversed Doppler effect and reversed Cherenkov radiation, are then introduced based on the negative refraction index [1].

In general, tailoring EM waves can be achieved by manipulating ϵ and μ of the material. With limited variety of ϵ and μ offered by natural materials, the quest for implementing negative values for ϵ and μ was pursued within the artificial material realm. The artificial materials that possess this property were then called "negative-index materials" or "left-handed materials". The physical form of this surreal artificial material was proven plausible when Dr. Pendry suggested that at certain operating frequencies, ϵ and μ could be adjusted freely using resonance structures proposed in [2, 3]. This artificial material was then experimentally verified in [4]. The term "metamaterials" was introduced by Dr. Smith and his colleagues to emphasize the unique aspect of negative-index materials as compared to

other composite materials; this was done by using the prefix "meta" ($\mu\epsilon\tau\acute{\alpha}$) which means "beyond" in Greek [5].

As the research develops, the term "metamaterials" now refers to artificial materials that are designed to possess desired unusual characteristics. A metamaterial consists of many unit cells. These unit cells consist of constitutive elements located in a host medium that collectively govern the EM properties of the metamaterial. Although the term "metamatrials" have been loosely assigned to many artificial media, it should be emphasized that the proper definition of metamaterials requires that the size of each unit cell is small compared to the wavelength in the host medium, but not too small [5]. If the unit cell size is too small compared to the wavelength, we will be in the quasi-static region, and classic mixing formula can be applied to obtain the EM properties of the artificial material [6]. On the other hand, if the size of the unit cell is in the order of the wavelength, e.g., electromagnetic bandgap (EBG) or photonic bandgap (PBG) structures, then an effective medium cannot be defined [6].

While the potential of metamaterials is unlimited, their bulkiness has become one of the major disadvantages, resulting in the increased overall loss, weight, size, and difficulties in fabrication and implementation. To overcome this issue, physicists and engineers started to investigate and develop quasi-two-dimensional metamaterials, which are also known as metasurfaces. One of the pioneering works in this area was the work of Capasso and colleagues [7] (published in 2011) that introduced the generalized laws of reflection and refraction over a surface. Metasurfaces can be utilized to tailor reflection [8], transmission [9], absorption [10] of EM waves, or a combination thereof. Herein, we focus on metasurfaces that are used to tailor the transmission of EM waves. To manipulate electric and magnetic fields at the metasurface boundary, appropriate electric and magnetic polarization currents need to be induced on the metasurface [11]. Due to taking advantage of both electric and magnetic polarization currents, these metasurfaces are often referred to as *Huygens' meta-*

surfaces [12]. These metasurfaces, which create collocated electric and magnetic responses when illuminated by an EM wave [8, 13], are the focus of this thesis. The reason behind their names (Huygens) comes from Huygens' principle, named after Dutch scientist Christiaan Huygens, which enables us to predict a wavefront from a set of fictitious electric and magnetic current sources [14].

Before the development of electromagnetic metasurfaces, thin structures have already been used to manipulate EM waves with specific functionalities. For example, conventional frequency selective surfaces are mainly used for filtering purposes, and reflectarrays are designed as a flat counterpart of traditional parabolic reflectors. Although these structures may *loosely* be referred to as metasurfaces, they are not exactly metasurfaces. As noted in [6], the dimension of the unit cells need to be small compared to the wavelength for the structure to be qualified as a metasurface. When this condition is not satisfied in conventional frequency selective surfaces and reflectarrays, they cannot be categorized under metasurfaces. However, it is important to note that these precursors played important roles in the development of metasurfaces. For example, the reconfigurability techniques considered in reflectarrays can be transferred to reconfigurable metasurfaces.

Metasurfaces often consist of an ultra thin dielectric structure with subwavelength (metallic) inclusions that could locally affect the amplitude, phase, and polarization of the incident wave. The accumulated effect of these subwavelength inclusions can create functionalities which go beyond what can be achieved with natural thin materials (e.g., generalized Snell's law [7]). By tuning each unit cell individually, this complex inhomogeneous artificial material could systematically control the EM wave through transmission, reflection and absorption, resulting in various applications. For example, many metasurfaces are designed to perform polarization transformation. In [15], linearly polarized incident waves can be transformed into circularly polarized waves. Wavefront manipulation could also be achieved by metasurfaces [9] for creating desired near-field or far-field responses. With the

use of active and nonlinear components, these metasurfaces can be further improved with switching and tuning abilities [16]. The recent studies of space-time metasurfaces [17] provided another level of control for EM waves. Space-time metasurfaces utilize both temporal and spatial modulation of the subwavelength inclusions. In this thesis, we only consider the spatial modulations of their subwavelength inclusions (i.e., no temporal modulation is employed), and therefore our focus is in the domain of spatially-modulated metasurfaces. In addition, spatially-modulated metasurfaces can be designed in two general ways. In the first approach, the subwavelength elements are tiny scatterers. This type of metasurfaces are sometimes referred as *metafilms* [18], and is perhaps the most common form of implementation. In the second approach, the subwavelength elements are tiny apertures on a sheet. This form is sometimes referred to as *metascreens* [6]. In this thesis, the focus is on metafilms.

Although different techniques are used for different applications, the design of these metasurfaces are all based on their homogenized behaviour (effective medium concept) and thus, they follow the same rule locally at each unit cell. Note that the effective medium concept can now include extra features such as magneto-electric coupling (bianisotropy) to explain the exotic wave transformation enabled by these metasurfaces. The macroscopic design of metasurfaces is focused on determining their effective surface parameters, which relies on the boundary conditions called the generalized sheet transition conditions (GSTCs). These boundary conditions were first studies in [19] and three effective models were developed for representing the GSTCs as followed:

- The polarizability model [20]
- The impedance model [13]
- The susceptibility model [21]

These models are related to each other. (For example, see [22,23] for the equations regarding

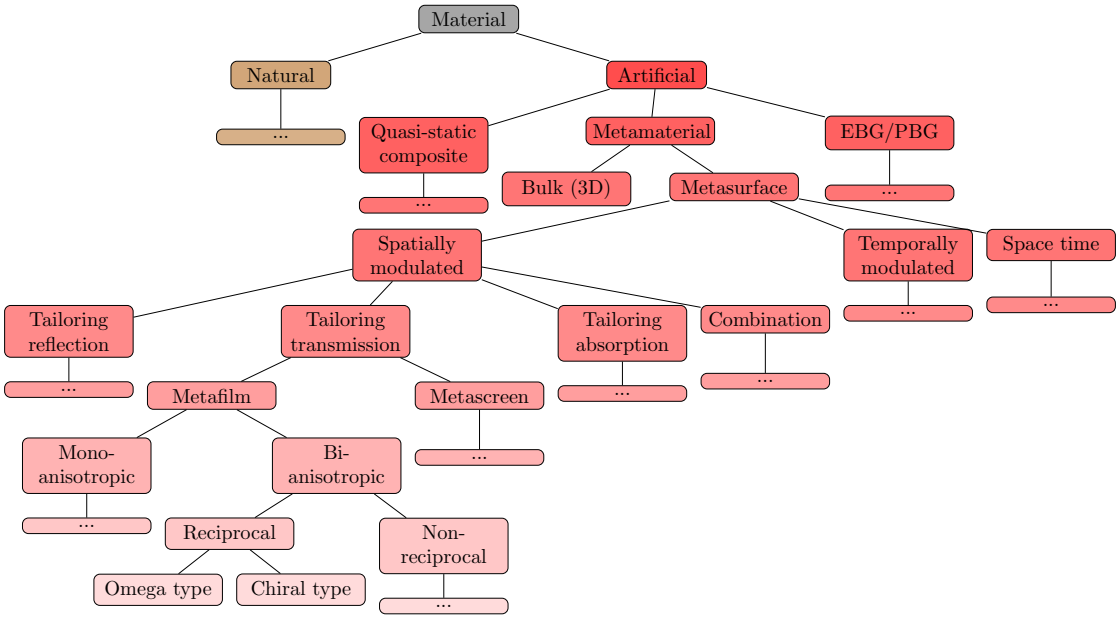

Fig. 1.1: A flowchart representing some of the classifications used in this thesis. The early part of this flowchart is based on a flowchart shown in [5].

their equivalency.) The susceptibility model is adopted in this thesis among these three effectively equivalent models, and the details of this model will be demonstrated later in the next chapter. As will be seen, once all the tangential components of the EM fields on both sides of the metasurface are known, the GSTCs could be applied to acquire surface susceptibilities, and hence the macroscopic design aspect is completed. On the other hand, the microscopic design of the metasurfaces focuses on realizing the aforementioned surface properties using practical physical implementation. The existing designs include Omega particles [24], Chiral particles [25], wire-loop structures [26], dogbone structures [27], etc.

In summary, Figure 1.1 presents some of the topics explained above in the flowchart format. In particular, it focuses more on what is relevant to this thesis. Some of the material presented in this flowchart is not yet explained, but will be explained as we go over some fundamentals of metasurfaces in the next chapter.

1.1 Objectives

As stated above, the macroscopic design of metasurfaces is rather straightforward if the incident, transmitted, and reflected EM fields are known over the boundaries of metasurfaces. However, for many practical problems, the information of these fields, especially transmitted fields, might not be directly available. For example, in antenna design applications, a complete far-field power pattern (phaseless), or certain far-field criteria, like main beam direction(s), half-power beamwidth(s), null direction(s), and others, might be provided. Therefore, typically, the designer has no access to the tangential complex (magnitude and phase) fields over the boundary of the metasurface. Thus, these tangential fields over the boundary of the metasurface need to be inferred from the provided performance criteria. This problem can therefore be regarded as an inverse problem. The work in [28] is one of the first works which address this problem within the inverse source framework. Later on, the local power conservation (LPC) constraint (originally introduced in [29] and to be discussed in the next chapter) was considered for the design of passive and lossless bianisotropic metasurfaces. The LPC constraint was incorporated into the inverse framework in [30]. Later, the inverse source framework was augmented by a total variation (TV) regularization term to favour smooth field variations on the surface of the metasurface for practical reasons [31].[1] (The collection of these inverse design works can be found in [32].) The objectives and the contributions of this thesis are the following.

– In the inverse source design framework explained above, a nonlinear conjugate-gradient (CG) method was used to solve the inverse problem. Due to the fact that the known quantity in this inverse problem is the desired *power* pattern[2], the inverse source

[1] As will be discussed in the next Chapter, the physical design (e.g., copper trace design) of metasurface unit cells is typically done under the assumption of periodicity. Thus, a smoother field variation on the metasurface will normally result in more convenient microscopic design. This is then typically referred to as quasi-periodicity assumption. Note that in general the inverse source framework can provide us with many solution due to the non-uniqueness associated with this inverse problem. Therefore, we need to single out a solution which is more appropriate from a practical point of view.

[2] From a practical point of view, a designer is mainly interested in power (magnitude-only) patterns rather

problem is nonlinear due to the absence of desired phase data. This requires a careful choice of the step length in the CG algorithm. Note that the unknown $\mathbf{x}$ at the kth iteration of the CG algorithm is updated as $\mathbf{x}_{k+1} = \mathbf{x}_k + \beta_k \mathbf{v}_k$ where $\mathbf{x}_k$ is the predicted unknown at the kth iteration, $\mathbf{v}_k$ is the CG direction along which we update $\mathbf{x}_k$. Finally, the step length β_k is the step length. In previous works explained above, an *ad hoc* approach has been used for the choice of β_k when the LPC constraint is utilized. Moreover, since the choice of the step length has been based on *ad hoc* methods, the CG algorithm uses a constant step length. However, the ideal choice is to minimize along the CG direction. In an attempt to make the above inverse source framework automated, this thesis derives an analytical expression for the step length in the presence of the LPC constraint and shows the result with this analytical expression.

– The previous inverse source approaches for the synthesis of desired power patterns have been based on the transverse electric (TE) or transverse magnetic (TM) assumptions. For this, the metasurface needs to be fully periodic in one direction, and can then have spatial modulation in the other direction. This thesis extends the inverse source framework to 3D scenarios where the desired power patterns are given on two perpendicular far-field cuts, such as desired power patterns on the E-plane and H-plane cuts.[3] This will then result in a metasurface that has spatial modulation in both directions along the surface of the metasurface.

1.2 Thesis Outline

This thesis is structured as follows.

than a complex field pattern (magnitude and phase).

[3] In [28], the authors consider the 3D problem, but they do not consider the LPC constraint, and also they do not perform any metasurface design based on their inversion.

Chapter 2 introduces a background of metasurface design. The generalized sheet transition conditions (GSTCs) based on the surface susceptibility model is presented. Then, a three-layer impedance sheet topology is provided as it could be used to represent the susceptibility model for full-wave simulation in Ansys HFSS. Each of the impedances within this three layer is either capacitive or inductive. These reactive impedances will then need to be implemented using appropriate copper traces. The implementation of the required impedances using copper traces is outside the scope of this thesis.

Chapter 3 presents an introduction to electromagnetic inversion. Since the electromagnetic inverse source framework is utilized in this thesis, the emphasis will be on the inverse source problem. Different components of the electromagnetic inverse source framework including the enforcement of the Love's condition is discussed. Since this chapter is presented using an operator notation, it will be applicable to both 2D TE and 2D TM as well as the 3D scenario.

Chapter 4 combines the topic discussed in Chapters 2 and 3 in an attempt to provide a step-by-step procedure for the inverse design of metasurfaces. For the sake of completeness of the thesis, all the steps are presented, but those who have been published before (e.g., see [32]) is presented without derivation. The main contribution of the author to this framework which is the analytical expression for the step length is presented with full derivation. Again, since the presentation in this chapter is based on the operator notation, it can be applied to 2D TE, 2D TM and 3D if the appropriate operator is utilized.

Chapter 5 presents full-wave simulation results using Ansys HFSS. Broadly speaking four categories of results are presented: (*i*) 2D TM, (*ii*) 2D TE, (*iii*) 3D, and (*iv*) 2D TE with cascaded metasurfaces. The 2D TE case with cascaded metasurfaces has been done in collaboration with another MSc student (Mr. Jayesh Gohel). In [31, 32], the 2D TE inversion with cascaded metasurfaces has been considered. The cascaded topology utilized herein differs from these two works in the sense that it takes into account multiple reflections

between the two metasurfaces as in [33]. The discussion on the 3D inversion includes a small part on the use of evanescent waves that has been done in collaboration with a PhD student (Mr. Mario Phaneuf).

Chapter 6 concludes this thesis, and provides directions for future work based on the lessons learned throughout this research and the new research directions currently being pursued by other research groups.

Chapter 2

Electromagnetic Metasurfaces Fundamentals

An EM metasurface is a quasi two-dimensional (2D) artificial material with sub-wavelength thickness that is formed by lattices of sub-wavelength inclusions known as meta-atoms with sub-wavelength spacing. Due to its sub-wavelength structure, a metasurface is modeled based on its surface properties as opposed to voluminal permittivity and permeability [34, 35]. The synthesis procedure includes deriving the appropriate surface properties, e.g., surface susceptibilities, based on the known incident, reflected, and transmitted EM fields, and realizing the required surface susceptibility values using suitable unit cells designs. (Each unit cell represents a meta-atom.) The emphasis of this chapter is on acquiring the surface properties, with a brief description of unit cell design procedure. The fundamentals of metasurfaces can be found in other works such as [36], [23].

2.1 The Generalized Sheet Transition Conditions

The behaviour of the metasurfaces is governed by the generalized sheet transition conditions (GSTCs) [21]. To understand this, let us begin by considering a material that when exposed

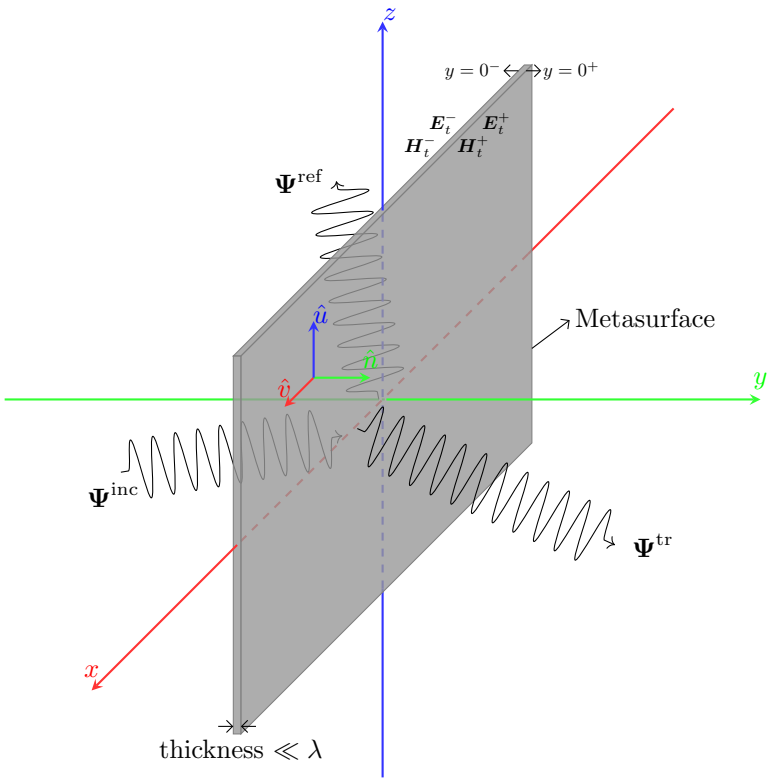

Fig. 2.1: Demonstration of a planar metasurface located on the xz plane that results in reflected field, $\boldsymbol{\Psi}_{\text{ref}}$, and transmitted field, $\boldsymbol{\Psi}_{\text{tr}}$, when illuminated by an incident field, $\boldsymbol{\Psi}_{\text{inc}}$. The unit vector that is normal to the metasurface, $\hat{n}$, is specified, along with the tangential components, $\hat{u}$ and $\hat{v}$.

to electric field $\boldsymbol{E}$ and magnetic field $\boldsymbol{H}$ will experience induced electric polarization $\boldsymbol{P}^{\text{e}}$ and induced magnetic polarization $\boldsymbol{P}^{\text{m}}$. The resulting electric and magnetic flux densities, denoted by $\boldsymbol{D}$ and $\boldsymbol{B}$ respectively, can be written as

$$\boldsymbol{D} = \varepsilon_0 \boldsymbol{E} + \boldsymbol{P}^{\text{e}}, \tag{2.1a}$$

$$\boldsymbol{B} = \mu_0 \boldsymbol{H} + \mu_0 \boldsymbol{P}^{\text{m}}, \tag{2.1b}$$

where ε_0 and μ_0 represent the free space permittivity and permeability respectively. Now consider a metasurface that lies on the xz plane, i.e., on the $y = 0$ plane as shown in Figure 2.1. The metasurface will have two sides: $y = 0^-$ and $y = 0^+$. If the metasurface

is illuminated by an incident field (e.g., from $y = 0^-$ side), surface electric and magnetic currents will be induced on the metasurface that can support EM field discontinuities across the surface. Consequently, a different field can be created on $y = 0^+$ face. According to the electromagnetic equivalence principle, this new field can create a new radiation pattern which is different than that of the incident field.

Assuming a time-dependency of $e^{j\omega t}$, where ω is the angular frequency and t denotes time, these discontinuities on passive metasurfaces[1] are described by the GSTCs, which can be written as [18, 21, 37, 38]

$$\hat{n} \times \Delta \boldsymbol{H} = j\omega \boldsymbol{P}_t^{\mathrm{e}} - \hat{n} \times \nabla_t P_n^{\mathrm{m}}, \tag{2.2a}$$

$$\Delta \boldsymbol{E} \times \hat{n} = j\omega \mu_0 \boldsymbol{P}_t^{\mathrm{m}} - \nabla_t (\frac{P_n^{\mathrm{e}}}{\varepsilon_0}) \times \hat{n}, \tag{2.2b}$$

where $\hat{n}$ represents the unit vector that is normal to the surface. For example, in our current example, $\hat{n} = \hat{y}$. The subscripts t and n denote the vector components that are tangential and normal to the surface, respectively. The vector cross product is represented by '$\times$', and '∇' represents the gradient operator.[2] The field difference $\Delta \boldsymbol{\Psi}$ is defined as

$$\Delta \boldsymbol{\Psi} \triangleq \boldsymbol{\Psi}^+ - \boldsymbol{\Psi}^-, \quad \text{where} \quad \boldsymbol{\Psi} = \{\boldsymbol{E}, \boldsymbol{H}\}. \tag{2.3}$$

where the superscripts $+$ and $-$ indicates the locations of the surface boundary that is in the direction of $\hat{n}$, and opposite to $\hat{n}$, respectively. For example, if $\hat{n}$ is set to $\hat{y}$ (as is the case in our example), the plus sign corresponds to locations on $y = 0^+$, and the minus sign corresponds to locations on $y = 0^-$. For simplicity, the normal components of the electric and magnetic polarization densities (i.e., P_n^{e} and P_n^{m}) are typically ignored as

[1] That is, no impressed currents exist on the metasurface.

[2] The operator '∇_t' is then the gradient vector with respect to the tangential components of the coordinate; in our example, we will then have $\nabla_t = \frac{\partial}{\partial x}\hat{x} + \frac{\partial}{\partial y}\hat{z}$.

justified in [21, 39]. The resulting GSTCs then read as

$$\hat{n} \times \Delta \boldsymbol{H} = j\omega \boldsymbol{P}_t^{\mathrm{e}}, \tag{2.4a}$$

$$\Delta \boldsymbol{E} \times \hat{n} = j\omega \mu_0 \boldsymbol{P}_t^{\mathrm{m}}. \tag{2.4b}$$

In the next section, we focus on how $\boldsymbol{P}_t^{\mathrm{m}}$ and $\boldsymbol{P}_t^{\mathrm{e}}$ are related to surface susceptibilities.

2.2 The Susceptibility Model

Before starting this session, let us consider the concept of *bianisotropy*. We already know that the electric polarization can be controlled by electric fields, and similarly the magnetic polarization can be controlled by magnetic fields. Bianisotropic materials will then generalize this concept in the sense that their electric polarization can be controlled by both electric and magnetic fields, and similarly their magnetic polarization can be controlled by both electric and magnetic fields. This is referred to as *magneto-electric coupling* [40].

The surface electric and magnetic polarization densities can be expressed using surface susceptibilities and averaged fields according to [18]. Considering a linear[3] bianisotropic metasurface, we have [21, 39]

$$\boldsymbol{P}_{t,s}^{e} = \varepsilon_0 \overline{\overline{\chi}}_{\mathrm{ee}} \cdot \boldsymbol{E}_{t,\mathrm{av}} + \frac{1}{c_0} \overline{\overline{\chi}}_{\mathrm{em}} \cdot \boldsymbol{H}_{t,\mathrm{av}}, \tag{2.5a}$$

$$\boldsymbol{P}_{t,s}^{m} = \overline{\overline{\chi}}_{\mathrm{mm}} \cdot \boldsymbol{H}_{t,\mathrm{av}} + \frac{1}{\eta_0} \overline{\overline{\chi}}_{\mathrm{me}} \cdot \boldsymbol{E}_{t,\mathrm{av}}, \tag{2.5b}$$

[3] Nonlinear metasurfaces are outside the scope of this thesis. To briefly explain them, let us refer to [22,41] which considers nonlinear metasurfaces with non-zero second-order susceptibilities. Based on that, the susceptibility can be represented by the first-order (linear component), denoted by $\overline{\overline{\chi}}^{(1)}$, and the second-order (nonlinear component), denoted by $\overline{\overline{\chi}}^{(2)}$ [22, 41]. Then, assuming a mono-isotropic metasurface for simplicity, the surface electric and magnetic polarization densities will be $P_{t,s}^{e} = \varepsilon_0 \chi_{\mathrm{ee}}^{(1)} E_{t,\mathrm{av}} + \varepsilon_0 \chi_{\mathrm{ee}}^{(2)} E_{t,\mathrm{av}}^2$ and $P_{t,s}^{m} = \chi_{\mathrm{mm}}^{(1)} H_{t,\mathrm{av}} + \chi_{\mathrm{mm}}^{(2)} H_{t,\mathrm{av}}^2$. (The subscript '$s$' emphasizes surface polarization densities.) Note that due to nonlinearity, we cannot utilize phasor-domain formulation, and the previous two equations are in the time domain.

where c_0 denotes the speed of light in vacuum, η_0 denote the characteristic impedance of vacuum, the subscript 's' emphasizes surface polarization densities, and the averaged fields are defined as

$$\boldsymbol{\Psi}_{\text{av}} \triangleq \frac{\boldsymbol{\Psi}^{+} + \boldsymbol{\Psi}^{-}}{2}, \quad \text{where} \quad \boldsymbol{\Psi} = \{\boldsymbol{E}, \boldsymbol{H}\}. \tag{2.6}$$

The tensors, $\overline{\overline{\chi}}_{\text{ee}}$, $\overline{\overline{\chi}}_{\text{em}}$, $\overline{\overline{\chi}}_{\text{mm}}$ and $\overline{\overline{\chi}}_{\text{me}}$, represent the electric and magnetic (first subscript) surface susceptibilities that could be excited by electric or magnetic fields (second subscript). Note that $\overline{\overline{\chi}}_{\text{em}}$ and $\overline{\overline{\chi}}_{\text{me}}$ represent the bianisotropic nature of this metasurface.[4]

Substituting the polarization densities by surface susceptibilities in the GSTCs, i.e., substituting 2.5 in (2.4), the GSTCs will then become[5]

$$\hat{n} \times \Delta\boldsymbol{H} = j\omega\varepsilon_0 \overline{\overline{\chi}}_{\text{ee}} \cdot \boldsymbol{E}_{t,\text{av}} + jk_0 \overline{\overline{\chi}}_{\text{em}} \cdot \boldsymbol{H}_{t,\text{av}}, \tag{2.7a}$$

$$\Delta\boldsymbol{E} \times \hat{n} = j\omega\mu_0 \overline{\overline{\chi}}_{\text{mm}} \cdot \boldsymbol{H}_{t,\text{av}} + jk_0 \overline{\overline{\chi}}_{\text{me}} \cdot \boldsymbol{E}_{t,\text{av}}, \tag{2.7b}$$

where k_0 denote the free space wavenumber. Note that (2.7) assumes that the susceptibilities are only a function of spatial coordinates and they are invariant with respect to time. That is why we may refer to these metasurfaces as *space metasurfaces*. If the susceptibilities also change as a function of time, which is outside the scope of this thesis, we will then have *space-time metasurfaces* [42].

To understand this system of equations in a clear and simple manner, these equations can be expressed in their matrix form as

$$\begin{pmatrix} -\Delta H_v \\ \Delta H_u \end{pmatrix} = j\omega\varepsilon_0 \begin{pmatrix} \chi_{\text{ee}}^{uu} & \chi_{\text{ee}}^{uv} \\ \chi_{\text{ee}}^{vu} & \chi_{\text{ee}}^{vv} \end{pmatrix} \begin{pmatrix} E_{u,\text{av}} \\ E_{v,\text{av}} \end{pmatrix} + jk_0 \begin{pmatrix} \chi_{\text{em}}^{uu} & \chi_{\text{em}}^{uv} \\ \chi_{\text{em}}^{vu} & \chi_{\text{em}}^{vv} \end{pmatrix} \begin{pmatrix} H_{u,\text{av}} \\ H_{v,\text{av}} \end{pmatrix}, \tag{2.8a}$$

[4] If the metasurface is monoanisotropic as opposed to bianisotropic, then $\overline{\overline{\chi}}_{\text{em}} = \overline{\overline{\chi}}_{\text{me}} = \overline{\overline{0}}$ [22].

[5] As indicated earlier, if the metasurface is nonlinear, phase-domain formulation cannot be used, and the GSTCs need to be written in the time domain [41].

$$\begin{pmatrix} \Delta E_v \\ -\Delta E_u \end{pmatrix} = j\omega\mu_0 \begin{pmatrix} \chi_{\mathrm{mm}}^{uu} & \chi_{\mathrm{mm}}^{uv} \\ \chi_{\mathrm{mm}}^{vu} & \chi_{\mathrm{mm}}^{vv} \end{pmatrix} \begin{pmatrix} H_{u,\mathrm{av}} \\ H_{v,\mathrm{av}} \end{pmatrix} + jk_0 \begin{pmatrix} \chi_{\mathrm{me}}^{uu} & \chi_{\mathrm{me}}^{uv} \\ \chi_{\mathrm{me}}^{vu} & \chi_{\mathrm{me}}^{vv} \end{pmatrix} \begin{pmatrix} E_{u,\mathrm{av}} \\ E_{v,\mathrm{av}} \end{pmatrix}, \tag{2.8b}$$

where u and v represent vector components that are tangential to the surface that satisfy $\hat{u} \times \hat{v} = \hat{n}$ and $\hat{u} \perp \hat{v}$. For example, in our example, $\hat{u} = \hat{z}$ and $\hat{v} = \hat{x}$. The superscripts of χ indicate the direction of the applied field and that of the induced polarizability. For example, χ_{me}^{vu} indicates that for the applied electric (e) field in the $\hat{u}$ direction, there would be a resulting induced magnetic (m) current in the $\hat{v}$ direction.[6]

Note that if the tangential components of the EM fields on both sides of the metasurface are known, the susceptibility values χ of the metasurface can be solved. However, this results in infinite number of solutions. This is due to the fact that the above system of equations is under-determined with 16 unknown χ and 4 equations (all of which can be complex-valued). Sometimes it is worthwhile to split the unknowns and the equations into their real and imaginary parts so as to arrive at purely real system of equations; this will then result in 32 unknowns and 8 equations.

However, appropriate assumptions and conditions for metasurface design are typically employed which will significantly reduce the number of unknowns. These practical assumptions are reciprocity, losslessness and passivity.

[6]Note that in general the susceptibility tensors are 3×3 tensors. However, based on the electromagnetic equivalence principle, we have ignored the normal components of the susceptibilities and have simplified the susceptibility tensors to 2×2 tensors that only consider the tangential components [43]. However, there are cases where the incorporation of normal components are useful [39]. In addition, as noted earlier, if $\overline{\overline{\chi}}_{\mathrm{em}} = \overline{\overline{\chi}}_{\mathrm{me}} = \overline{\overline{0}}$, then the metasurface is monoanisotropic. Now if further assume that the off-diagonal elements of $\overline{\overline{\chi}}_{\mathrm{ee}}$ and $\overline{\overline{\chi}}_{\mathrm{mm}}$ are zero, we will then have a birefringent metasurface [22]. Then, for the birefringent metasurface, if we further assume that $\chi_{\mathrm{ee}}^{uu} = \chi_{\mathrm{ee}}^{vv}$ and $\chi_{\mathrm{mm}}^{uu} = \chi_{\mathrm{mm}}^{vv}$, then the birefringent metasurface becomes a monoisotropic metasurface. Therefore, from this point of view, one may consider the following flow for simplification of the metasurface model:

bianisotropic $\rightarrow$ monoanisotropic $\rightarrow$ birefringent $\rightarrow$ monoisotropic

2.3 Assumptions for Metasurface Design

Herein, we focus on some practical assumptions that can be made in the design of metasurfaces, and we will see their effect on the surface susceptibilites.

2.3.1 Non-gyrotropy

If the design process does not require change of polarization (such as linear polarization to circular polarization), then it is rational to assume that the metasurface is non-gyrotropic, which requires that [44]

$$\chi_{\mathrm{ee}}^{uv} = \chi_{\mathrm{ee}}^{vu} = \chi_{\mathrm{mm}}^{uv} = \chi_{\mathrm{mm}}^{vu} = \chi_{\mathrm{em}}^{uu} = \chi_{\mathrm{em}}^{vv} = \chi_{\mathrm{me}}^{uu} = \chi_{\mathrm{me}}^{vv} = 0 \tag{2.9}$$

This will reduce the number of unknowns from 16 complex χ to 8 complex χ. Subsequently, (2.8) will become

$$\begin{aligned} -\Delta H_v &= j\omega\epsilon_0\chi_{\mathrm{ee}}^{uu}E_{u,\mathrm{av}} + jk_0\chi_{\mathrm{em}}^{uv}H_{v,\mathrm{av}} \\ \Delta H_u &= j\omega\epsilon_0\chi_{\mathrm{ee}}^{vv}E_{v,\mathrm{av}} + jk_0\chi_{\mathrm{em}}^{vu}H_{u,\mathrm{av}} \\ \Delta E_v &= j\omega\mu_0\chi_{\mathrm{mm}}^{uu}H_{u,\mathrm{av}} + jk_0\chi_{\mathrm{me}}^{uv}E_{v,\mathrm{av}} \\ -\Delta E_u &= j\omega\mu_0\chi_{\mathrm{mm}}^{vv}H_{v,\mathrm{av}} + jk_0\chi_{\mathrm{me}}^{vu}E_{u,\mathrm{av}} \end{aligned} \tag{2.10}$$

2.3.2 Omega-type bianisotropy

The fact that we have assumed $\chi_{\mathrm{em}}^{uu} = \chi_{\mathrm{em}}^{vv} = \chi_{\mathrm{me}}^{uu} = \chi_{\mathrm{me}}^{vv} = 0$ in (2.9) links us to a particular form of bianisotropy. To understand this, let us note that a bianisotropic medium can be classified under two broad categories: reciprocal and non-reciprocal. In this thesis, the focus is on reciprocal metasurfaces. Under the reciprocal class, we have two general types of bianisotropic media: omega type and chiral type [36]. Herein, our focus is on omega bianisotropic metasurfaces. In omega bianisotropic metasurfaces, (i) the acting magnetic field will result in an electric current that is perpendicular to the acting magnetic field, and

(ii) the acting electric field will result in a magnetic current that is perpendicular to the acting electric field [13]. For this to happen, the diagonal components of $\overline{\overline{\chi}}_{\mathrm{me}}$ and $\overline{\overline{\chi}}_{\mathrm{em}}$ need to be zero. This is exactly the condition that we have for $\overline{\overline{\chi}}_{\mathrm{me}}$ and $\overline{\overline{\chi}}_{\mathrm{em}}$ in (2.9).

Omega-type bianisotropy is needed for wide angle refraction (wide angle beam steering) [13], and that is why it is employed in this thesis. On the other hand, for chiral metasurfaces, the induced electric current due to the acting magnetic field are parallel and also the induced magnetic current due to the acting electric field are parallel; this requires the diagonal components of $\overline{\overline{\chi}}_{\mathrm{me}}$ and $\overline{\overline{\chi}}_{\mathrm{em}}$. The chiral metasurfaces can be used for polarization rotation, which is outside the scope of this thesis.

2.3.3 Reciprocity

Although we briefly noted the reciprocity in the previous section, let us now have a closer look at its requirements. It is typically desired to design a reciprocal metasurface to avoid complications such as applying external magnetic bias to ferrite or the use of the so-called space-time metasurfaces as described in [44,45]. (It should be noted that for several applications, non-reciprocal systems are in fact needed; however, in this thesis, we limit ourselves to reciprocal systems.) A reciprocal metasurface indicates that the field at the observer location will not change if the location of the source and the observer interchanged, which requires its susceptibility tensors to satisfy [22, 46]

$$\overline{\overline{\chi}}_{\mathrm{ee}}^{\mathrm{T}} = \overline{\overline{\chi}}_{\mathrm{ee}}, \quad \overline{\overline{\chi}}_{\mathrm{mm}}^{\mathrm{T}} = \overline{\overline{\chi}}_{\mathrm{mm}}, \quad \overline{\overline{\chi}}_{\mathrm{em}}^{\mathrm{T}} = -\overline{\overline{\chi}}_{\mathrm{me}}, \tag{2.11}$$

where the superscript 'T' denotes the transpose operator. Assuming non-gyrotropy and reciprocity, we have now reduced the number of unknowns to 6 complex χ.

2.3.4 Passivity and losslessness

In many applications, passive and lossless metasurfaces are preferred to avoid lossy elements (to avoid power loss) and/or active element devices (to avoid biasing) [44]. The loss and gain in the metasurface can be analyzed through the time-average Poynting vector stated as [46]

$$\langle \boldsymbol{S} \rangle = \frac{1}{2}\mathrm{Re}(\boldsymbol{E} \times \boldsymbol{H}^*), \tag{2.12}$$

where the $\langle \cdot \rangle$ operator denotes the time-average operator, $\boldsymbol{S}$ denotes the Poynting vector, 'Re' denotes the real-part operator, and the superscript $*$ represents the complex conjugate operator. Since $\langle \boldsymbol{S} \rangle$ represents the time-average energy flow, its divergence, $\nabla \cdot \langle \boldsymbol{S} \rangle$, can be used to determine whether the metasurface is acting like a source or a drain of energy. This can be explicitly stated in terms of the surface susceptibility tensors as [22]

$$\begin{aligned} \nabla \cdot \langle \boldsymbol{S} \rangle = -\frac{1}{4}\mathrm{Re}\Big[j\omega \Big(\varepsilon_0 \boldsymbol{E}^* \cdot (2\overline{\overline{\chi}}_{\mathrm{ee}} - \overline{\overline{\chi}}_{\mathrm{ee}}^* - \overline{\overline{\chi}}_{\mathrm{ee}}^\dagger) \cdot \boldsymbol{E} + \mu_0 \boldsymbol{H}^* \cdot (2\overline{\overline{\chi}}_{\mathrm{mm}} - \overline{\overline{\chi}}_{\mathrm{mm}}^* - \overline{\overline{\chi}}_{\mathrm{mm}}^\dagger) \cdot \boldsymbol{H} \\ + \; 2k_0 \boldsymbol{E}^* \cdot (\overline{\overline{\chi}}_{\mathrm{me}} - \overline{\overline{\chi}}_{\mathrm{em}}^\dagger) \cdot \boldsymbol{H} \Big) \Big], \end{aligned} \tag{2.13}$$

where the superscript $\dagger$ denotes the Hermitian (complex conjugate transpose) operator. The terms $\boldsymbol{E}$ and $\boldsymbol{H}$ represent the acting fields that can be expressed in terms of the average fields, and for the metasurface to be passive and lossless, $\nabla \cdot \langle \boldsymbol{S} \rangle$ must be zero for arbitrary sets of $\boldsymbol{E}$ and $\boldsymbol{H}$. This can be met by

$$\begin{aligned} 2\overline{\overline{\chi}}_{\mathrm{ee}} - \overline{\overline{\chi}}_{\mathrm{ee}}^* - \overline{\overline{\chi}}_{\mathrm{ee}}^\dagger = 0 \\ 2\overline{\overline{\chi}}_{\mathrm{mm}} - \overline{\overline{\chi}}_{\mathrm{mm}}^* - \overline{\overline{\chi}}_{\mathrm{mm}}^\dagger = 0 \\ \overline{\overline{\chi}}_{\mathrm{em}}^\dagger - \overline{\overline{\chi}}_{\mathrm{me}} = 0 \end{aligned} \tag{2.14}$$

If we also assume a reciprocal metasurface, which requires satisfying (2.11), the conditions

for losslessness and passivity as noted in (2.14) can be simplified as

$$\begin{aligned} \mathrm{Im}(\overline{\overline{\chi}}_{\mathrm{ee}}) &= 0 \\ \mathrm{Im}(\overline{\overline{\chi}}_{\mathrm{mm}}) &= 0 \\ \mathrm{Re}(\overline{\overline{\chi}}_{\mathrm{em}}) &= 0 \\ \mathrm{Re}(\overline{\overline{\chi}}_{\mathrm{me}}) &= 0. \end{aligned} \tag{2.15}$$

where 'Im' denotes the imaginary-part operator.

We have already noted that if we consider non-gyrotropy and reciprocity, we will have 6 unknown complex χ, which is equivalent to 12 real-valued unknown components. Considering the lossless and passivity constraints as listed in (2.15), we will now have 6 real unknowns.

2.3.5 Fixing the polarization

In this work, we consider a fixed polarization. That is, we assume that the *tangential* electric field on the metasurface has only one component (say, E_u) and also the *tangential* magnetic field on the metasurface has one component (say, H_v). Then, after applying the reciprocity condition, (2.10) will become

$$\begin{aligned} -\Delta H_v &= j\omega\epsilon_0\chi_{\mathrm{ee}}^{uu}E_{u,\mathrm{av}} + jk_0\chi_{\mathrm{em}}^{uv}H_{v,\mathrm{av}} \\ -\Delta E_u &= j\omega\mu_0\chi_{\mathrm{mm}}^{vv}H_{v,\mathrm{av}} - jk_0\chi_{\mathrm{em}}^{uv}E_{u,\mathrm{av}} \end{aligned} \tag{2.16}$$

This represents two complex equations or equivalently four real-valued equations. Based on the losslessness and passivity condition, we also have three real unknowns. This may be seen as an over-determined system of equations.

To better understand this, we should note that for the metasurface to be lossless and passive, it needs to satisfy the local power conservation (LPC) constraint [29, 30]. That is, at any unit cell of the metasurface, the real part of the in-going power density needs to be equal to

the real part of the out-going power density. Now, let us assume that the LPC is satisfied for the desired field transformation. In other words, we would like to solve (2.16) while knowing that the LPC has already been met by $\{E_u^+, E_u^-, H_v^+, H_v^-\}$. (We later discuss the LPC constraint in more details in Section 4.4.5.)

For the sake of discussion, let us now assume that in (2.16) χ_{em}^{uv} is a complex susceptibility (i.e., having real and imaginary parts). We still require χ_{ee}^{uu} and χ_{mm}^{vv} to be purely real. Therefore, we now have four real unknowns. (The real and imaginary parts of χ_{em}^{uv} are treated as two real unknowns.) Thus, solving (2.16) is now equivalent to solving for four real equations with four real unknowns. Since the LPC is satisfied, when the two components (real and imaginary parts) of χ_{em}^{uv} are solved, we will observe that its real part is zero since the metasurface has to be lossless and passive. This is due to the fact that the LPC is already satisfied and $\chi_{\text{ee}}^{uu}, \chi_{\text{mm}}^{vv}$ are purely real. If χ_{em}^{uv} is to have a real component, we should then have either gain or loss, which is in contradiction with the LPC constraint. That is why (2.16) can be solved with a unique solution if the tangential fields satisfy the LPC constraint.

2.4 Two-Port Network Model for Metasurfaces

As discussed above, a metasurface transforms a set of tangential fields to another one. This 'wave transformation' can be modeled by a two-port networks using parameters like the scattering parameters (S-parameters) [47], impedance parameters (Z-parameters) [13], transmission parameters (ABCD parameters) [48]. This concept has been depicted in Figure 2.2. Herein, the transmission parameters are adopted because of its advantage in analyzing cascaded networks.

To explain this, let us consider electromagnetic waves with the tangential components on the metasurface as (E_u, H_v). The unit cell of the metasurface lies on the uv plane as shown in Figure 2.2 and is considered to be non-gyrotropic and reciprocal. The GSTCs can then

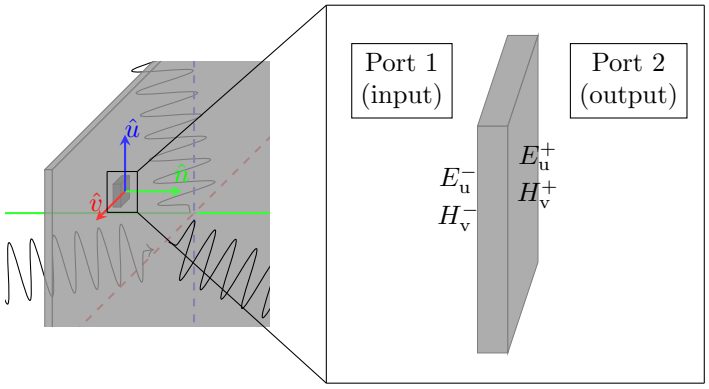

Fig. 2.2: A close-up look at the unit cell of the metasurface. For analysis, the tangential fields are assumed to be uniform over the unit cell. The systematic transformation from one set of tangential fields to another can be treated as a two-port network.

be written as

$$H_v^- - H_v^+ = \frac{j\omega\varepsilon_0}{2}\chi_{\mathrm{ee}}^{uu}\left(E_u^+ + E_u^-\right) + \frac{jk_0}{2}\chi_{\mathrm{em}}^{uv}\left(H_v^+ + H_v^-\right), \tag{2.17a}$$

$$E_u^- - E_u^+ = \frac{j\omega\mu_0}{2}\chi_{\mathrm{mm}}^{vv}\left(H_v^+ + H_v^-\right) - \frac{jk_0}{2}\chi_{\mathrm{em}}^{uv}\left(E_u^+ + E_u^-\right). \tag{2.17b}$$

The above equations can then be written into the matrix representation of a transmission two-port network as [49]

$$\begin{pmatrix} E_u^- \\ H_v^- \end{pmatrix} = \begin{pmatrix} T_{11} & T_{12} \\ T_{21} & T_{22} \end{pmatrix} \begin{pmatrix} E_u^+ \\ H_v^+ \end{pmatrix}, \tag{2.18}$$

where

$$T_{11} = \frac{\zeta\tau\chi_{\mathrm{ee}}^{uu}\chi_{\mathrm{mm}}^{vv} + \left(1 - \xi\chi_{\mathrm{em}}^{uv}\right)^2}{1 - \zeta\tau\chi_{\mathrm{ee}}^{uu}\chi_{\mathrm{mm}}^{vv} - \left(\xi\chi_{\mathrm{em}}^{uv}\right)^2}, \tag{2.19a}$$

$$T_{12} = \frac{2\tau\chi_{\mathrm{mm}}^{vv}}{1 - \zeta\tau\chi_{\mathrm{ee}}^{uu}\chi_{\mathrm{mm}}^{vv} - \left(\xi\chi_{\mathrm{em}}^{uv}\right)^2}, \tag{2.19b}$$

$$T_{21} = \frac{2\zeta\chi_{\mathrm{ee}}^{uu}}{1 - \zeta\tau\chi_{\mathrm{ee}}^{uu}\chi_{\mathrm{mm}}^{vv} - \left(\xi\chi_{\mathrm{em}}^{uv}\right)^2}, \tag{2.19c}$$

$$T_{22} = \frac{\zeta\tau\chi_{\mathrm{ee}}^{uu}\chi_{\mathrm{mm}}^{vv} + \left(1 + \xi\chi_{\mathrm{em}}^{uv}\right)^2}{1 - \zeta\tau\chi_{\mathrm{ee}}^{uu}\chi_{\mathrm{mm}}^{vv} - \left(\xi\chi_{\mathrm{em}}^{uv}\right)^2}, \tag{2.19d}$$

and

$$\zeta = \frac{j\omega\varepsilon_0}{2},\ \xi = \frac{jk_0}{2},\ \tau = \frac{j\omega\mu_0}{2}. \tag{2.20}$$

Based on the above, two observations can be made:

- Notice that the determinant of the transmission matrix is unity, i.e. $T_{11}T_{22} - T_{12}T_{21} = 1$, which corroborates the reciprocity assumption.

- Another observation to be made is that if the metasurface is passive and lossless (χ_{ee}^{uu} and χ_{mm}^{vv} are purely real, and χ_{em}^{uv} is purely imaginary), then T_{11} and T_{22} will be purely real, and T_{12} and T_{21} will be purely imaginary, which corroborates the passive and lossless condition for two-port network represented by transmission parameters.

Similarly, for the other polarization, i.e., with tangential components as (E_v, H_u), the GSTCs read

$$H_u^+ - H_u^- = \frac{j\omega\varepsilon_0}{2}\chi_{\mathrm{ee}}^{vv}\left(E_v^+ + E_v^-\right) + \frac{jk_0}{2}\chi_{\mathrm{em}}^{vu}\left(H_u^+ + H_u^-\right), \tag{2.21a}$$

$$E_v^+ - E_v^- = \frac{j\omega\mu_0}{2}\chi_{\mathrm{mm}}^{uu}\left(H_u^+ + H_u^-\right) - \frac{jk_0}{2}\chi_{\mathrm{em}}^{vu}\left(E_v^+ + E_v^-\right), \tag{2.21b}$$

and the corresponding transmission parameters are [23]

$$T_{11} = \frac{\zeta\tau\chi_{\mathrm{ee}}^{uu}\chi_{\mathrm{mm}}^{vv} + \left(1 + \xi\chi_{\mathrm{em}}^{uv}\right)^2}{1 - \zeta\tau\chi_{\mathrm{ee}}^{uu}\chi_{\mathrm{mm}}^{vv} - \left(\xi\chi_{\mathrm{em}}^{uv}\right)^2}, \tag{2.22a}$$

$$T_{12} = \frac{2\tau\chi_{\mathrm{mm}}^{vv}}{\zeta\tau\chi_{\mathrm{ee}}^{uu}\chi_{\mathrm{mm}}^{vv} + \left(\xi\chi_{\mathrm{em}}^{uv}\right)^2 - 1}, \tag{2.22b}$$

$$T_{21} = \frac{2\zeta\chi_{\mathrm{ee}}^{uu}}{\zeta\tau\chi_{\mathrm{ee}}^{uu}\chi_{\mathrm{mm}}^{vv} + \left(\xi\chi_{\mathrm{em}}^{uv}\right)^2 - 1}, \tag{2.22c}$$

$$T_{22} = \frac{\zeta\tau\chi_{\mathrm{ee}}^{uu}\chi_{\mathrm{mm}}^{vv} + \left(1 - \xi\chi_{\mathrm{em}}^{uv}\right)^2}{1 - \zeta\tau\chi_{\mathrm{ee}}^{uu}\chi_{\mathrm{mm}}^{vv} - \left(\xi\chi_{\mathrm{em}}^{uv}\right)^2}. \tag{2.22d}$$

2.4.1 Unit cell topology

To verify the metasurface design, ideal or realistic physical models can be made from the two-port network parameters that are derived from the material parameters. Consider the case where the transmission parameters are known and the metasurface is reciprocal, the three *independent*[7] parameters can be realized using an ideal topology that consists of three admittance sheets connected by two dielectric substrates as in [48]. This is shown in Figure 2.3 where we can see three impedance layers (denoted by their admittances Y_1, Y_2, and Y_3) connected with two dielectric substrates with the thickness of $t_{\mathrm{TL},1}$ and $t_{\mathrm{TL},2}$.

The resulting transmission parameters of the cascaded structure are calculated as [48]

$$\overline{\overline{T}} = \overline{\overline{T}}_{Y,1} \cdot \overline{\overline{T}}_{\mathrm{TL},1} \cdot \overline{\overline{T}}_{Y,2} \cdot \overline{\overline{T}}_{\mathrm{TL},2} \cdot \overline{\overline{T}}_{Y,3}, \tag{2.23}$$

where the transmission parameters of the admittance sheets are expressed as

$$\overline{\overline{T}}_{Y,i} = \begin{pmatrix} 1 & 0 \\ Y_i & 1 \end{pmatrix}, \; i = 1, 2, 3, \tag{2.24}$$

and the transmission parameters of the dielectric substrates are expressed as

$$\overline{\overline{T}}_{\mathrm{TL},i} = \begin{pmatrix} T_{\mathrm{TL},i,11} & T_{\mathrm{TL},i,12} \\ T_{\mathrm{TL},i,21} & T_{\mathrm{TL},i,22} \end{pmatrix} = \begin{pmatrix} \cos(\beta_{\mathrm{TL},i} t_{\mathrm{TL},i}) & jZ_{\mathrm{TL},i} \sin(\beta_{\mathrm{TL},i} t_{\mathrm{TL},i}) \\ \frac{j \sin(\beta_{\mathrm{TL},i} t_{\mathrm{TL},i})}{Z_{\mathrm{TL},i}} & \cos(\beta_{\mathrm{TL},i} t_{\mathrm{TL},i}) \end{pmatrix}, \; i = 1, 2, \tag{2.25}$$

with Y_i denoting the admittance value, $\beta_{\mathrm{TL},i}$ denoting the phase constant in the dielectric, $t_{\mathrm{TL},i}$ denoting the thickness of the dielectric, and $Z_{\mathrm{TL},i}$ denoting the characteristic impedance of the dielectric. Once the substrates are determined, the admittance values can

[7] One of the parameters is dropped due to the reciprocity assumption.

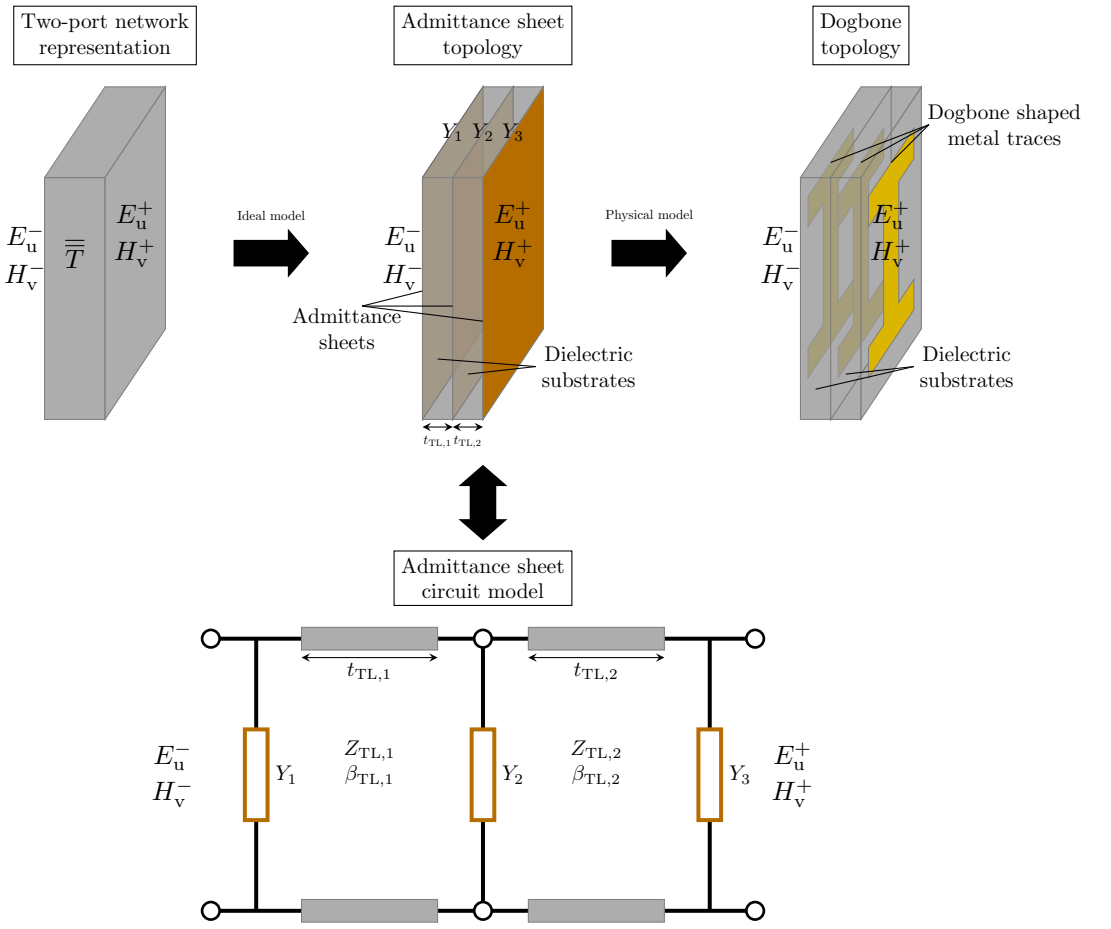

Fig. 2.3: Demonstration of the three-layer admittance sheet topology. This ideal model can be physically realized using the dogbone structure.

be calculated as [48, 49]

$$Y_1 = \frac{T_{22} - Y_2 T_{\mathrm{TL},1,22} T_{\mathrm{TL},2,12} - T_{\mathrm{TL},1,21} T_{\mathrm{TL},2,12} - T_{\mathrm{TL},1,22} T_{\mathrm{TL},2,22}}{Y_2 T_{\mathrm{TL},1,12} T_{\mathrm{TL},2,12} + T_{\mathrm{TL},1,11} T_{\mathrm{TL},2,12} + T_{\mathrm{TL},1,12} T_{\mathrm{TL},2,22}}, \tag{2.26a}$$

$$Y_2 = \frac{T_{12} - T_{\mathrm{TL},1,11} T_{\mathrm{TL},2,12} - T_{\mathrm{TL},1,12} T_{\mathrm{TL},2,22}}{T_{\mathrm{TL},1,12} T_{\mathrm{TL},2,12}}, \tag{2.26b}$$

$$Y_3 = \frac{T_{11} - Y_2 T_{\mathrm{TL},1,12} T_{\mathrm{TL},2,11} - T_{\mathrm{TL},1,11} T_{\mathrm{TL},2,11} - T_{\mathrm{TL},1,12} T_{\mathrm{TL},2,21}}{Y_2 T_{\mathrm{TL},1,12} T_{\mathrm{TL},2,12} + T_{\mathrm{TL},1,11} T_{\mathrm{TL},2,12} + T_{\mathrm{TL},1,12} T_{\mathrm{TL},2,22}}. \tag{2.26c}$$

It is worth noting that for passive and lossless metasurfaces, Y_1, Y_2, and Y_3 are purely imaginary, which correspond to capacitive or inductive sheets. This unit cell topology is

can then be simulated in Ansys HFSS using impedance sheets. In practice, these impedance sheets need to be converted to physical structures such as the dogbone structure. To do this, typically dogbones of various shapes are simulated and then a lookup table is formed, and is then used to choose a dogbone structure that corresponds to the desired capacitive or inductive value [50,51]. Alternatively, the physical design may be pursued using machine learning approaches [52]. The physical procedure is not presented herein and it is outside the scope of this thesis.

2.4.2 Asymmetry and bianisotropy

To understand how bianisotropy can be achieved using a three layer design, let us write the impedance matrix representation of the two-port network as

$$\begin{pmatrix} E_u^- \\ E_u^+ \end{pmatrix} = \begin{pmatrix} Z_{11} & Z_{12} \\ Z_{21} & Z_{22} \end{pmatrix} \begin{pmatrix} H_v^- \\ -H_v^+ \end{pmatrix}, \tag{2.27}$$

for (E_u, H_v) polarization (tangential components on the metasurface). Noting (2.17), we can then derive the two-port impedance paramaters as

$$Z_{11} = \frac{\zeta\tau\chi_{\mathrm{ee}}^{uu}\chi_{\mathrm{mm}}^{vv} + (1-\xi\chi_{\mathrm{em}}^{uv})^2}{2\zeta\chi_{\mathrm{ee}}^{uu}}, \tag{2.28a}$$

$$Z_{12} = \frac{-\zeta\tau\chi_{\mathrm{ee}}^{uu}\chi_{\mathrm{mm}}^{vv} + 1 - (\xi\chi_{\mathrm{em}}^{uv})^2}{2\zeta\chi_{\mathrm{ee}}^{uu}}, \tag{2.28b}$$

$$Z_{21} = \frac{-\zeta\tau\chi_{\mathrm{ee}}^{uu}\chi_{\mathrm{mm}}^{vv} + 1 - (\xi\chi_{\mathrm{em}}^{uv})^2}{2\zeta\chi_{\mathrm{ee}}^{uu}}, \tag{2.28c}$$

$$Z_{22} = \frac{\zeta\tau\chi_{\mathrm{ee}}^{uu}\chi_{\mathrm{mm}}^{vv} + (1+\xi\chi_{\mathrm{em}}^{uv})^2}{2\zeta\chi_{\mathrm{ee}}^{uu}}, \tag{2.28d}$$

where $\zeta = \frac{j\omega\varepsilon_0}{2}$, $\xi = \frac{jk_0}{2}$, and $\tau = \frac{j\omega\mu_0}{2}$.

As expected, due to reciprocity, we have $Z_{12} = Z_{21}$. More importantly, it can be seen that if $\chi_{\mathrm{em}}^{uv} \neq 0$, then $Z_{11} \neq Z_{12}$. That is, for bianisotropic design, we need to create asymmetric

two-port networks. Based on our model, this requires $Y_1 \neq Y_3$. Further details on this topic based on the surface impedance model of metasurfaces can be found in [53].

Chapter 3

Electromagnetic Inversion

As described in the previous chapter, we need to know what the tangential fields on the metasurface are so as to obtain the required surface susceptibilities. However, in many applications, we do not know the tangential fields on the metasurface. For example, let us consider a design scenario in which the designer would like to achieve two main beams in the far-field zone in specified directions with a few specified null angles. Based on these performance criteria, how can we find the tangential fields to support the desired specifications? This is why we need a mechanism to use these design objectives to obtain the required tangential fields. As will be seen, similar to [28, 32], our approach to address this is based on formulating an electromagnetic inverse problem.

In general, an electromagnetic inverse problem describes a situation where the electromagnetic *effects* or observations are known and the *causes* of these observations are to be found. The three essential components in such problems are the sources (e.g., a radiating antenna), materials (e.g., dielectric substrates, human body, or simply free space), and the resulting fields (e.g., the fields in the far-field zone). A forward problem can be constructed if the source and the material are given. On the other hand, inverse problems typically deal with finding source or material properties. Therefore, EM inversion can be characterized into

two broad categories depending on the unknown [54]:

- One is the *inverse scattering* problem where the resulting fields and the source are known, and the goal is to find what material properties (e.g., relative complex permittivity) have created the effects.

- The other one is the *inverse source* problem where the goal is to find the source where the resulting fields and material properties are known.

A typical example that is related to the inverse scattering problem is microwave imaging where the dielectric properties of the object being imaged is to be found from the knowledge of resulting scattered fields and the illuminating antennas [55]. Similarly, the inverse scattering framework can be used to design dielectric lenses, by finding their required dielectric profiles, to satisfy far-field performance criteria [56]. On the other hand, A typical example for inverse source problems is antenna diagnostics where the goal to to find the equivalent currents of the antenna under test and then find the faulty element in the antenna array [57, 58].

More recently, metasurface design has been cast as an electromagnetic inverse problem [28, 30, 59] where the followings are assumed to be known:

- The source that illuminates the metasurface. For example, as will be seen in this thesis, the source can be a plane wave, a line source or a horn antenna.

- The desired far-field power pattern or the desired far-field performance criteria such as main beam directions, half-power beamwidth (HPBW), and null angles.

The unknown is then

- the required macroscopic properties of the metasurface such as surface susceptibilites $(\chi_{\mathrm{ee}}^{uu}, \chi_{\mathrm{mm}}^{vv}, \chi_{\mathrm{em}}^{uv})$ that we have discussed in the previous chapter.

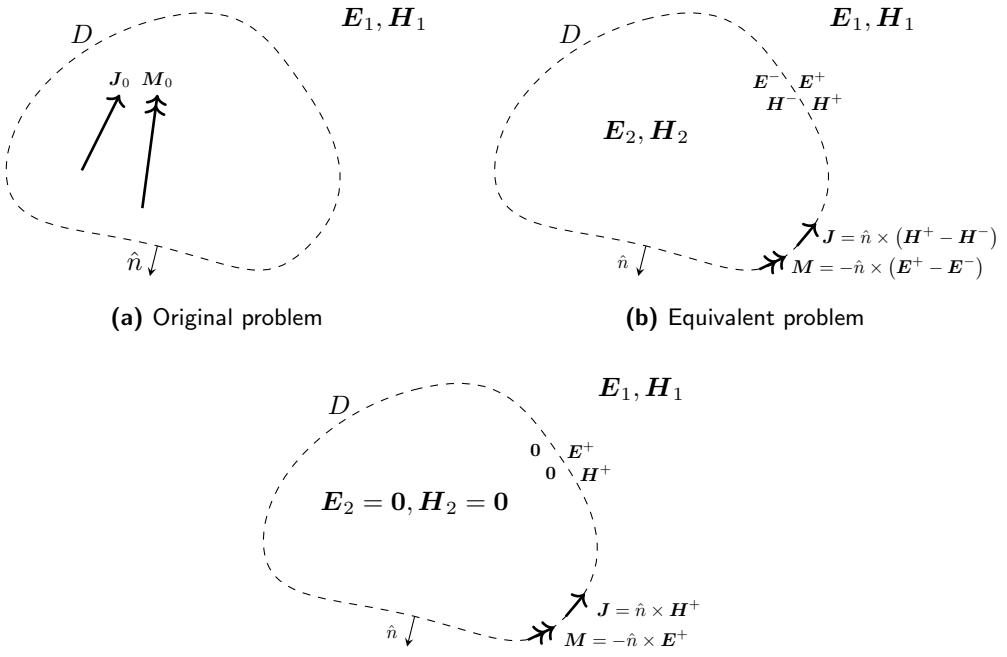

(a) Original problem

(b) Equivalent problem

(c) Equivalent problem under Love's equivalence principle

Fig. 3.1: Demonstration of the equivalent principle. The original current sources in (a), $\boldsymbol{J}_0$ and $\boldsymbol{M}_0$, produces $\boldsymbol{E}_1$ and $\boldsymbol{H}_1$ everywhere. A set of equivalent surface current densities in (b), $\boldsymbol{J}$ and $\boldsymbol{M}$, produces the same fields outside D and different fields inside D. (c) The Love's equivalent principle assumes null internal fields.

Based on the above definition of inverse scattering problems, the inverse metasurface design problem can be classified under inverse scattering problems, but as will be seen, it can also be treated as an inverse source problem. This section will focus on describing the proposed inverse source problem, and its associated details.

3.1 Problem Statement

Consider a set of impressed electric and magnetic current density sources, $\boldsymbol{J}_0$ and $\boldsymbol{M}_0$, enclosed by an imaginary closed surface D as shown in Figure 3.1. According to the equivalence principle [60], we can remove the original sources, then assume arbitrary fields within in the internal region of fictitious surface D, and then support the discontinuity between

the assumed internal fields and the original external fields with surface electric and magnetic currents on D, denoted by $\boldsymbol{J}$ and $\boldsymbol{M}$. Based on the EM's boundary conditions, these surface currents will be

$$\boldsymbol{J} = \hat{n} \times \left(\boldsymbol{H}^{+} - \boldsymbol{H}^{-}\right), \tag{3.1a}$$

$$\boldsymbol{M} = -\hat{n} \times \left(\boldsymbol{E}^{+} - \boldsymbol{E}^{-}\right), \tag{3.1b}$$

where $\hat{n}$ denotes the unit vector that is normal to the surface D, '$\times$' denotes vector cross-product, and the superscripts '$+$' and '$-$' indicate the locations of the surface boundary that is in the direction of $\hat{n}$, and opposite to $\hat{n}$, respectively. Notice that in the equivalent problem, the sources, the material and the fields inside D are not necessarily the same as the original ones. For the inverse source problem, it is assumed that the material outside D, and the fields away from and outside D are known, and the goal is to find the equivalent surface currents $\boldsymbol{J}$ and $\boldsymbol{M}$.

As will be seen, in this thesis, we invoke a particular form of the equivalence principle known as Love's equivalence principle [61] in which the internal fields are assumed to be zero, and the equivalent problem is formed with respect to the external region. Thus, the surface electric and magnetic currents will be

$$\boldsymbol{J} = \hat{n} \times \boldsymbol{H}^{+}, \tag{3.2a}$$

$$\boldsymbol{M} = -\hat{n} \times \boldsymbol{E}^{+}. \tag{3.2b}$$

Note that the '$\hat{n}\times$' operator yields the tangential component of the field on which it operates; thus, these Love's equivalent currents are directly related to the tangential fields. This makes them, in particular, suitable for metasurface design applications in which the tangential fields are a critical part of the GSTCs. Therefore, the problem may be stated as follows.

– For a given desired power pattern, find a set of Love's currents that support the given pattern.

As will be seen later, the above objective is not sufficient for the design of lossless and passive metasurfaces as the currents need to meet an extra condition known as the LPC constraint [30]. In addition, it is typically desirable to deal with smoother currents for practical implementation [31].

3.2 Forward Problem

Since the inverse source problem is the 'inverse' of the forward problem, it is necessary to first construct the forward problem that establishes the relationship between the equivalent currents, the material, and the resulting fields. Similar to [32], assuming vacuum for simplicity, their relationship is described by the electric and magnetic field integral equations (often abbreviated as EFIE and MFIE). These can be written as [62][1]

$$\boldsymbol{E}(\boldsymbol{r}) = -j\eta_0 k_0 \int_D \widetilde{G}_0(\boldsymbol{r},\boldsymbol{r}') \cdot \boldsymbol{J}(\boldsymbol{r}')\mathrm{d}S' + \int_D \boldsymbol{M}(\boldsymbol{r}') \times \nabla g_0(\boldsymbol{r},\boldsymbol{r}')\mathrm{d}S', \tag{3.3a}$$

$$\boldsymbol{H}(\boldsymbol{r}) = -\frac{jk_0}{\eta_0} \int_D \widetilde{G}_0(\boldsymbol{r},\boldsymbol{r}') \cdot \boldsymbol{M}(\boldsymbol{r}')\mathrm{d}S' - \int_D \boldsymbol{J}(\boldsymbol{r}') \times \nabla g_0(\boldsymbol{r},\boldsymbol{r}')\mathrm{d}S', \tag{3.3b}$$

where $\boldsymbol{r}$ and $\boldsymbol{r}'$ are the position vectors and '∇' denotes the gradient operator. In addition, $\widetilde{G}_0$ is the free space dyadic Green's function that can be written as

$$\widetilde{G}_0 = \left(\widetilde{I} + \frac{1}{k_0^2}\nabla\nabla\right) g_0(\boldsymbol{r},\boldsymbol{r}'), \tag{3.4}$$

where $\widetilde{I}$ is the unit dyadic, and g_0 denotes the 3D free space Green's function that can be expressed as

$$g_0(\boldsymbol{r},\boldsymbol{r}') = \frac{e^{-jk_0|\boldsymbol{r}-\boldsymbol{r}'|}}{4\pi|\boldsymbol{r}-\boldsymbol{r}'|}. \tag{3.5}$$

[1] Throughout this thesis, we assume a time-dependency of $\exp(j\omega t)$.

where k_0 is the wavenumber in free space.

According to the uniqueness theorem [63], there is a unique solution to the Maxwell's equations if the source inside the boundary, and the tangential electric *or* magnetic fields on the boundary are known [2], which means solving one of the equations in (3.3) is sufficient for the forward problem.[3] If the electric field is of interest for example, the forward operator $\mathcal{A}$ can be used to represent the forward mapping from the current densities to the electric field as

$$\boldsymbol{E} = \mathcal{A}\left(\boldsymbol{J}, \boldsymbol{M}\right). \tag{3.6}$$

where $\mathcal{A}$ is defined based on (3.3a). Also note that assuming $\boldsymbol{J} = \boldsymbol{J}_1 + \alpha\boldsymbol{J}_2$ and $\boldsymbol{M} = \boldsymbol{M}_1 + \alpha\boldsymbol{M}_2$, where α is a scalar, the operator $\mathcal{A}$ satisfies

$$\mathcal{A}\left(\boldsymbol{J}, \boldsymbol{M}\right) = \mathcal{A}\left(\boldsymbol{J}_1, \boldsymbol{M}_1\right) + \alpha\mathcal{A}\left(\boldsymbol{J}_2, \boldsymbol{M}_2\right), \tag{3.7}$$

which means $\mathcal{A}$ is a linear operator. It should be emphasized that this operator is linear for the complex output, i.e, complex (magnitude and phase) field $\boldsymbol{E}$. On the other hand, in our inverse problem we deal with power pattern synthesis. Thus, we are effectively dealing with $|\boldsymbol{E}|^2$ (magnitude-only) which makes the inverse problem nonlinear.

3.3 Inverse Source Problem

As noted above for the forward problem, the known quantities are current densities and the unknown is their resulting effect, e.g., $\boldsymbol{E}$. The situation is reverse in the inverse problem, and more precisely in the inverse source problem. In inverse source problems, the unknowns are the current densities, and the known quantities are the left hand side of (3.3) at a given

[2] This theorem is derived for lossy media, and the lossless case is justified by letting loss go to zero.

[3] In certain cases, which are outside the scope of this thesis, one might solve a combined EFIE and MFIE problem in the form of α EFIE $+ (1-\alpha)\frac{j}{k}$ MFIE [64, Sec. 3.2.1] where $0 \leq \alpha \leq 1$. This approach is called the combined field integral equation (CFIE). Note that if $\alpha = 1$, then the CFIE becomes the EFIE.

region of interest, e.g., in the far-field zone. In other words, the known quantities are the EM effect of these unknown sources.

Considering the current densities as the unknowns, the equations in (3.3) will be Fredholm integral equations of the first kind, which suggests that the problem is ill-posed [65]. This ill-posed problem need to be solved numerically, and may have zero or infinite number of solutions. For example, there may exist no sets of current densities that can produce the given EM fields, as the fields might represents a far-field directivity level that is not achievable with the given aperture for the current densities. This is known as the non-existence of the solution.

Moreover, the data (EM effect) are typically known at discrete number of angles (e.g., over a specified angular interval in the far-field zone). Then, there may exist non-radiating (NR) sources, $\boldsymbol{J}_{\mathrm{NR}}$ and $\boldsymbol{M}_{\mathrm{NR}}$, such that $\mathcal{A}\left(\boldsymbol{J}_{NR}, \boldsymbol{M}_{NR}\right)$ is zero at the data locations [57]. Note that the effect of these NR currents can still be non-zero at some other locations which are not specified by the designer, and is therefore absent in the problem formulation. This is because that the Green's function acts like a low-pass spatial filter that attenuates high *spatial* frequency components of the sources (e.g., evanescent waves). Since $\mathcal{A}$ is linear, adding the NR sources to the solution will not change the field data (based on a finite precision numerical calculation). This can create infinite number of solutions. In the design process, this non-uniqueness is an advantage and ideally the designer needs to choose the best solution, e.g., in terms of the ease of fabrication.

To solve this ill-posed problem, a cost functional is formed and minimized using an optimization algorithm, which is the conjugate gradient (CG) method in our case. Assuming that the electric field data desired by the designer at a given region of interest (ROI) is denoted by $\boldsymbol{E}_{\mathrm{des}}$, the cost functional reads as

$$\mathcal{C}\left(\boldsymbol{J}, \boldsymbol{M}\right) = \left\| \mathcal{A}\left(\boldsymbol{J}, \boldsymbol{M}\right) - \boldsymbol{E}_{\mathrm{des}} \right\|_{\mathrm{ROI}}^{2}, \tag{3.8}$$

where $\|\cdot\|_{\text{ROI}}$ denotes the L_2 norm over the ROI, and it is defined as

$$\|\boldsymbol{E}\|_{\text{ROI}} = \langle \boldsymbol{E}, \boldsymbol{E} \rangle_{\text{ROI}}^{\frac{1}{2}}, \tag{3.9}$$

with the inner product, $\langle \cdot, \cdot \rangle$, defined as

$$\langle \boldsymbol{E}_1, \boldsymbol{E}_2 \rangle_{\text{ROI}} = \int_{\text{ROI}} \boldsymbol{E}_1(\boldsymbol{r}') \cdot \boldsymbol{E}_2^*(\boldsymbol{r}') d\boldsymbol{r}'. \tag{3.10}$$

where '$\cdot$' in the above equation represent the vector dot product. The above cost functional, often referred to as the data misfit cost functional, is then minimized over $\boldsymbol{J}$ and $\boldsymbol{M}$ using the CG method. The CG method works in an iterative manner and yields the required $\boldsymbol{J}$ and $\boldsymbol{M}$ when converges.

Numerically solving this minimization problem requires discretization of $\boldsymbol{J}$ and $\boldsymbol{M}$ over D and the field data $\boldsymbol{E}_{\text{des}}$ over the ROI. As will be seen later, there are often other requirements to be enforced on the sources so as to meet design constraints. Therefore, other regularization terms will be introduced in Chapters 4 to accommodate the extra needs. This will potentially limit the number of solutions as we then not only aim to minimize the data misfit cost functional but also aim to minimize other cost functionals which are beneficial for the design process.

Finally, it should be noted that (3.8) represents the simplest form of the inverse design formulation. As will be seen later, the desired field specifications are typically given as normalized power patterns. Note that power is a phaseless (magnitude-only) quantity. Thus, this is different than the formulation in (3.8) where the desired specification is given in terms of complex (magnitude and phase) $\boldsymbol{E}_{\text{des}}$. It is well-known that phaseless inverse problems are nonlinear and are generally more difficult to be solved [66, 67]

3.4 Interior Field Constraint

With the field data assigned outside D, no internal field (internal with respect to D) constraint has been made. That is, the solution of the inverse source problem would fit the given field data that located outside D, and create arbitrary field inside D. Herein, the Love's equivalent condition [57, 62] is applied, which enforces the internal fields to be zero. This extra requirement would bring several benefits. First of all, extra field specifications would enhance the stability of the solution by annihilating some of the non-radiating sources from the original problem, as these sources might not produce null field at the internal locations. Secondly, assuming the unit normal vector $\hat{n}$, which is pointing outward of D, the boundary conditions in (3.1) are simplified to

$$\boldsymbol{J} = \hat{n} \times \boldsymbol{H}^{+}, \tag{3.11a}$$

$$\boldsymbol{M} = -\hat{n} \times \boldsymbol{E}^{+}. \tag{3.11b}$$

As can be seen, this directly relates the equivalent current densities to the tangential fields outside of the boundary. This is important as the tangential fields are required for metasurface design according to the GSTCs. Lastly, as will be shown in Chapter 4, another regularization term will be added to eliminate some other non-radiating sources by reducing the spatial variation of the sources. If Love's condition is enforced, this direct link between the sources and the tangential fields will result in smoother transmitted fields as well, which is beneficial for metasurface design. This is due to the fact that the unit cell design procedure is performed under periodic assumption (local periodicity approximation). That is, the properties of each unit cell, such as surface susceptibilities or scattering parameters, are obtained by simulating the individual unit cell under periodic boundary condition in a full wave solver such as Ansys HFSS.

Finally, it should be noted that in an inverse source approach, the currents are found

numerically, and we need to make sure that they are consistent with Maxwell's equations. The enforcement of Love's condition is a means to make sure that the reconstructed currents are consistent with Maxwell's equations [62]. In particular, in [68], it has been shown that the enforcement of Love's condition is not only required for reflectionless metasurfaces, but is also necessary to obtain a desired reflection as well as a desired transmission.

Chapter 4

Inversion Framework

In this chapter, a general electromagnetic (EM) inversion framework for metasurface design is presented under both 2D and 3D assumptions. Note that the 2D assumption is still practical as the metasurface can be made fully periodic in one direction and then have spatial modulation in the other direction. Most of the works in the area of metasurface design have been done under the 2D assumption. In particular, the 2D work presented in this Chapter follows the work in [28, 30–32], which is presented here for the sake of completeness. This chapter then extends these works by providing an analytical expression for a component of the inversion algorithm (known as step length) which was chosen in an *ad hoc* way in those previous works. In addition, in this chapter, the inverse metasurface design is extended to 3D. Note that in the 3D case, we can have spatial modulation along both dimensions of the metasurface. That is, for a metasurface lying on the uv plane, the surface susceptibility χ will be a function of u and v coordinates, i.e., $\chi(u, v)$. To the best of the author's knowledge, this is the first time that this inverse source approach has been developed for the 3D case.

4.1 Introduction

As noted earlier in the thesis, EM metasurfaces are quasi two-dimensional structures with subwavelength inclusions. These inclusions are typically metallic in the microwave frequency range. Metasurfaces provide systematic transformations of the EM waves that impinge onto them. This is achieved by locally altering the amplitude, phase and/or polarization of the incoming EM waves. As we already described, there are two necessary steps for metasurface design, namely, macroscopic design and microscopic design. The macroscopic design focuses on solving for surface properties, such as surface susceptibilities, that support the desired transformation. On the other hand, the microscopic design focuses on realizing these surface properties with physical unit cell structures. The macroscopic design procedure, which is the focus of this thesis, requires the knowledge of the tangential EM fields over the faces of the metasurface. However, in many practical cases, these fields, especially the transmitted fields, may not be directly available. For example, five possible cases for the transmitted field information were noted in [28], namely:

1. Analytical expressions of the transmitted field (e.g., plane wave refraction)

2. Complex (magnitude and phase) field on a canonical surface and canonical shaped metasurface

3. Complex (magnitude and phase) field on an arbitrary surface and/or arbitrary shaped metasurface

4. Magnitude-only (phaseless) field on an arbitrary surface and/or arbitrary shaped metasurface

5. Far-field criteria such as main beam direction(s), half-power beamwidth(s), null direction(s), and side lobe levels.

In the cases listed above, only the first two cases could retrieve the transmitted tangential field on the metasurface easily. The other three cases would require the use of other techniques to find the transmitted tangential field on the surface of the metasurface. Note that in many design scenarios, the user only cares about obtaining a desired power pattern which is a phaseless quantity. Thus, the first two cases cannot support this situation as they require phase information. In addition, assuming a phase distribution would unnecessarily limit the scope of the achievable solutions. That is why the use of phaseless approaches are desired.

Herein, since far-field criteria can be transformed into far-field power patterns (phaseless quantity) [28, 69], and practical metasurfaces are mostly flat or curved, an inversion framework for solving flat metasurface design problem for the third and fourth cases will be provided based on [28, 30–32]. These techniques are all iterative and at each iteration they require the choice of the optimization step length. However, they have so far relied on *ad hoc* approaches to determine this step length which is not effective and cannot result in an *automated* design approach. Herein, the analytical step length that was missing from the optimization method used in [30, 31] will be derived and provided. Moreover, the inverse metasurface design technique is extended to 3D so as to be able to handle desired power patterns in two fundamental cuts. (In the 2D case, we can only handle desired power patterns in one cut.)

4.2 Problem Statement

Consider a transmitting metasurface lying on the xz plane as shown in Figure 4.1 and the orientation implies that $\hat{u} = \hat{z}$, $\hat{v} = \hat{x}$, and $\hat{n} = \hat{y}$. Assuming that the incident field, $\mathbf{\Psi}^{\text{inc}}$, produced by the source is known on the input side of the metasurface, and the desired

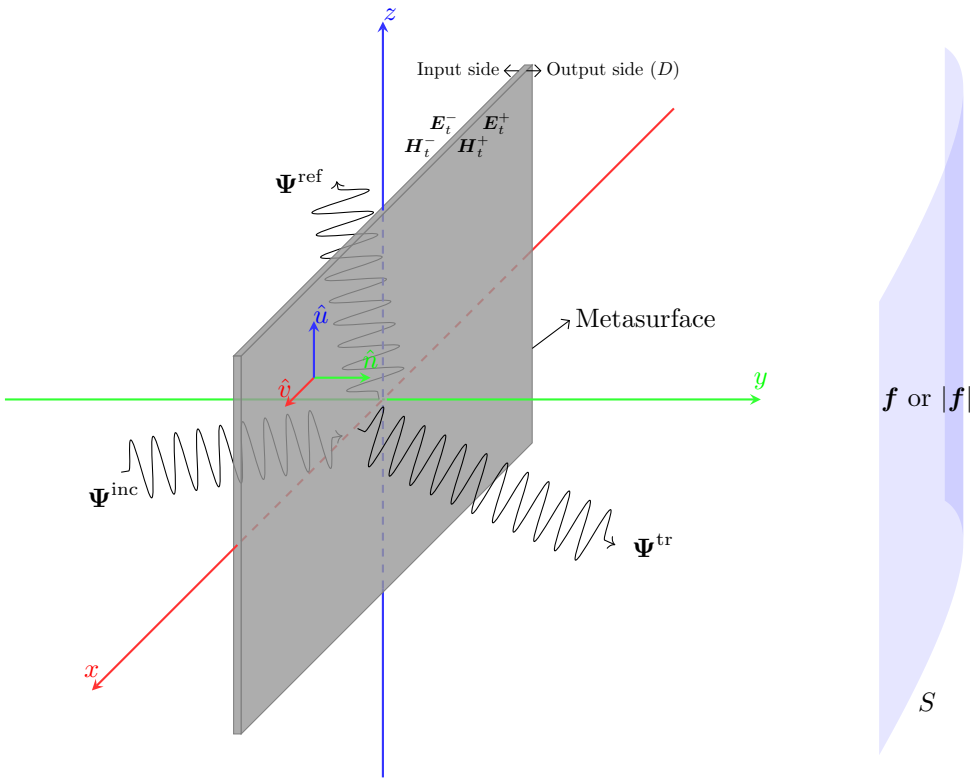

Fig. 4.1: A metasurface is designed to transform the known incident field, $\boldsymbol{\Psi}^{\text{inc}}$, to the desired field quantities, $\boldsymbol{f}$ or $|\boldsymbol{f}|$, at region S. The tangential fields on the both sides of the metasurface are required for the design, and more specifically, the tangential output fields, $\boldsymbol{E}_t^+$ and $\boldsymbol{H}_t^+$, are inversely found through $\boldsymbol{f}$ or $|\boldsymbol{f}|$.

electric or magnetic field, with or without phase information[1], is known on the region S instead of the transmitted side of the metasurface, the goal is to find the susceptibility profile for the metasurface, such that the metasurface could transform the known incident field to a transmitted field that matches desired magnitude-only electric or magnetic field pattern[2]. Also, note that magnitude-only field patterns are equivalent to power patterns as power density is a phaseless quantity and is related to $|\boldsymbol{f}|^2$. Therefore, they can be used interchangeably throughout this thesis.

[1]To clarify the difference, desired field with phase information (i.e., a complex field value) is denoted by $\boldsymbol{f}$, and amplitude-only desired field is denoted by $|\boldsymbol{f}|$, where $|\cdot|$ represents the absolute value.

[2]The reason that matching the pattern rather than matching the exact field values is required is that once the pattern is matched, matching the exact field values can be achieved by simply adjusting the power of the incident field.

4.3 Methodology

In this section, the procedure to solve the proposed metasurface macroscopic design problem is described.

4.3.1 Finding the Tangential Fields

As can be seen in the GSTC equations, the tangential fields on both sides of the metasurface are required to compute the corresponding surface susceptibility values χ. In the following, the incident and transmitted sides of the metasurface will be referred as the input and output sides, respectively. Therefore, it is necessary to first find the tangential input and output fields.

Tangential Input Fields

As the metasurface described in Figure 4.1 aims to alter the incident wave through transmission, it is rational to assume that no reflection is desired, and therefore, the tangential input fields are known quantities as they equal to the tangential incident fields, i.e., $\boldsymbol{E}_t^- = \boldsymbol{E}_t^{\text{inc}}$ and $\boldsymbol{H}_t^- = \boldsymbol{H}_t^{\text{inc}}$. However, we note that there might be cases that the designer would like to create a desired reflection in addition to a desired transmission. However, this is not discussed within this thesis and we limit ourselves to reflectionless metasurfaces. Since these metasurfaces are used for transmission, they are typically referred to as Huygens' metasurfaces [70].

Tangential Output Fields

The tangential output fields are not directly available since the desired fields (or more accurately desired power patterns) are defined over S instead of on the output side of the metasurface. To this end, the equivalent surface currents, $\boldsymbol{J}$ and $\boldsymbol{M}$, on the output side of the metasurface will be found by using the approach described in Chapter 3, with Love's

equivalence principle applied. Notice that extra regularization terms are needed to ensure that the metasurface is practical, and the details of finding these currents are later presented in Section 4.4. Once the currents are obtained, the tangential output fields can be found by rearranging the boundary conditions in (3.11) as[3]

$$\boldsymbol{E}_t^+ = \hat{y} \times \boldsymbol{M}, \tag{4.1a}$$

$$\boldsymbol{H}_t^+ = -\hat{y} \times \boldsymbol{J}. \tag{4.1b}$$

However, in practice, the above equation needs to be written as

$$\boldsymbol{E}_t^+ = \alpha\ \hat{y} \times \boldsymbol{M}, \tag{4.2a}$$

$$\boldsymbol{H}_t^+ = -\alpha\ \hat{y} \times \boldsymbol{J}, \tag{4.2b}$$

where α is a real-valued scalar to ensure that the *total* power conservation is satisfied [30]. Since the metasurface is passive and lossless, the total output power needs to be equal to the total input power. As will be demonstrated in Section 4.4, the choice of α will not change the resulting pattern.

4.3.2 Calculating the Susceptibility Profile

According to Section 2.2, the susceptibility profile of the metasurface is related to the tangential fields through the GSTCs. With the predefined coordinates shown in Figure 4.1, the GSTCs read

$$\begin{pmatrix} -\Delta H_x \\ \Delta H_z \end{pmatrix} = j\omega\varepsilon_0 \begin{pmatrix} \chi_{\mathrm{ee}}^{zz} & \chi_{\mathrm{ee}}^{zx} \\ \chi_{\mathrm{ee}}^{xz} & \chi_{\mathrm{ee}}^{xx} \end{pmatrix} \begin{pmatrix} E_{z,\mathrm{av}} \\ E_{x,\mathrm{av}} \end{pmatrix} + jk_0 \begin{pmatrix} \chi_{\mathrm{em}}^{zz} & \chi_{\mathrm{em}}^{zx} \\ \chi_{\mathrm{em}}^{xz} & \chi_{\mathrm{em}}^{xx} \end{pmatrix} \begin{pmatrix} H_{z,\mathrm{av}} \\ H_{x,\mathrm{av}} \end{pmatrix}, \tag{4.3a}$$

[3]Note that $\hat{n}$ is now $\hat{y}$. Also, the identity $\boldsymbol{A} \times (\boldsymbol{B} \times \boldsymbol{C}) = \boldsymbol{B}(\boldsymbol{A} \cdot \boldsymbol{C}) - \boldsymbol{C}(\boldsymbol{A} \cdot \boldsymbol{B})$ is used where $\boldsymbol{A}$, $\boldsymbol{B}$, and $\boldsymbol{C}$ are arbitrary vectors and $\times$ denotes vector cross product and $\cdot$ denotes vector dot product.

$$\begin{pmatrix} \Delta E_x \\ -\Delta E_z \end{pmatrix} = j\omega\mu_0 \begin{pmatrix} \chi_{\mathrm{mm}}^{zz} & \chi_{\mathrm{mm}}^{zx} \\ \chi_{\mathrm{mm}}^{xz} & \chi_{\mathrm{mm}}^{xx} \end{pmatrix} \begin{pmatrix} H_{z,\mathrm{av}} \\ H_{x,\mathrm{av}} \end{pmatrix} + jk_0 \begin{pmatrix} \chi_{\mathrm{me}}^{zz} & \chi_{\mathrm{me}}^{zx} \\ \chi_{\mathrm{me}}^{xz} & \chi_{\mathrm{me}}^{xx} \end{pmatrix} \begin{pmatrix} E_{z,\mathrm{av}} \\ E_{x,\mathrm{av}} \end{pmatrix}, \tag{4.3b}$$

Although microscopic unit cell (meta-atom) designs are not considered, the unit cell design of a reciprocal, passive and lossless metasurface is generally preferred to avoid energy loss and using circuit components that require DC bias or more advanced fabrication. Moreover, the design of reciprocal metasurfaces is also preferred in this thesis. Therefore, herein, it is required that the metasurface is reciprocal, passive and lossless. Since the three-layer topology employed herein cannot support change of polarization, the metasurface is assumed to be non-gyrotropic as well. Combining the assumptions stated above and applying the requirements stated in Section 2.3 to fulfill the assumptions, the GSTCs become

$$\begin{pmatrix} -\Delta H_x \\ \Delta H_z \end{pmatrix} = j\omega\varepsilon_0 \begin{pmatrix} \chi_{\mathrm{ee}}^{zz} & 0 \\ 0 & \chi_{\mathrm{ee}}^{xx} \end{pmatrix} \begin{pmatrix} E_{z,\mathrm{av}} \\ E_{x,\mathrm{av}} \end{pmatrix} + jk_0 \begin{pmatrix} 0 & \chi_{\mathrm{em}}^{zx} \\ \chi_{\mathrm{em}}^{xz} & 0 \end{pmatrix} \begin{pmatrix} H_{z,\mathrm{av}} \\ H_{x,\mathrm{av}} \end{pmatrix}, \tag{4.4a}$$

$$\begin{pmatrix} \Delta E_x \\ -\Delta E_z \end{pmatrix} = j\omega\mu_0 \begin{pmatrix} \chi_{\mathrm{mm}}^{zz} & 0 \\ 0 & \chi_{\mathrm{mm}}^{xx} \end{pmatrix} \begin{pmatrix} H_{z,\mathrm{av}} \\ H_{x,\mathrm{av}} \end{pmatrix} + jk_0 \begin{pmatrix} 0 & -\chi_{\mathrm{em}}^{xz} \\ -\chi_{\mathrm{em}}^{zx} & 0 \end{pmatrix} \begin{pmatrix} E_{z,\mathrm{av}} \\ E_{x,\mathrm{av}} \end{pmatrix}. \tag{4.4b}$$

In the above equation, in accordance with Section 2.3, the susceptibility values need to satisfy

$$\begin{gathered} \chi_{\mathrm{ee}}^{zz}, \chi_{\mathrm{ee}}^{xx}, \chi_{\mathrm{mm}}^{zz}, \chi_{\mathrm{mm}}^{xx} \in \mathbb{R}, \\ \chi_{\mathrm{em}}^{zx}, \chi_{\mathrm{em}}^{xz} \in \mathbb{I}, \end{gathered} \tag{4.5}$$

where $\mathbb{R}$ denotes the real number set and $\mathbb{I}$ denotes the imaginary number set. For simplicity, one can align the polarization of the tangential fields with the predefined coordinate system. For example, if the incident fields are TE (TM$_z$) fields, the GSTCs in (4.4) can be further simplified to

$$H_x^- - H_x^+ = \frac{j\omega\varepsilon_0}{2}\chi_{\mathrm{ee}}^{zz}\left(E_z^+ + E_z^-\right) + \frac{jk_0}{2}\chi_{\mathrm{em}}^{zx}\left(H_x^+ + H_x^-\right), \tag{4.6a}$$

$$E_z^- - E_z^+ = \frac{j\omega\mu_0}{2}\chi_{\mathrm{mm}}^{xx}\left(H_x^+ + H_x^-\right) - \frac{jk_0}{2}\chi_{\mathrm{em}}^{zx}\left(E_z^+ + E_z^-\right). \tag{4.6b}$$

As mentioned in Section 2.3.4, this problem is well defined and there will be a unique set of susceptibility values that can realize the desired field transformation.

4.3.3 Implementing the Susceptibility Profile

The three-layer admittance sheet topology described in Section 2.4.1 is used to implement the acquired susceptibility profile. Firstly, according to Section 2.4, assuming a TE (TM_z) incident field, the field transformation delivered by the metasurface unit cell can be represented by a two-port network using transmission parameters as [49]

$$\begin{pmatrix} E_z^- \\ H_x^- \end{pmatrix} = \begin{pmatrix} T_{11} & T_{12} \\ T_{21} & T_{22} \end{pmatrix} \begin{pmatrix} E_z^+ \\ H_x^+ \end{pmatrix}, \tag{4.7}$$

where[4]

$$T_{11} = \frac{\zeta\tau\chi_{\mathrm{ee}}^{zz}\chi_{\mathrm{mm}}^{xx} + \left(1 - \xi\chi_{\mathrm{em}}^{zx}\right)^2}{1 - \zeta\tau\chi_{\mathrm{ee}}^{zz}\chi_{\mathrm{mm}}^{xx} - \left(\xi\chi_{\mathrm{em}}^{zx}\right)^2}, \tag{4.8a}$$

$$T_{12} = \frac{2\tau\chi_{\mathrm{mm}}^{xx}}{1 - \zeta\tau\chi_{\mathrm{ee}}^{zz}\chi_{\mathrm{mm}}^{xx} - \left(\xi\chi_{\mathrm{em}}^{zx}\right)^2}, \tag{4.8b}$$

$$T_{21} = \frac{2\zeta\chi_{\mathrm{ee}}^{zz}}{1 - \zeta\tau\chi_{\mathrm{ee}}^{zz}\chi_{\mathrm{mm}}^{xx} - \left(\xi\chi_{\mathrm{em}}^{zx}\right)^2}, \tag{4.8c}$$

$$T_{22} = \frac{\zeta\tau\chi_{\mathrm{ee}}^{zz}\chi_{\mathrm{mm}}^{xx} + \left(1 + \xi\chi_{\mathrm{em}}^{zx}\right)^2}{1 - \zeta\tau\chi_{\mathrm{ee}}^{zz}\chi_{\mathrm{mm}}^{xx} - \left(\xi\chi_{\mathrm{em}}^{zx}\right)^2}, \tag{4.8d}$$

and

$$\zeta = \frac{j\omega\varepsilon_0}{2},\ \xi = \frac{jk_0}{2},\ \tau = \frac{j\omega\mu_0}{2}. \tag{4.9}$$

[4]We repeat some of the equations noted in Section 2.4 with the specified coordinate considered herein. That is, we replace u and v by the coordinates considered in Figure 2.1.

Assuming that the two substrates are identical, the three purely-imaginary (i.e., lossless and passive) admittance values can be calculated as [48, 49]

$$Y_1 = \frac{T_{22} - jZ_0 \sin(\beta t)\cos(\beta t)Y_2 + \sin^2(\beta t) - \cos^2(\beta t)}{2jZ_0 \sin(\beta t)\cos(\beta t) - Z_0^2 \sin^2(\beta t)Y_2}, \tag{4.10a}$$

$$Y_2 = \frac{T_{12} - 2jZ_0 \sin(\beta t)\cos(\beta t)}{-Z_0^2 \sin^2(\beta t)}, \tag{4.10b}$$

$$Y_3 = \frac{T_{11} - jZ_0 \sin(\beta t)\cos(\beta t)Y_2 + \sin^2(\beta t) - \cos^2(\beta t)}{2jZ_0 \sin(\beta t)\cos(\beta t) - Z_0^2 \sin^2(\beta t)Y_2}, \tag{4.10c}$$

where β denotes the phase constant in the dielectric substrate, t denotes the thickness of the substrate, and Z_0 denotes the characteristic impedance of the dielectric substrate.[5]

4.4 Numerical Implementation

The procedure described in the previous section provides explicit calculation for all the quantities needed for the proposed problem except for the equivalent surface current densities. As these unknown current densities are difficult to be analytically calculated, they are inferred from user-specified field specifications (with or without phase) through an EM inversion algorithm. In this section, the procedure for numerically finding the current densities will be elaborated. Since this thesis builds on the work presented in [32], it follows a similar style of presentation for the numerical implementation.

4.4.1 Creating the Vector of Unknowns

Let us begin this section by emphasizing one more time that only the tangential field components, E_z^+ and H_x^+, are concerned in the design process, and also let us emphasize that according to (3.11), the equivalent electric and magnetic current densities are directly related to the output tangential fields as $J_z = -H_x^+$ and $M_x = -E_z^+$. In order to apply

[5] Although we typically have small losses in the substrate, the substrate is considered to be lossless in the above calculation. But, in the full-wave simulation in Ansys HFSS, the loss will be considered.

an EM inversion algorithm to numerically solve for the current density components, the metasurface needs to be discretized into N unit cells, and the current density components can then be discretized and approximated as

$$J_z(\boldsymbol{r}) \approx \sum_{n=1}^{N} J_n f_n(\boldsymbol{r}), \tag{4.11a}$$

$$M_x(\boldsymbol{r}) \approx \sum_{n=1}^{N} M_n f_n(\boldsymbol{r}), \tag{4.11b}$$

where J_n and M_n are the complex coefficients, and $f_n(\boldsymbol{r})$ is the pulse basis function that equals unity when $\boldsymbol{r}$ is inside n^{th} unit cell and zero elsewhere. Let

$$\mathbf{J} = \begin{bmatrix} J_1 \\ J_2 \\ \cdots \\ J_N \end{bmatrix} \in \mathbb{C}^{N\times 1}, \quad \mathbf{M} = \begin{bmatrix} M_1 \\ M_2 \\ \cdots \\ M_N \end{bmatrix} \in \mathbb{C}^{N\times 1} \tag{4.12}$$

be the vectors that contain the coefficients. As in [30], these vectors can be expressed in terms of their real and imaginary components as[6]

$$\mathbf{J} = \mathbf{J}_{\mathrm{R}} + j\mathbf{J}_{\mathrm{I}}, \tag{4.13a}$$

$$\mathbf{M} = \mathbf{M}_{\mathrm{R}} + j\mathbf{M}_{\mathrm{I}}. \tag{4.13b}$$

[6] As can be seen in [30], the main reason for decomposing the equivalent currents into their real and imaginary parts is to develop a cost functional for the enforcement of the local power conservation (LPC) constraint.

Finally, similar to [32], the vector of unknowns, $\mathbf{x}$, is constructed by concatenating the real and imaginary parts of the coefficients as

$$\mathbf{x} = \begin{bmatrix} \mathbf{J}_{\mathrm{R}} \\ \mathbf{J}_{\mathrm{I}} \\ \mathbf{M}_{\mathrm{R}} \\ \mathbf{M}_{\mathrm{I}} \end{bmatrix} \in \mathbb{R}^{4N\times 1}. \tag{4.14}$$

Notice that with this arrangement, the unknown is a real-valued vector that could simplify some of the calculations later on.

4.4.2 Creating the Forward Operator

The forward operator is an operator that accepts a set of known currents and calculate their effect in the region of interest (ROI). The effect is typically electric or magnetic fields in the far-field zone. However, the formulation presented here also covers the electric and magnetic fields in the near-field zone. The forward operator is created based on the integral equations in (3.3). Assuming that the observation point $\boldsymbol{r}$ is in ROI, i.e, $\boldsymbol{r} \in$ ROI, based on the EFIE and the discretized current densities, the relationship between the unknowns and the electric field at the observation point, $\boldsymbol{E}(\boldsymbol{r})$, can be expressed as

$$\begin{aligned} \boldsymbol{E}(\boldsymbol{r}) = -j\eta_0 k_0 \int_D \widetilde{G}_0(\boldsymbol{r},\boldsymbol{r}') \cdot \hat{z} \sum_{n=1}^{N} J_n f_n\left(\boldsymbol{r}'\right) \mathrm{d}x'\mathrm{d}z' \\ + \int_D \hat{x} \sum_{n=1}^{N} M_n f_n\left(\boldsymbol{r}'\right) \times \nabla g_0(\boldsymbol{r},\boldsymbol{r}')\mathrm{d}x'\mathrm{d}z', \end{aligned} \tag{4.15}$$

where $\boldsymbol{r} \in$ ROI, and $\boldsymbol{r}'$ spans the outside surface of the metasurface denote by D, i.e., $\boldsymbol{r}' \in D$. The discrete forward operator $\mathbf{A}$ is then created such that $\mathbf{Ax}$ produces a vector of electric field component values over the ROI. The details of constructing the linear operator $\mathbf{A}$ can

be found in Appendix A. As will be seen, the selection of the Green's function in (4.15) depends on whether 2D assumption is applied, and therefore, the resulting operator will be different. In addition, another forward operator $\mathbf{A}_{\text{Love}}$ is created in a similar manner such that $\mathbf{A}_{\text{Love}}\mathbf{x}$ produces a vector of E_z values at locations where Love's equivalence principle is enforced[7]. Note that (3.11) is valid under Love's condition, and thus, it makes sense to have an operator that can be later used to enforce the Love's equivalence principle. To create this operator, the observation point $\boldsymbol{r}$ will span the Love's surface according to [28, 57, 62].

4.4.3 Forming the Data Misfit Cost Functional

The data misfit cost functional quantifies the relative difference between the user specified discrete field data $\mathbf{f}$ and the field produced by the equivalent current densities at the region of interest (ROI). Herein, we denote the ROI by S for brevity. To match complex field data, the data misfit cost functional is expressed as

$$\mathcal{C}_{\text{data}}(\mathbf{x}) = \frac{\|\mathbf{A}\mathbf{x} - \mathbf{f}\|_S^2}{M\|\mathbf{f}\|_S^2}, \tag{4.16}$$

where M denotes the number of discrete field data and it is presented for the purpose of normalization and $\|\cdot\|_S$ represents the L_2 norm taken over the domain S.[8] Similarly, to match amplitude-only field data (i.e., power patterns), the data misfit cost functional is expressed as

$$\mathcal{C}_{\text{data}}(\mathbf{x}) = \frac{\left\| |\mathbf{A}\mathbf{x}|^2 - |\mathbf{f}|^2 \right\|_S^2}{M\left\| |\mathbf{f}|^2 \right\|_S^2}. \tag{4.17}$$

[7] Herein, the null fields are enforced on the input side of the metasurface.

[8] Compared to previous works in our group, e.g., [32], we have intentionally added the parameter M in the data misfit cost functional to provide better balance between this cost functional, and the remaining cost functionals. From the experience of the author, this leads to an easier choice for the regularization parameters. In particular, the author has observed that by this particular implementation, an appropriate weight for the LPC cost functional is around unity. Intuitively, this is reasonable as the LPC cost functional for the design of lossless and passive metasurfaces is as important as the data misfit cost functional.

Minimizing this functional reduces the difference between the desired magnitude-only field and the magnitude-only field produced by the equivalent current densities. That is, it represents the power pattern mismatch, or simply the data misfit.

4.4.4 Forming the Love's Equivalence Principle Cost Functional

Similar to the data misfit cost functional, the Love's equivalence principle cost functional quantifies the electric field values at locations where null fields are desired. Similar to [31], it is constructed as[9]

$$\mathcal{C}_{\text{Love}}(\mathbf{x}) = \frac{\|\mathbf{A}_{\text{Love}}\mathbf{x}\|^2}{L}, \tag{4.18}$$

where L denotes the number of testing points that enforces null fields. If this functional is minimized, the relationship between the equivalent sources and the output tangential fields in (4.2) is then valid.

4.4.5 Forming the Local Power Conservation Cost Functional

The local power conservation (LPC) [29] constraint is needed to be met to arrive at lossless and passive metasurfaces. This requires ensuring that the real power perpendicular to the unit cell on its input and output sides are the same. To this end, we have utilized the LPC cost functional derived in [30]. This cost functional aims to minimize the discrepancy between the real power entering a given unit cell in the perpendicular direction and the real power exiting that unit cell in the perpendicular direction. Thus, to enforce LPC, one must satisfy

$$\frac{1}{2}\text{Re}\left(\boldsymbol{E}_t^- \times \boldsymbol{H}_t^{-*}\right) = \frac{1}{2}\text{Re}\left(\boldsymbol{E}_t^+ \times \boldsymbol{H}_t^{+*}\right) \tag{4.19}$$

[9]The reason for normalizing this cost functional with L is the same as the reason presented in the previous footnote. In addition, we would like to note that in some other works, the Love's principle has been incorporated directly into the data misfit cost functional by augmenting the data operator, e.g. in [28].

at each unit cell, that is, $p_n^{\text{in}} = p_n^{\text{out}}$. The input power density for the n^{th} unit cell can be approximated as

$$p_n^{\text{in}} \approx \frac{1}{2}\text{Re}\left(E_{z,n}^{-}H_{x,n}^{-*}\right), \tag{4.20}$$

where $E_{z,n}^{-}$ and $H_{x,n}^{-}$ are measured at the centroid of the n^{th} unit cell. Notice that the input power densities are known quantities, and the vector containing these values will be denoted as $\mathbf{p}^{\text{in}}$. Similarly, the output power density for the n^{th} unit cell can be approximated as

$$p_n^{\text{out}} \approx \frac{1}{2}\text{Re}\left(E_{z,n}^{+}H_{x,n}^{+*}\right), \tag{4.21}$$

which, according to the equations in (4.2) and (4.11), can be written in terms of the coefficients as

$$\frac{1}{2}\text{Re}\left(E_{z,n}^{+}H_{x,n}^{+*}\right) = \frac{\alpha^2}{2}\text{Re}\left(M_n J_n^*\right). \tag{4.22}$$

The vector that contains the output power densities can then be written as

$$\mathbf{p}^{\text{out}} = \frac{\alpha^2}{2}\text{Re}\left(\mathbf{M} \odot \mathbf{J}^*\right), \tag{4.23}$$

where $\odot$ denotes the element-wise Hadamard product. Separating the real and imaginary parts of the coefficients, (4.23) becomes[10]

$$\begin{aligned}\mathbf{p}^{\text{out}} &= \frac{\alpha^2}{2}\text{Re}\left[(\mathbf{M}_{\text{R}} + j\mathbf{M}_{\text{I}}) \odot (\mathbf{J}_{\text{R}} - j\mathbf{J}_{\text{I}})\right] \\ &= \frac{\alpha^2}{2}\left(\mathbf{J}_{\text{R}} \odot \mathbf{M}_{\text{R}} + \mathbf{J}_{\text{I}} \odot \mathbf{M}_{\text{I}}\right).\end{aligned} \tag{4.24}$$

[10] At this point, we would like to remind the reader about the reason behind decomposing the unknown equivalent currents into their real and imaginary parts. As done in [30], this is needed to derive the LPC cost functional.

Now, to satisfy the *total* power conservation, i.e., $\text{sum}\left(\mathbf{p}^{\text{in}}\right) = \text{sum}\left(\mathbf{p}^{\text{out}}\right)$, α is calculated as [30]

$$\alpha = \left(\frac{\text{sum}\left(\mathbf{p}^{\text{in}}\right)}{\frac{1}{2}\text{sum}\left(\mathbf{J}_{\text{R}} \odot \mathbf{M}_{\text{R}} + \mathbf{J}_{\text{I}} \odot \mathbf{M}_{\text{I}}\right)} \right)^{\frac{1}{2}}. \tag{4.25}$$

Instead of strictly enforcing LPC which would potentially eliminate some of the solution sets, the cost functional associated with LPC,

$$\mathcal{C}_{\text{LPC}}(\mathbf{x}) = \frac{\left\| \mathbf{J}_{\text{R}} \odot \mathbf{M}_{\text{R}} + \mathbf{J}_{\text{I}} \odot \mathbf{M}_{\text{I}} - \frac{2}{\alpha^2}\mathbf{p}^{\text{in}} \right\|_D^2}{N \left\| \frac{2}{\alpha^2}\mathbf{p}^{\text{in}} \right\|_D^2}, \tag{4.26}$$

is minimized to reduce the difference between the input and output power. As will be seen, in our 3D implementation, we are concerned with the main (co-pol) polarization, and therefore, we will utilize the same LPC cost functional (originally developed for 2D [30]) for 3D. Obviously, we will deal with more unit cells in 3D as compared to the 2D case.

Note that enforcing LPC this way results in slightly different input and output power, and even if LPC is strictly enforced, the input and output power might still be slightly different due to precision error. This will cause problems when calculating the susceptibility profile and the admittance values, since the passive and lossless assumption of the metasurface no longer *perfectly* holds. This will result in χ_{em}^{zx} to have a non-zero real part. (If the LPC is *perfectly* satisfied, χ_{em}^{zx} will have zero real part.) On the other hand, if the LPC is *sufficiently* satisfied, the real part of the resulting χ_{em}^{zx} will be insignificant comparing to its imaginary part, and therefore, passivity and losslessness can still be achieved by neglecting the real part of χ_{em}^{zx}. This is the situation that happens in the inversion process. Once we get a complex χ_{em}^{zx}, we ignore its (small) real part in the process of implementing the corresponding three-layer admittance model.

4.4.6 Forming the Total Variation Regularization Term

As mentioned before, the Green's function used in (4.15) acts like a low-pass *spatial* filter. This can create non-radiating sources with high spatial frequency. That is, for a given solution $\bar{\mathbf{x}}$, we can also have $\bar{\mathbf{x}} + \mathbf{x}_{\mathrm{NR}}$ as another solution where $\mathbf{x}_{\mathrm{NR}}$ represents a non-radiating (NR) component. Meanwhile, since the output tangential fields are directly related to the equivalent current densities (with Love's equivalent principle enforced), a spatially smoother solution would better support the periodic assumption of three-layer admittance sheet topology. Therefore, among different possible solutions, it makes sense to favour the one that has smoother field variations across the metasurface. This is sometimes referred to as quasi-periodicity assumption. To this end, we might use penalty terms (regularization terms) that favour smoother solutions. For this, one candidate is the use of total variation (TV) regularization term that was first used in [31] for cascaded metasurface design.

The TV regularization term quantifies the spatial variation of the current densities, and it is formulated as

$$\mathcal{C}_{\mathrm{TV}}(\mathbf{x}) = \frac{\|\mathbb{V}(\mathbf{x})\|_D^2}{N}, \tag{4.27}$$

where the operator $\mathbb{V}$ takes the length of the gradient of the real and imaginary parts of current densities *separately*, which can be explicitly written as[11]

$$\mathbb{V}(\mathbf{x}) \triangleq \begin{bmatrix} |\nabla \mathbf{J}_{\mathrm{R}}| \\ |\nabla \mathbf{J}_{\mathrm{I}}| \\ |\nabla \mathbf{M}_{\mathrm{R}}| \\ |\nabla \mathbf{M}_{\mathrm{I}}| \end{bmatrix} = \begin{bmatrix} \sqrt{\left(\frac{\partial}{\partial x}\mathbf{J}_{\mathrm{R}}\right)^2 + \left(\frac{\partial}{\partial z}\mathbf{J}_{\mathrm{R}}\right)^2} \\ \sqrt{\left(\frac{\partial}{\partial x}\mathbf{J}_{\mathrm{I}}\right)^2 + \left(\frac{\partial}{\partial z}\mathbf{J}_{\mathrm{I}}\right)^2} \\ \sqrt{\left(\frac{\partial}{\partial x}\mathbf{M}_{\mathrm{R}}\right)^2 + \left(\frac{\partial}{\partial z}\mathbf{M}_{\mathrm{R}}\right)^2} \\ \sqrt{\left(\frac{\partial}{\partial x}\mathbf{M}_{\mathrm{I}}\right)^2 + \left(\frac{\partial}{\partial z}\mathbf{M}_{\mathrm{I}}\right)^2} \end{bmatrix}, \tag{4.28}$$

and the partial derivatives are numerically calculated using the central difference approxi-

[11] We would like to remind the reader that it is assumed that the metasurface lies in the xz plane for the 3D case.

mation. With the 2D assumption, for example $\frac{\partial}{\partial z} = 0$, this functional is simplified as

$$\mathcal{C}_{\mathrm{TV}}(\mathbf{x}) = \frac{\|D_x(\mathbf{x})\|_D^2}{N}, \tag{4.29}$$

where D_x is a operator that computes the partial derivative of the real and imaginary current density components separately, which can be explicitly written as

$$D_x(\mathbf{x}) \triangleq \begin{bmatrix} \frac{\partial}{\partial x}\mathbf{J}_{\mathrm{R}} \\ \frac{\partial}{\partial x}\mathbf{J}_{\mathrm{I}} \\ \frac{\partial}{\partial x}\mathbf{M}_{\mathrm{R}} \\ \frac{\partial}{\partial x}\mathbf{M}_{\mathrm{I}} \end{bmatrix}. \tag{4.30}$$

Minimizing this functional penalizes solutions with rapid spatial variations, resulting in both less non-radiating sources and eventually a metasurface with more uniformly distributed unit cells.

4.4.7 Solving the Minimization Problem

The unknowns are determined by minimizing the total cost functional that is constructed as

$$\mathcal{C}(\mathbf{x}) = \mathcal{C}_{\mathrm{data}}(\mathbf{x}) + w_{\mathrm{Love}}\mathcal{C}_{\mathrm{Love}}(\mathbf{x}) + w_{\mathrm{LPC}}\mathcal{C}_{\mathrm{LPC}}(\mathbf{x}) + w_{\mathrm{TV}}\mathcal{C}_{\mathrm{TV}}(\mathbf{x}), \tag{4.31}$$

where w_{Love}, w_{LPC} and w_{TV} are three real-valued weighing parameters that controls the relative importance between the three functionals. (As noted earlier, the specific choice of the normalization parameters in the above cost functionals has a beneficial consequence: the weight w_{LPC} can be typically chosen to be around unity.) Herein, the proposed minimization problem is solved using the nonlinear conjugate gradient method. This iterative method

updates the vector of unknowns as

$$\mathbf{x}_{k+1} = \mathbf{x}_k + \beta_k \mathbf{v}_k, \tag{4.32}$$

where $\mathbf{x}_k$ denotes the predicted solution at the k_{th} iteration, β_k is the real-valued step length, and the vector $\mathbf{v}_k$ is the search direction at the k^{th} iteration. Similar to [32], we employ the Polak-Ribière conjugate gradient method [71], which can be calculated as

$$\mathbf{v}_k = -\mathbf{g}_k + \frac{(\mathbf{g}_k - \mathbf{g}_{k-1})^\dagger \mathbf{g}_k}{\mathbf{g}_{k-1}^\dagger \mathbf{g}_{k-1}} \mathbf{v}_{k-1}. \tag{4.33}$$

In the above equation, $\mathbf{g}_k$ represents the gradient of $\mathcal{C}(\mathbf{x})$ with respect to $\mathbf{x}$ at the k^{th} iteration and the superscript † denotes the Hermitian (complex conjugate transpose) operator. Now to apply (4.32) to update the solution, the gradient of the total cost functional $\mathbf{g}$ and the step length β must be determined.

Determining the Gradient

To determine $\mathbf{g}$, one can individually calculate the gradient for the three cost functionals. If complex field data are given, the gradient of (4.16) can be calculated as

$$\mathbf{g}_{\text{data}}(\mathbf{x}) = \frac{2\text{Re}\left[\mathbf{A}^\dagger (\mathbf{A}\mathbf{x} - \mathbf{f})\right]}{M\|\mathbf{f}\|_S^2}. \tag{4.34}$$

If amplitude-only field data[12] are given, the gradient of (4.17) can be calculated as [31]

$$\mathbf{g}_{\text{data}}(\mathbf{x}) = \frac{4\text{Re}\left[\mathbf{A}^\dagger (\mathbf{r}_{\text{data}} \odot \mathbf{A}\mathbf{x})\right]}{M\left\| |\mathbf{f}|^2 \right\|_S^2}, \tag{4.35}$$

[12] In the region of interest is in the far-field zone, this will correspond to desired power patterns.

where $\mathbf{r}_{\text{data}}$ is the residual vector for the data misfit cost functional that is defined as

$$\mathbf{r}_{\text{data}}(\mathbf{x}) \triangleq |\mathbf{A}\mathbf{x}|^2 - |\mathbf{f}|^2. \tag{4.36}$$

The gradient of the Love's equivalence principle cost functional in (4.18) is calculated as [31]

$$\mathbf{g}_{\text{Love}}(\mathbf{x}) = \frac{2\text{Re}\left[\mathbf{A}_{\text{Love}}^{\dagger}\mathbf{A}_{\text{Love}}\mathbf{x}\right]}{L}. \tag{4.37}$$

The gradient of the LPC cost functional in equation (4.26) is derived as [31]

$$\mathbf{g}_{\text{LPC}}(\mathbf{x}) = \frac{2}{N\left\|\frac{2}{\alpha^2}\mathbf{p}^{\text{in}}\right\|_D^2}\begin{bmatrix}\mathbf{r}_{\text{LPC}} \odot \mathbf{M}_{\text{R}} \\ \mathbf{r}_{\text{LPC}} \odot \mathbf{M}_{\text{I}} \\ \mathbf{r}_{\text{LPC}} \odot \mathbf{J}_{\text{R}} \\ \mathbf{r}_{\text{LPC}} \odot \mathbf{J}_{\text{I}}\end{bmatrix}, \tag{4.38}$$

where the residual vector for the LPC cost functional, $\mathbf{r}_{\text{LPC}}$, is defined as

$$\mathbf{r}_{\text{LPC}}(\mathbf{x}) \triangleq \mathbf{J}_{\text{R}} \odot \mathbf{M}_{\text{R}} + \mathbf{J}_{\text{I}} \odot \mathbf{M}_{\text{I}} - \frac{2}{\alpha^2}\mathbf{p}^{\text{in}}. \tag{4.39}$$

The gradient of the total variation cost functional in equation (4.27) is derived as [31]

$$\mathbf{g}_{\text{TV}}(\mathbf{x}) = \frac{-2\mathbb{W}^2(\mathbf{x})}{N}, \tag{4.40}$$

where the operator $\mathbb{\nabla}^2$ takes the Laplacian of the real and imaginary parts of the current density components separately. That is,

$$\mathbb{\nabla}^2(\mathbf{x}) \triangleq \begin{bmatrix} \nabla^2\mathbf{J}_{\mathrm{R}} \\ \nabla^2\mathbf{J}_{\mathrm{I}} \\ \nabla^2\mathbf{M}_{\mathrm{R}} \\ \nabla^2\mathbf{M}_{\mathrm{I}} \end{bmatrix}, \tag{4.41}$$

and similar to (4.28), is numerically evaluated using central difference approximation. If 2D assumption is made ($\frac{\partial}{\partial z} = 0$), the gradient of the total variation cost functional is simplified as

$$\mathbf{g}_{\mathrm{TV}}(\mathbf{x}) = \frac{-2D_x^2(\mathbf{x})}{N}, \tag{4.42}$$

where the operator D_x^2 computes the second partial derivative of the real and imaginary current density components separately as

$$D_x^2(\mathbf{x}) \triangleq \begin{bmatrix} \frac{\partial^2}{\partial x^2}\mathbf{J}_{\mathrm{R}} \\ \frac{\partial^2}{\partial x^2}\mathbf{J}_{\mathrm{I}} \\ \frac{\partial^2}{\partial x^2}\mathbf{M}_{\mathrm{R}} \\ \frac{\partial^2}{\partial x^2}\mathbf{M}_{\mathrm{I}} \end{bmatrix}. \tag{4.43}$$

Finally the gradient of the total cost functional is calculated as

$$\mathbf{g} = \mathbf{g}_{\mathrm{data}} + w_{\mathrm{Love}}\mathbf{g}_{\mathrm{Love}} + w_{\mathrm{LPC}}\mathbf{g}_{\mathrm{LPC}} + w_{\mathrm{TV}}\mathbf{g}_{\mathrm{TV}} \tag{4.44}$$

Determining the Step length

The step length of the nonlinear conjugate gradient algorithm has been denoted by β_k in (4.32). This parameter is essential in controlling how much the optimization algorithm should incorporate the conjugate gradient direction $\mathbf{v}_k$ in the update process. Since the

derivation of the step length in the presence of the local power conservation (LPC) cost functional is a contribution of this thesis, a full derivation is presented herein.

In the nonlinear conjugate gradient (CG) optimization for inverse (passive and lossless) metasurface design, the choice of the step length has been considered in an *ad hoc* way. Originally, for the case of lossy or active metasurfaces, an analytical expression for the step length was derived [28]. However, when the LPC cost functional was added to the problem formulation to enforce lossless and passive metasurfaces [49], the analytical expressions for the CG direction and step length were not derived for the LPC-augmented cost functional. Consequently a global optimization approach (particle swarm optimization) in conjunction with the CG algorithm was used in a two-step fashion. Later, in [31], for the LPC-augmented cost functional, an analytical expression for the CG direction was derived. However, the step length was still chosen in an *ad hoc* fashion. For example, in [31], this step length has been changed from 100, 10, 1, 0.1, and 0.005 for different design examples. There are at least two shortcomings with this *ad hoc* choice of step length:

- This requires a trial-and-error approach, and thus can be time consuming for the designer.

- Even if the trial-and-error approach is successful to determine a reasonable step length, this step length is kept fixed during different iterations of the CG algorithm as was done in [31]. This is not ideal as the step length in the CG algorithm varies at different iterations. The change of step length as a function of the CG iteration ensures a faster convergence and possibly arriving at a better solution for the optimization problem.

To address the above issues, herein, we derive the analytical expression for the CG step length of the LPC-augmented cost functional. The analytical expression of the step length, which makes the minimization more efficient, can be found by minimizing $\mathcal{F}(\beta_k) = \mathcal{C}(\mathbf{x}_k + \beta_k \mathbf{v}_k)$ with respect to β_k. (Note that the step length β_k is a real number.) Similar to

calculating the gradient, the three cost functionals in terms of β_k are derived individually. If complex field data are given, the data misfit cost functional can be expressed as

$$\begin{aligned}\mathcal{F}_{\text{data}}(\beta_k) &= \mathcal{C}_{\text{data}}(\mathbf{x}_k + \beta_k \mathbf{v}_k) \\ &= \frac{\|\mathbf{A}(\mathbf{x}_k + \beta_k \mathbf{v}_k) - \mathbf{f}\|_S^2}{M\|\mathbf{f}\|_S^2} \\ &= \frac{\|\mathbf{A}\mathbf{v}_k\|_S^2 \beta_k^2 + 2\text{Re}\left[(\mathbf{A}\mathbf{v}_k)^\dagger (\mathbf{A}\mathbf{x}_k - \mathbf{f})\right] \beta_k + \|\mathbf{A}\mathbf{x}_k - \mathbf{f}\|_S^2}{M\|\mathbf{f}\|_S^2}.\end{aligned} \tag{4.45}$$

If amplitude-only field data are given, the data misfit cost functional can be expressed as a fourth order polynomial of β_k as [28, 72]

$$\begin{aligned}\mathcal{F}_{\text{data}}(\beta_k) &= \mathcal{C}_{\text{data}}(\mathbf{x}_k + \beta_k \mathbf{v}_k) \\ &= \frac{\left\| |\mathbf{A}(\mathbf{x}_k + \beta_k \mathbf{v}_k)|^2 - |\mathbf{f}|^2 \right\|_S^2}{M\left\| |\mathbf{f}|^2 \right\|_S^2} \\ &= \frac{\left\| |\mathbf{A}\mathbf{v}_k|^2 \beta_k^2 + 2\text{Re}\left[(\mathbf{A}\mathbf{x}_k) \odot (\mathbf{A}\mathbf{v}_k)^*\right] \beta_k + \mathbf{r}_{\text{data},k} \right\|_S^2}{M\left\| |\mathbf{f}|^2 \right\|_S^2} \\ &= a_{\text{data},4}\beta_k^4 + a_{\text{data},3}\beta_k^3 + a_{\text{data},2}\beta_k^2 + a_{\text{data},1}\beta_k + a_{\text{data},0},\end{aligned} \tag{4.46}$$

where

$$\begin{aligned} a_{\text{data},4} &= \frac{\left\| |\mathbf{A}\mathbf{v}_k|^2 \right\|_S^2}{M\left\| |\mathbf{f}|^2 \right\|_S^2},\ a_{\text{data},3} = \frac{4(|\mathbf{A}\mathbf{v}_k|^2)^{\text{T}}\text{Re}\left[(\mathbf{A}\mathbf{x}_k) \odot (\mathbf{A}\mathbf{v}_k)^*\right]}{M\left\| |\mathbf{f}|^2 \right\|_S^2}, \\ a_{\text{data},2} &= \frac{4\|\text{Re}\left[(\mathbf{A}\mathbf{x}_k) \odot (\mathbf{A}\mathbf{v}_k)^*\right]\|_S^2 + 2\mathbf{r}_{\text{data},k}^{\text{T}}|\mathbf{A}\mathbf{v}_k|^2}{M\left\| |\mathbf{f}|^2 \right\|_S^2}, \\ a_{\text{data},1} &= \frac{4\mathbf{r}_{\text{data},k}^{\text{T}}\text{Re}\left[(\mathbf{A}\mathbf{x}_k) \odot (\mathbf{A}\mathbf{v}_k)^*\right]}{M\left\| |\mathbf{f}|^2 \right\|_S^2},\ a_{\text{data},0} = \frac{\|\mathbf{r}_{\text{data},k}\|_S^2}{M\left\| |\mathbf{f}|^2 \right\|_S^2}. \end{aligned} \tag{4.47}$$

Similarly, the Love's equivalence principle cost functional in terms of β_k can be expressed

as

$$\begin{aligned}\mathcal{F}_{\text{Love}}(\beta_k) &= \mathcal{C}_{\text{Love}}(\mathbf{x}_k + \beta_k \mathbf{v}_k) \\ &= \frac{\|\mathbf{A}_{\text{Love}}(\mathbf{x}_k + \beta_k \mathbf{v}_k)\|^2}{L} \\ &= \frac{\|\mathbf{A}_{\text{Love}}\mathbf{v}_k\|^2 \beta_k^2 + 2\text{Re}\left[(\mathbf{A}_{\text{Love}}\mathbf{v}_k)^\dagger (\mathbf{A}_{\text{Love}}\mathbf{x}_k)\right] \beta_k + \|\mathbf{A}_{\text{Love}}\mathbf{x}_k\|^2}{L}.\end{aligned} \tag{4.48}$$

The LPC cost functional can also be expressed as a fourth order polynomial of β_k as [72]

$$\begin{aligned}\mathcal{F}_{\text{LPC}}(\beta_k) &= \mathcal{C}_{\text{LPC}}(\mathbf{x}_k + \beta_k \mathbf{v}_k) \\ &= \frac{\left\|(\mathbf{J}_{\text{R},k} + \beta_k \mathbf{v}_{1,k}) \odot (\mathbf{M}_{\text{R},k} + \beta_k \mathbf{v}_{3,k}) + (\mathbf{J}_{\text{I},k} + \beta_k \mathbf{v}_{2,k}) \odot (\mathbf{M}_{\text{I},k} + \beta_k \mathbf{v}_{4,k}) - \frac{2}{\alpha^2}\mathbf{p}^{\text{in}}\right\|_D^2}{N\left\|\frac{2}{\alpha^2}\mathbf{p}^{\text{in}}\right\|_D^2} \\ &= \frac{\left\|\mathbf{c}_k \beta_k^2 + \mathbf{d}_k \beta_k + \mathbf{r}_{\text{LPC},k}\right\|_D^2}{N\left\|\frac{2}{\alpha^2}\mathbf{p}^{\text{in}}\right\|_D^2} \\ &= a_{\text{LPC},4}\beta_k^4 + a_{\text{LPC},3}\beta_k^3 + a_{\text{LPC},2}\beta_k^2 + a_{\text{LPC},1}\beta_k + a_{\text{LPC},0},\end{aligned} \tag{4.49}$$

where

$$\begin{aligned}a_{\text{LPC},4} = \frac{\|\mathbf{c}_k\|_D^2}{N\left\|\frac{2}{\alpha^2}\mathbf{p}^{\text{in}}\right\|_D^2},\ a_{\text{LPC},3} = \frac{2\mathbf{c}_k^{\text{T}}\mathbf{d}_k}{N\left\|\frac{2}{\alpha^2}\mathbf{p}^{\text{in}}\right\|_D^2},\ a_{\text{LPC},2} = \frac{2\mathbf{c}_k^{\text{T}}\mathbf{r}_{\text{LPC},k} + \|\mathbf{d}_k\|_D^2}{N\left\|\frac{2}{\alpha^2}\mathbf{p}^{\text{in}}\right\|_D^2}, \\ a_{\text{LPC},1} = \frac{2\mathbf{d}_k^{\text{T}}\mathbf{r}_{\text{LPC},k}}{N\left\|\frac{2}{\alpha^2}\mathbf{p}^{\text{in}}\right\|_D^2},\ a_{\text{LPC},0} = \frac{\|\mathbf{r}_{\text{LPC},k}\|_D^2}{N\left\|\frac{2}{\alpha^2}\mathbf{p}^{\text{in}}\right\|_D^2}.\end{aligned} \tag{4.50}$$

In the expressions given in (4.49) and (4.50), $\mathbf{c}_k$ and $\mathbf{d}_k$ are two real-valued vectors at the kth iteration that can be calculated as

$$\mathbf{c}_k = \mathbf{v}_{1,k} \odot \mathbf{v}_{3,k} + \mathbf{v}_{2,k} \odot \mathbf{v}_{4,k},\ \mathbf{d}_k = \mathbf{J}_{\text{R},k} \odot \mathbf{v}_{3,k} + \mathbf{M}_{\text{R},k} \odot \mathbf{v}_{1,k} + \mathbf{J}_{\text{I},k} \odot \mathbf{v}_{4,k}, \tag{4.51}$$

where $\mathbf{v}_{1,k}$, $\mathbf{v}_{2,k}$, $\mathbf{v}_{3,k}$ and $\mathbf{v}_{4,k}$ are vectors in $\mathbb{R}^N$, and are the segments of the search direction

$\mathbf{v}_k$ such that (i.e., column-wise concatenation)

$$\mathbf{v}_k = \begin{bmatrix} \mathbf{v}_{1,k} \\ \mathbf{v}_{2,k} \\ \mathbf{v}_{3,k} \\ \mathbf{v}_{4,k} \end{bmatrix}. \tag{4.52}$$

The total variation cost functional in terms of β_k can be expressed as

$$\mathcal{F}_{\mathrm{TV}}(\beta_k) = \frac{\left(\|D_x(\mathbf{v}_k)\|_D^2 + \|D_z(\mathbf{v}_k)\|_D^2\right)\beta_k^2}{N} + \frac{2\left(D_x(\mathbf{x}_k)^{\mathrm{T}} D_x(\mathbf{v}_k) + D_z(\mathbf{x}_k)^{\mathrm{T}} D_z(\mathbf{v}_k)\right)\beta_k}{N} + \frac{\|D_x(\mathbf{x}_k)\|_D^2 + \|D_z(\mathbf{x}_k)\|_D^2}{N}, \tag{4.53}$$

where similar to (4.43), the operators D_x and D_z take the partial derivative of real and imaginary current density components, or the segments of the search direction separately, with respect to x and z. Notice that if 2D assumption ($\frac{\partial}{\partial z} = 0$) is made, the total variation cost functional in terms of β_k can be simplified as

$$\mathcal{F}_{\mathrm{TV}}(\beta_k) = \frac{\|D_x(\mathbf{v}_k)\|_D^2 \beta_k^2 + 2D_x(\mathbf{x}_k)^{\mathrm{T}} D_x(\mathbf{v}_k)\beta_k + \|D_x(\mathbf{x}_k)\|_D^2}{N}. \tag{4.54}$$

Finally, whether the field data is given with or without phase, the total cost functional is a fourth order polynomial in terms of β_k, and can be calculated as

$$\mathcal{F}(\beta_k) = \mathcal{F}_{\mathrm{data}}(\beta_k) + w_{\mathrm{Love}}\mathcal{F}_{\mathrm{Love}}(\beta_k) + w_{\mathrm{LPC}}\mathcal{F}_{\mathrm{LPC}}(\beta_k) + w_{\mathrm{TV}}\mathcal{F}_{\mathrm{TV}}(\beta_k). \tag{4.55}$$

The analytical step length can then be found by numerically solving the third degree polynomial, $\frac{\partial \mathcal{F}(\beta_k)}{\partial \beta_k} = 0$, and choosing the real-valued root that results in the smallest $\mathcal{F}(\beta_k)$.

Chapter 5

Full-Wave Simulation Results

In this chapter, several metasurface designs simulated in Ansys HFSS will be presented. The design procedure follows the previous chapter where the output tangential fields are acquired using the inversion algorithm, and the three-layer admittance sheet topology is used for each unit cell. In all the examples shown here, the admittance sheets are either purely capacitive or inductive. That is, no gain or loss mechanisms have been used. In addition, in all the examples, practical dielectric substrates, e.g., Rogers RO3010, have been used in the unit cell model, and the unit cell model shown in Figure 2.3 is used for the metasurface implementation in Ansys HFSS.

5.1 Performance Comparison between Fixed and Analytical Step Length

The main purpose of this section is to investigate the advantage of using the analytical step length derived in this thesis. Two examples are conducted within the 2D assumption ($\frac{\partial}{\partial z} = 0$). In these examples, the metasurface lies in the xz plane. Since the problem is 2D with no variations along the z axis, the metasurface will have spatial variations only along

the x axis, and is fully periodic along the z axis. Furtheremore, due to this 2D assumption, the desired power pattern contains only one far-field cut in the xy plane. Therefore, the angular variation of the desired power pattern cut can be represented by the azimuthal angle φ. (As will be seen, when we go to the 3D case, we also need the elevation angle θ to fully represent the angular variation of the power pattern.)

For the first example, two metasurfaces are designed to transform a transverse magnetic (TM)[1] incident plane wave to a desired far-field power pattern ($|H_z|$) as shown in red in Figure 5.1 at 10.5 GHz. The metasurfaces lie in the xz plane and they individually consist of 30 unit cells with the same width of $\frac{\lambda}{6}$ spread across the x axis. To calculate the susceptibility profiles of the two metasurfaces, the tangential output fields are found using the inversion algorithm via (i) a fixed step length ($\beta_k = 2 \times 10^3$)[2] and (ii) the analytical step length, respectively. The weighting parameters are $w_{\text{Love}} = 10^{-4}$, $w_{\text{LPC}} = 1$ and $w_{\text{TV}} = 5 \times 10^{-12}$ for both cases.

The inversion algorithm is then run with the fixed step length and with the analytical step length using the same initial guess and stopping condition. It takes 11883 iterations to converge using the fixed step length, and 543 iterations to converge using the analytical step length. Their convergence rates in the first 10000 iterations are shown in Figure 5.2. As expected, the inversion algorithm converges faster when the analytical step length is implemented. It should be emphasized that we have intentionally chosen an appropriate fixed step length. If we were to choose a non-appropriate one, the inversion algorithm using a fixed step length could have failed.

The resulting far-field power patterns from the inversion results are shown in black in Figure 5.1. After the equivalent current densities are determined, the susceptibility values,

[1] This is equivalent to the TE_z configuration.

[2] In this particular example, a step length of 2×10^3 is not the largest fixed step length that guarantees the algorithm to converge, but a fixed step length of 3×10^3 would cause convergence issue, and therefore, it is reasonable. The same reason applies to the choice of the fixed step length of the second example. Also, note that the step length in this case does not vary as a function of iteration k.

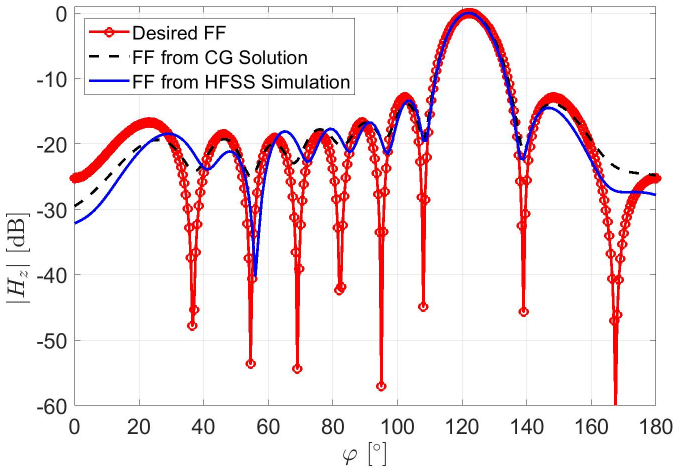

(a) Fixed Step Length

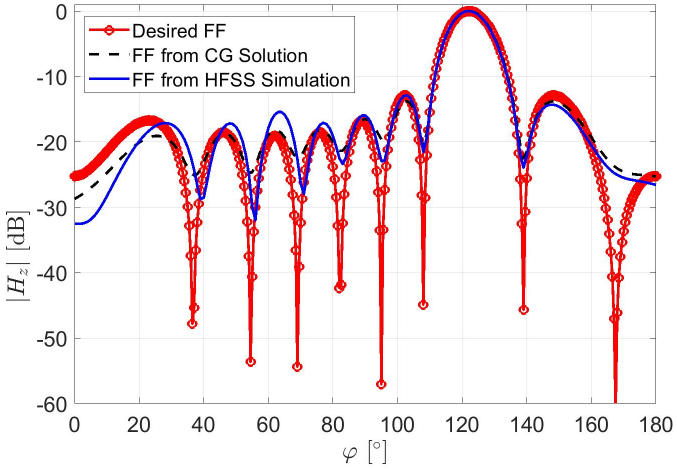

(b) Analytical Step Length

Fig. 5.1: Far-field comparison between the use of the fixed step length and analytical step length for the 2D TM test case. The desired far-field power pattern is shown in red, the power pattern from the inversion solution is shown in black, and the power pattern from the Ansys HFSS simulation is shown in blue.

and consequently, the three admittance values can be calculated, where Rogers RO3010 ($\varepsilon_r = 10.2, \tan\delta = 0.0022$) is used for the two dielectric substrates, and each with a thickness of 1.28 mm. As the metasurface is lossless and passive, the admittance values are purely imaginary, and the resulting susceptance values (i.e., the imaginary part of the admittance)

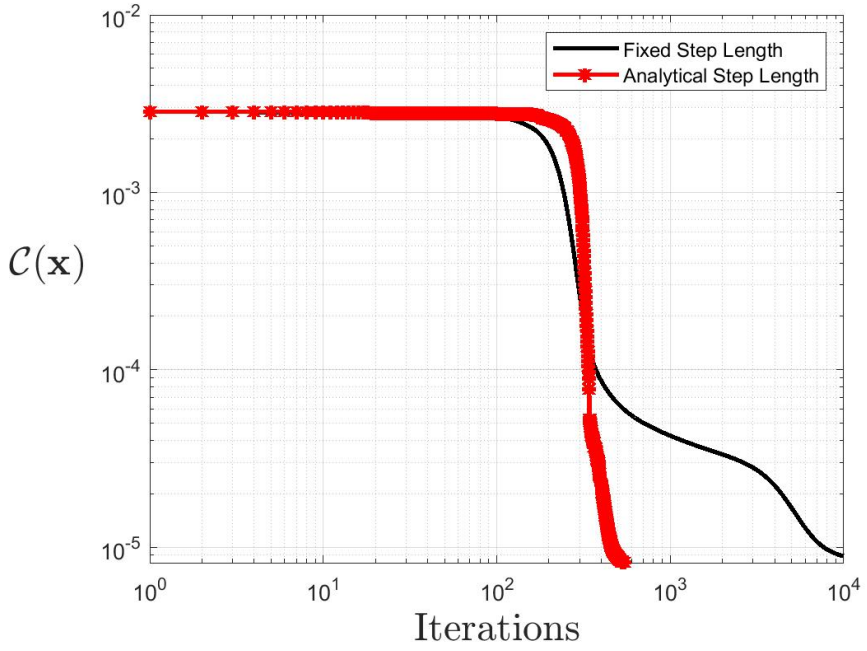

Fig. 5.2: The convergence rate using the fixed step length versus the analytical step length for the 2D TM test case.

for each unit cell are shown in Figure 5.3. The metasurface designs are then simulated in Ansys HFSS, and to improve the result, perfect electric baffles[3] [27] are placed in between the unit cells to create a closer agreement between the unit cell transmission-line based model and the full-wave behaviour. In addition, absorbing metasurfaces are placed next to the metasurface, extending each side by 2λ.

The absolute value of the real part of the total electric field ($|\mathrm{Re}(\boldsymbol{E})|$) in the simulation domain is shown in Figure 5.4. Note that this is the near-field distribution. In this near-field distribution, we can still identify the formation of the refracted beam. The resulting tangential fields on the output side of the metasurface are then extracted from Ansys HFSS. They can then be used in near-field to far-field transformation to obtain the resulting far-field power pattern.[4] The far-field power pattern from the Ansys HFSS simulation is shown

[3] In practice, these can be implemented using vias [27].

[4] This can be for example done by converting the output tangential fields to the equivalent currents, and

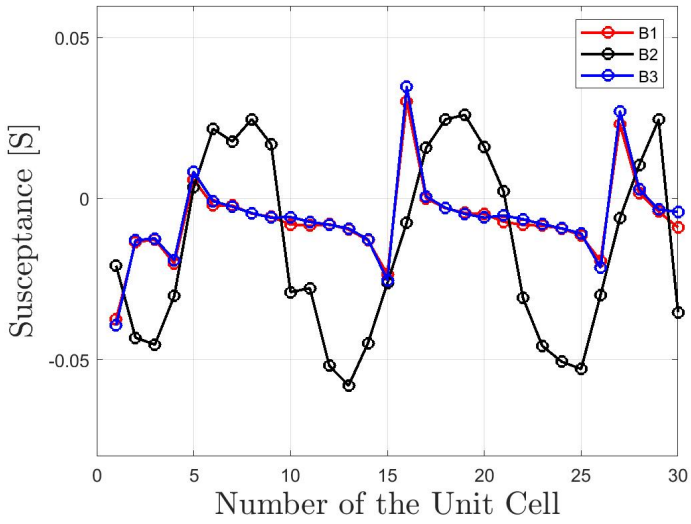

(a) Fixed Step Length

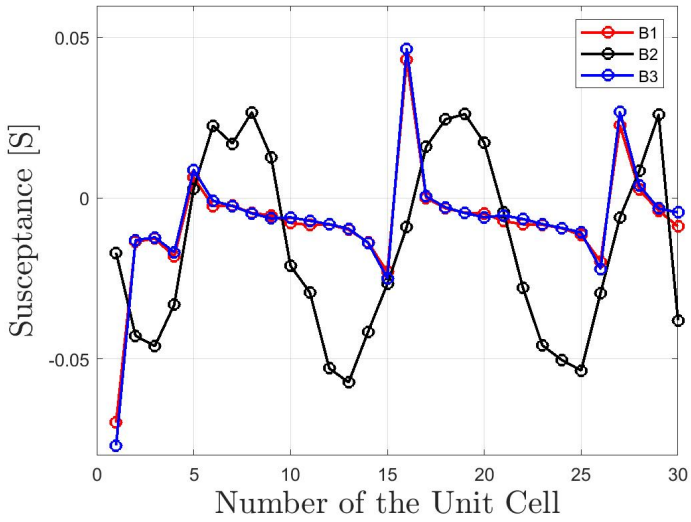

(b) Analytical Step Length

Fig. 5.3: The three susceptance values per unit cell resulting from using the fixed step length approach and the analytical step length approach for the 2D TM case.

in blue in Figure 5.1. As can be seen, the simulated power pattern matches well with the desired power pattern, with some minor deviation in the side lobes. The efficiencies,

then mapping them to the far-field zone using the forward operator.

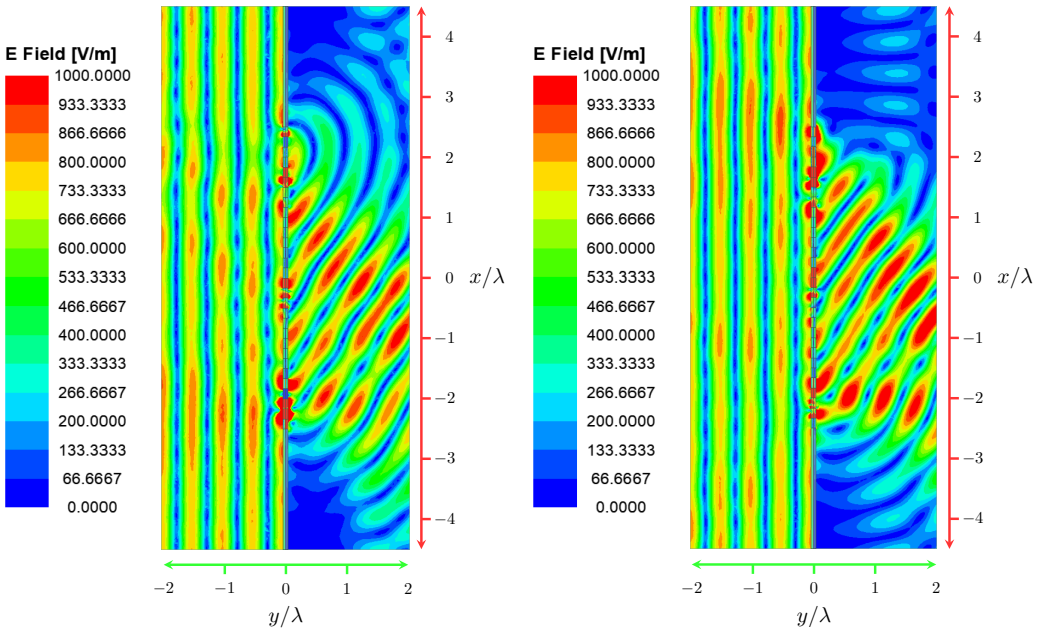

(a) Fixed step length **(b)** Analytical step length

Fig. 5.4: The absolute value of the real part of the electric field in the simulation domain (near-field zone) for the 2D TM test case. The metasurface lies in the xz plane with no variations along the z axis. In this 2D cut, the metasurface is located on the $y = 0$ line. From its left side, the metasurface is illuminated by a plane wave which is normally incident on the metasurface. The right side of the metasurface is its output side which shows the creation of a refracted beam. The metasurface design in (a) is based on the inversion solution using the fixed step length, and (b) is based on the inversion solution using the analytical step length. Note that in both cases, the quality of the impinging plane wave on the input side of the metasurface is quite good which is a testament to the fact that the metasurface is nearly reflectionless.

calculated as the ratio between the input power and the output power, are 94% for the fixed step length and 95% for the analytical step length. The reason that the transmission efficienct is not 100% is due to at least two reasons: the substrate RO3010 is slightly lossy, and also the LPC constraint is not perfectly satisfied.

The second example uses the same configuration for the metasurfaces with a transverse electric (TE)[5] incident plane wave, and a desired far-field power pattern ($|E_z|$) as shown in red in Figure 5.5 at 10.5 GHz. The inversion algorithm is again run twice with a fixed step length of 4×10^{-4} and the analytical step length. Both cases use the same initial guess,

[5]This is equivalent to the TM_z configuration as it is known in electromagnetic imaging.

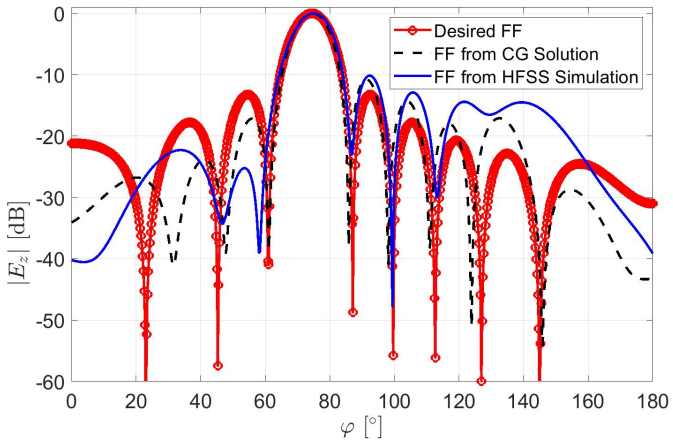

(a) Fixed Step Length

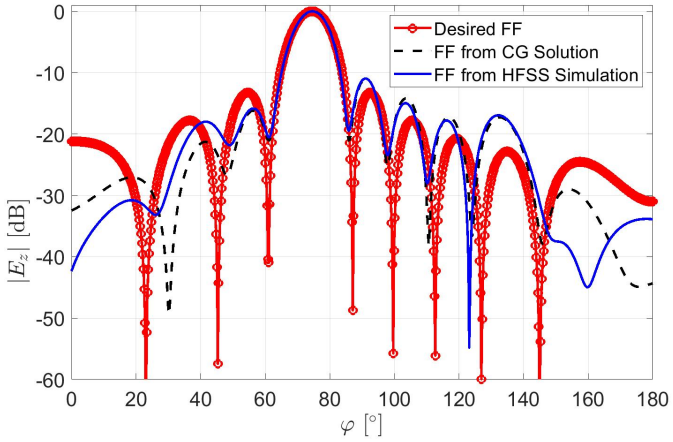

(b) Analytical Step Length

Fig. 5.5: Far-field comparison between the use of the fixed step length and analytical step length for the 2D TE test case. The desired far-field power pattern is shown in red, the power pattern from the inversion solution is shown in black, and the power pattern from the Ansys HFSS simulation is shown in blue.

stopping condition and weighting parameters, which are chosen as $w_{\text{Love}} = 10^{-5}$, $w_{\text{LPC}} = 1$ and $w_{\text{TV}} = 1 \times 10^{-4}$. It takes 219199 iterations to converge using the fixed step length, and only 207 iterations to converge using the analytical step length. Their convergence rates in the first 10000 iterations are shown in Figure 5.6. It is again shown that the use of analytical step length makes the inversion algorithm converge faster. Also, note that since the fixed

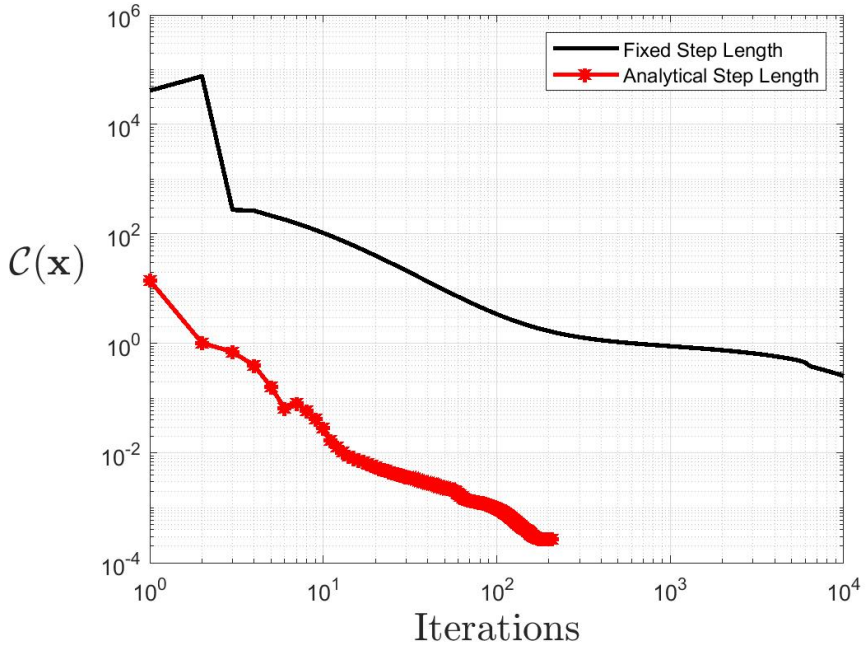

Fig. 5.6: The convergence rate using the fixed step length versus the analytical step length for the 2D TE test case.

step length is based on *ad hoc* choice, the cost functional is not guaranteed to decrease at each iteration. This is clearly visible in the first few iterations of the CG algorithm under the fixed step length.

The far-field pattern derived from the inversion results is shown in black in Figure 5.5. The two designs are then simulated in Ansys HFSS with the same setup of the previous example (using Rogers RO3010 substrates), except that the PEC baffles are now switched to perfect magnetic conductor (PMC) baffles to accommodate the change of polarization.[6] The resulting susceptance values for each unit cell are shown in Figure 5.7. The absolute value of the real part of the total magnetic field ($|\mathrm{Re}(\boldsymbol{H})|$) in the simulation domain is shown in Figure 5.8. Noticeable reflections can be observed from the case where the metasurface

[6] Although the implementation of the PEC baffles are practical using vias as was done in [27], it is not clear to the author how these PMC baffles can be implemented in practice.

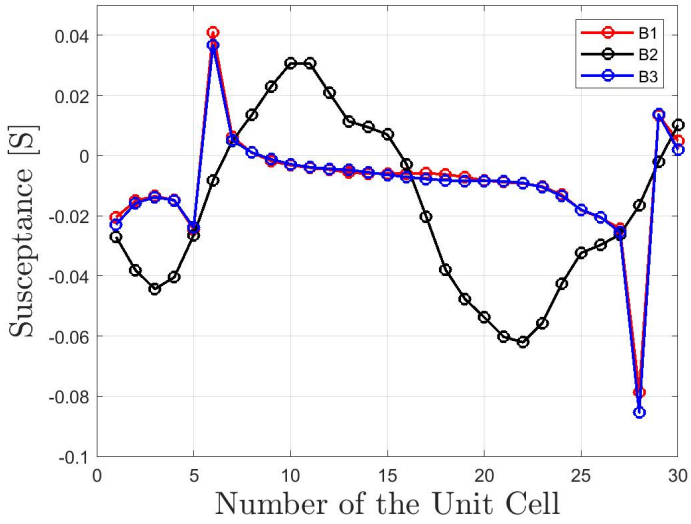

(a) Fixed Step Length

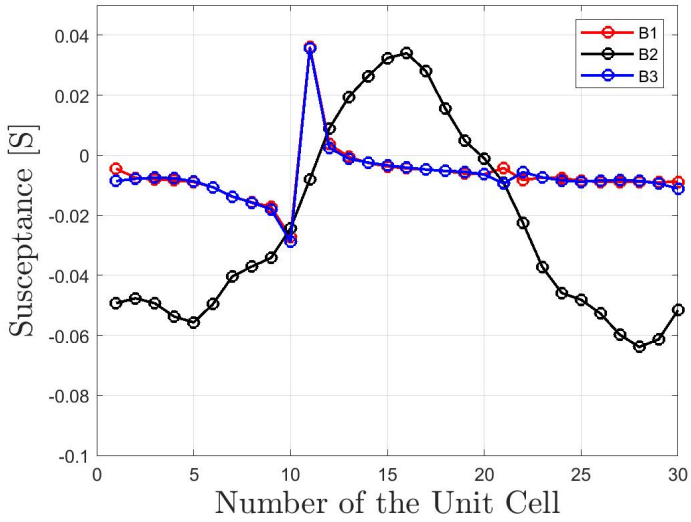

(b) Analytical Step Length

Fig. 5.7: The three susceptance values resulting from using the fixed step length and the analytical step length approaches for the 2D TE case.

is designed using the fixed step length.[7] This is because the resulting equivalent currents

[7]This can be understood by looking at the quality of the plane wave on the input (left) side of the metasurface. As can be seen, the quality of the plane wave in the case of analytical step length is better. For the case of fixed step length, we see reflections that tend to create a standing wave on the input side of the metasurface.

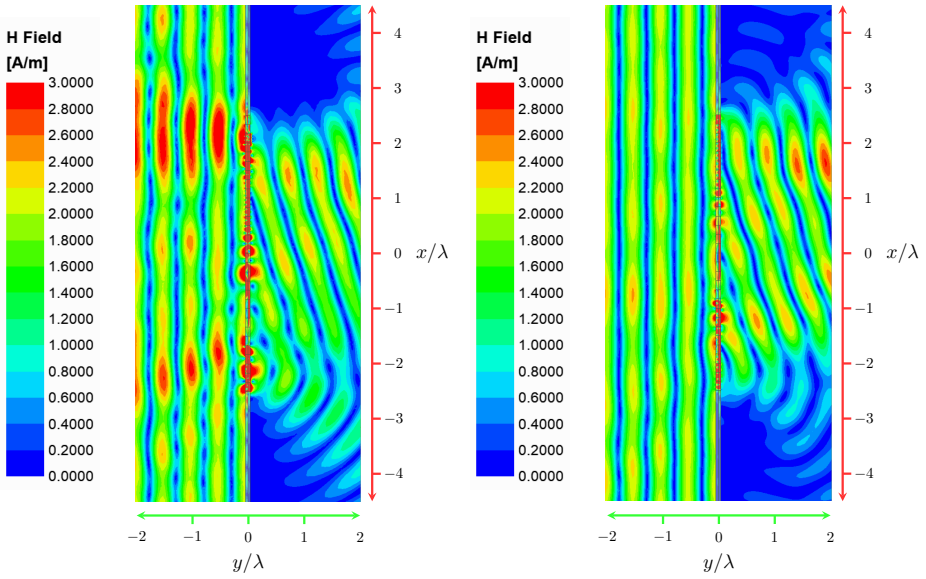

(a) Fixed step length **(b)** Analytical step length

Fig. 5.8: The absolute value of the real part of the magnetic field in the simulation domain (near-field zone) for the TE test case. The metasurface lies in the xz plane with no variations along the z axis. In this 2D cut, the metasurface is located on the $y = 0$ line. From its left side, the metasurface is illuminated by a plane wave which is normally incident on the metasurface. The right side of the metasurface is its output side which shows the creation of a refracted beam. The metasurface design in (a) is based on the inversion solution using the fixed step length, and (b) is based on the inversion solution using the analytical step length.

using the fixed step length have a rapider spatial change, and poorer enforcement of the Love's equivalent principle[8] than the ones using the analytical step length. The far-field power pattern from the Ansys HFSS simulation is shown in blue in Figure 5.5, and the case using the analytical step length shows a better alignment. The efficiencies are calculated as 80% for the fixed step length and 91% for the analytical step length which agrees with the observation of more reflections in the case of fixed step length.

[8]We have already shown that if Love's condition is not properly enforced, undesired reflections will arise [68].

5.2 3D Far-Field Power Pattern Synthesis

In the above, we have shown the improvements that can be achieved by the use of analytically-derived expressions for the step length in comparison with the prior works [28, 30, 32] using *ad hoc* fixed step lengths. These works have been done under the 2D TM or TE assumptions. In this section, we examine the inversion algorithm under the 3D case. As opposed to the 2D case, the metasurface under the 3D assumption can have spatial modulation in both directions along the metasurface, and the beam shaping can be done at different cuts in the far-field zone.

Herein, two 3D examples will be presented with their main difference being the incident field. The goal of the first example is to design a metasurface that transform the $\hat{z}$ polarized incident plane wave traveling towards $\hat{y}$ to a desired far-field power pattern ($|E_\theta|^2$) that is specified on two plane cuts as shown in red in Figure 5.9 at 10.5 GHz. The metasurface lies in the xz plane, and it consist of 30 unit cells along both $\hat{x}$ and $\hat{z}$ directions, resulting in a total of 900 unit cell. Each unit cell is $\frac{\lambda}{6}$ in width, making the metasurface a total area of $5\lambda \times 5\lambda$. The desired power pattern is given in xy plane and yz plane as $|\mathbf{f}_1|^2$ and $|\mathbf{f}_2|^2$. The total desired power pattern is then constructed by concatenating the two cuts as[9]

$$|\mathbf{f}|^2 = \begin{bmatrix} |\mathbf{f}_1|^2 \\ |\mathbf{f}_2|^2 \end{bmatrix}. \tag{5.1}$$

The above vector then serves as the data to the inversion algorithm.

The inversion algorithm is then used to find the equivalent currents and subsequently the susceptibility profile and the admittance values. The weighting parameter are $w_{\text{Love}} = 10^{-7}$, $w_{\text{LPC}} = 1$ and $w_{\text{TV}} = 10^{-7}$. Once the algorithm converges, the far-field power pattern generated by the equivalent currents is then found as shown in black in Figure 5.9. Rogers RO3010 of 1.28 mm thickness is used as the two substrates of the metasurface, and the

[9]The desired pattern is constructed using a dipole array.

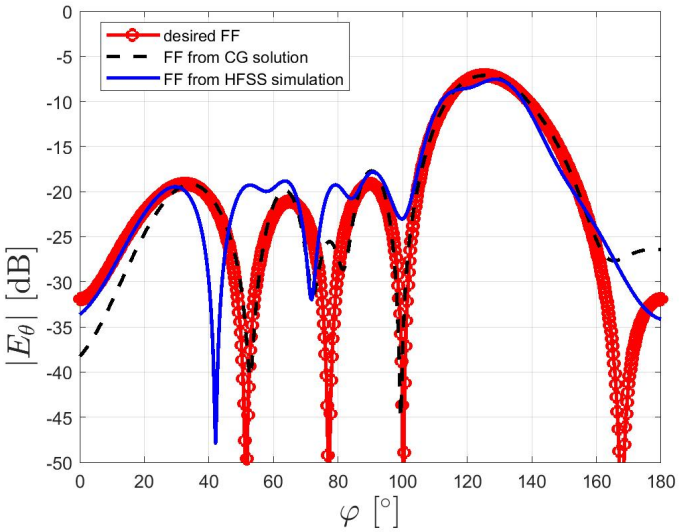

(a) xy plane

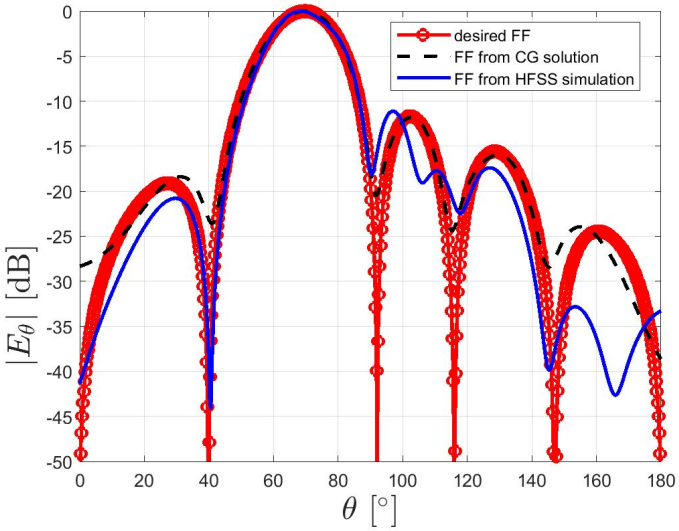

(b) yz plane

Fig. 5.9: 3D Test case with far-field power patterns in two perpendicular cuts. The metasurface aperture lies in the xz plane with the y axis being perperndicular to the metasurface aperture. Far-field power pattern with plane wave incident field in (a) xy plane and (b) yz plane. Desired power pattern is shown in red, power pattern obtained directly from reconstructed equivalent currents is shown in black, and power pattern from Ansys HFSS simulation is shown in blue.

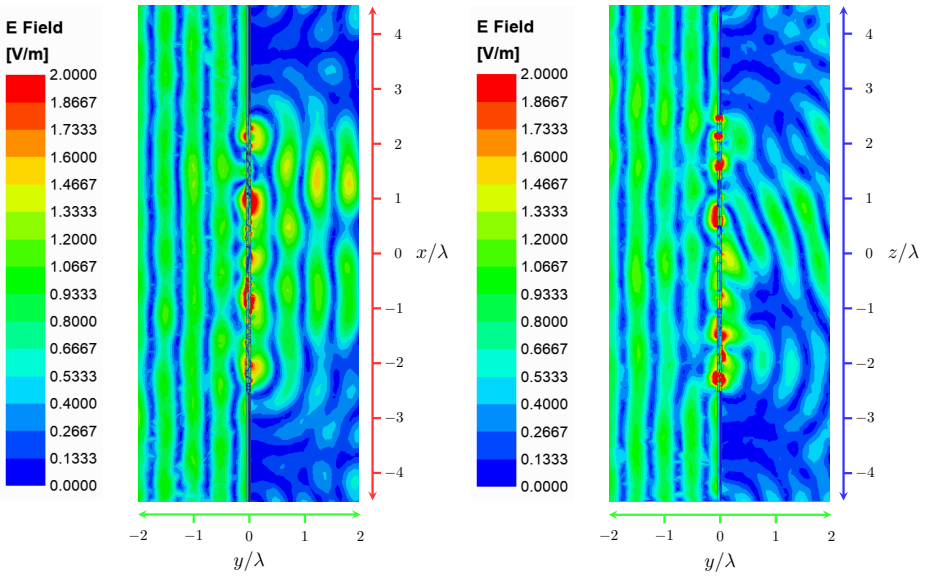

(a) xy plane **(b)** yz plane

Fig. 5.10: 3D test case with the plane wave incident on the metasurface from its left side. The absolute value of the real part of the electric field with plane wave incident field in the simulation domain on (a) xy plane and (b) yz plane.

design is then simulated in Ansys HFSS. PEC baffles are placed in between each row of the metasurface to improve the results. In addition, absorbing metasurfaces are placed around the metasurface, extending each side by 2λ, to prevent the spillover that could potentially affect the tangential output field. Two cuts of the absolute value of the real part of the total electric field in the simulation domain are shown in Figure 5.10.

Following the step described in the previous section, the far-field power pattern from the simulation result can be produced as shown in blue in Figure 5.9. This figure shows a good match between the desired far field pattern and the far-field pattern from the simulation in both cuts. The efficiency of the metasurface is calculated as 76%. One reason for this relatively low transmission efficiency is the reflections on the input side of the metasurface that can be seen in Figure 5.10(b). This is likely due to the fact that the LPC constraint is not satisfied well.

In the second 3D example, a horn antenna is used to generate the incident field. The horn

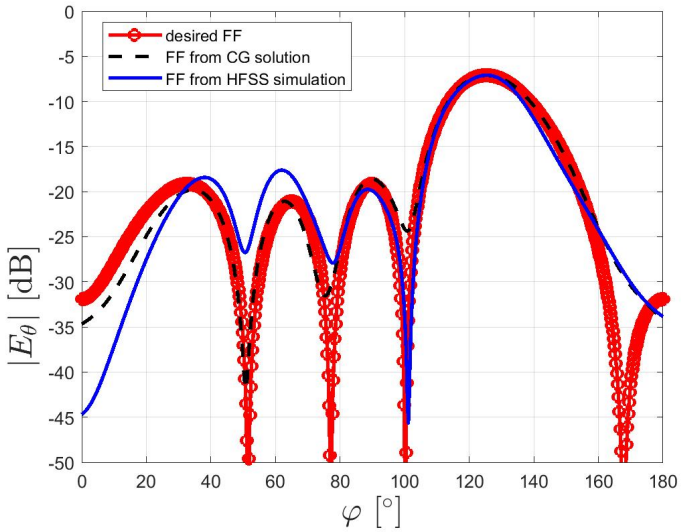

(a) xy plane

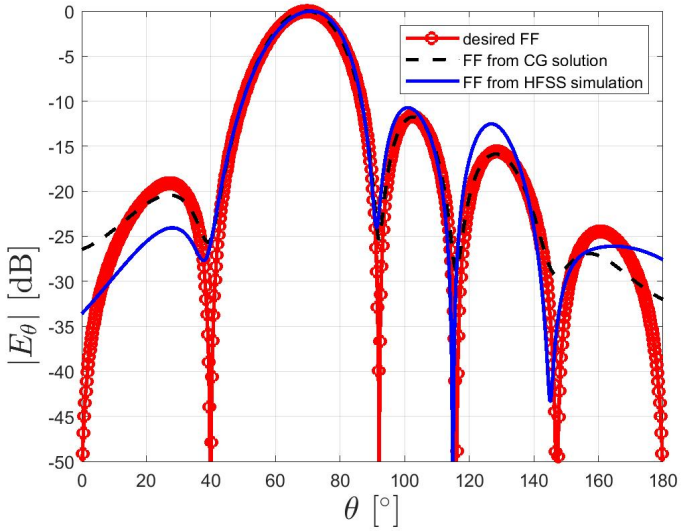

(b) yz plane

Fig. 5.11: 3D far-field power pattern synthesis with the horn antenna as the source in (a) xy plane and (b) yz plane. Desired power pattern is shown in red, power pattern obtained directly from reconstructed equivalent currents is shown in black, and power pattern from Ansys HFSS simulation is shown in blue.

antenna is fed with TE_{10} mode and the co-polarized component of the electric field of the horn antenna is along $\hat{z}$. It is placed 3λ away from the metasurface, with its boresight

towards $\hat{y}$. The goal of this example is to transform this incident field to a far-field power pattern that is the same as the previous example as shown in red in Figure 5.11.

With the set up of the metasurface unchanged, the inversion algorithm is preformed with the weighting parameters chosen as $w_{\text{Love}} = 10^{-5}$, $w_{\text{LPC}} = 1$ and $w_{\text{TV}} = 10^{-9}$. The far-field power pattern generated by the resulting equivalent currents is found as shown in black in Figure 5.11. After calculating the susceptibility profile, the metasurface design is simulated in Ansys HFSS with the PEC baffles placed in between each row. The resulting two cuts of the absolute value of the real part of the total electric field in the near field region are shown in Figure 5.10, and the far-field power pattern from the simulation result is produced as shown in blue in Figure 5.9. A good match between the desired far-field and the simulation result can be observed, with the transmission efficiency calculated as 80%.

We now investigate if our inverse formulation supports the existence of surface waves.[10] Surface waves travel along the metasurface (xz plane) and they are evanescent toward the $\hat{y}$ direction based on the coordinates chosen in this section. In the metasurface literature, surface waves have been utilized to help with satisfying the LPC constraint as surface waves can travel along the metasurface and help with power redistribution [73]. For example, in [74, 75], surface waves have been utilized to redistribute the power such that the power profile of a line source, which has a taper, can be locally matched with that of a plane wave, which is uniform. Similarly, in [76], surface waves are added to the solution in a separate optimization stage.

Herein, to check if our solution contains such surface waves, we perform the following. After finding the required tangential fields on the output metasurface side, we find its plane wave spectrum. As it is well-known, the plane wave spectrum consists of two parts: the propagating part and the evanescent part. The evanescent part exponentially decays as a

[10]The author acknowledges the contribution of Mario Phaneuf in the discussion on surface waves. Mario Phaneuf has developed the methodology to investigate the presence of surface waves in this inverse source framework.

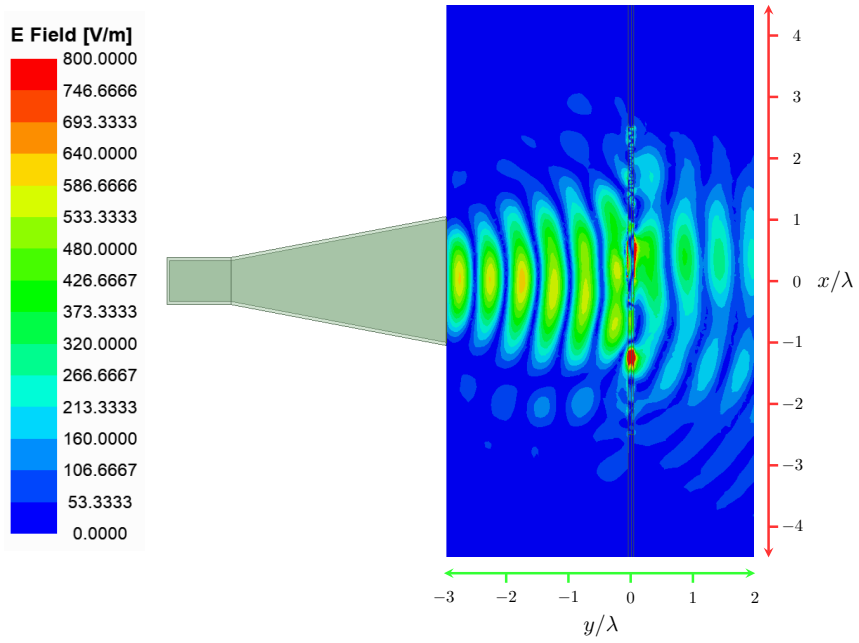

(a) xy plane

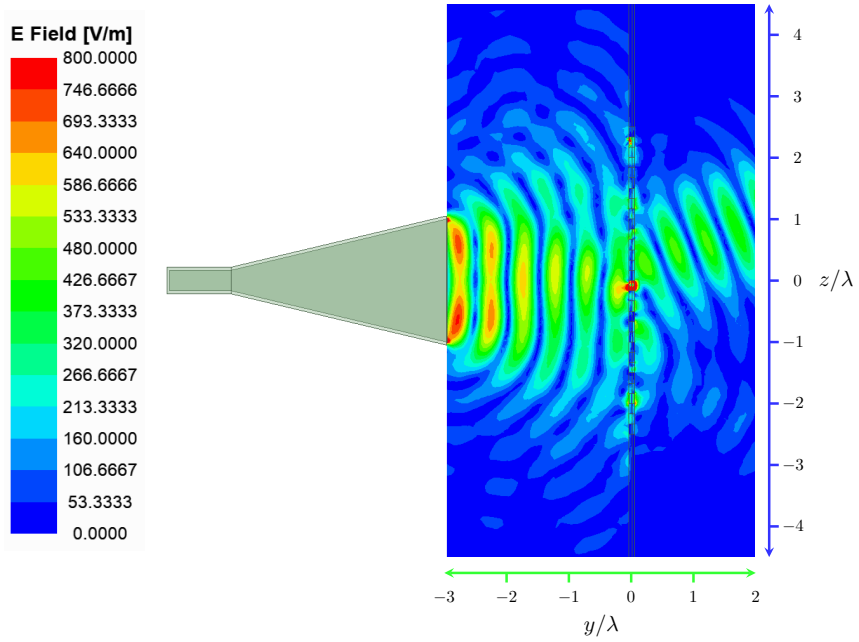

(b) yz plane

Fig. 5.12: The absolute value of the real part of the electric field with horn antenna as the source in the simulation domain on (a) xy plane and (b) yz plane.

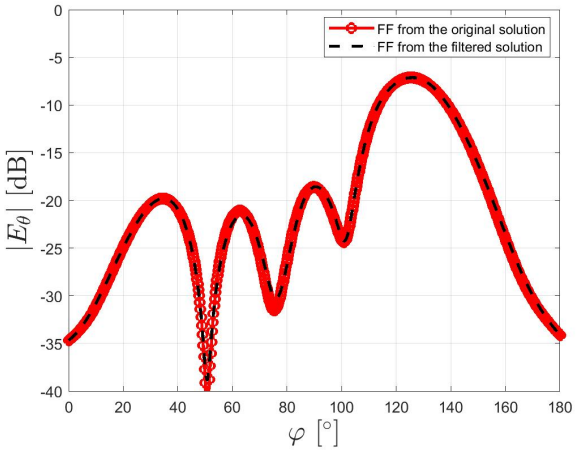

(a) xy plane

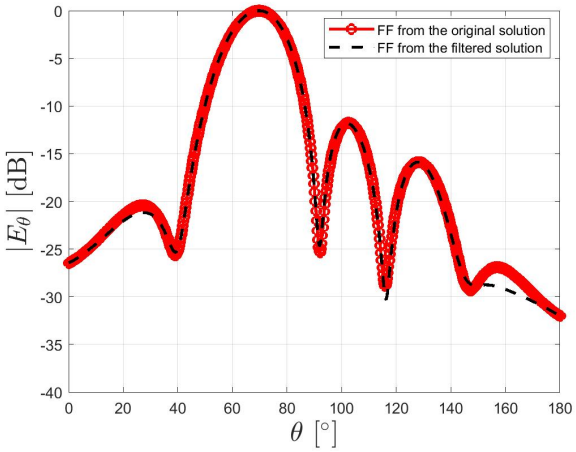

(b) yz plane

Fig. 5.13: 3D far-field power pattern derived from the equivalent currents in (a) xy plane and (b) yz plane. Power pattern derived from the original solution is shown in red, and the power pattern obtained from the filtered solution (without the evanescent spectrum) is shown in black.

function of y and therefore has no signature in the far-field zone. However, it is still present in the aperture of the metasurface and can potentially help with power redistribution to help satisfy the LPC constraint. If our inverse solution is benefiting from these surface waves, if we filter out the evanescent spectrum from the metasurface aperture tangential fields, the far-field pattern should not change but the LPC constraint on the metasurface

should be adversely affected.

After calculating the plane wave spectrum of the metasurface aperture tangential fields, we can remove its evanescent component. After removing the evanescent spectrum, we can propagate the filtered solution to the far-field zone to check if it still satisfies the far-field power pattern. This has been shown in Figure 5.13.

As can be seen, the far-field pattern of the original solution matches almost perfectly with the filtered solution. The reason behind small discrepancies lies in the fact that the far-field distance cannot be set to infinity to make the effect of evanescent waves exactly zero.

We now need to investigate whether or not the removal of the evanescent component has affected the power distribution on the metasurface. To this end, we calculate the normal real power density on the metasurface output side (aperture) for these two cases: the original solution and the filtered solution. Since the normal power density is along the y direction, we denote it as S^y, and then calculate the following:

$$\text{Power Difference } (\%) = 100 \times \frac{S^y_{\text{original}} - S^y_{\text{filtered}}}{S^y_{\text{original}}}, \tag{5.2}$$

at each unit cell location. The result of this calculation has been plotted in Figure 5.14. As can be seen, if we filter the evanescent component of the aperture field, the power distribution profile on the metasurface aperture significantly changes with respect to the original solution. Given that the original solution has a reasonable LPC match, we can conclude that the presence of the surface wave (evanescent component with respect to y direction) has helped us satisfy the LPC constraint.

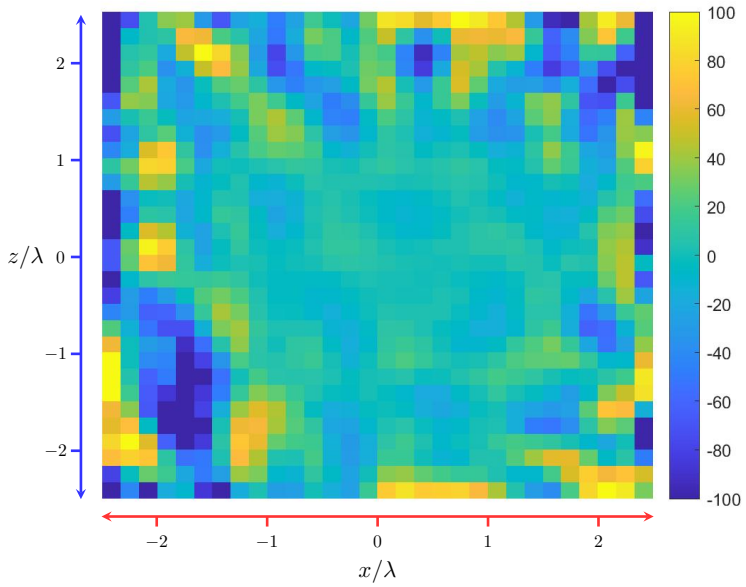

Fig. 5.14: The percentage difference of the normal power density between the original solution and filtered solution.

5.3 Cascaded Metasurface Design

As emphasized in the previous section, the LPC constraint must be well satisfied for a lossless and passive design. The approach that was discussed in the previous section to help with meeting the LPC constraint is to take advantage of surface waves. Another approach to help with the LPC constraint is to use a second metasurface. The combination of the two metasurfaces can help redistribute the power and can help with satisfying the LPC. The resulting metasurface pair is then referred to as a cascaded metasurface system [31,33,77,78]. The cascaded metasurface system does that through multiple reflections formed in the cavity between the two metasurfaces. These multiple reflections can then redistribute the power between the unit cells.

For pattern synthesis using a cascaded metasurface system, we still need to know the tangential fields on the output of the second metasurface. In [31, 32], this has been done using electromagnetic inversion. However, in these works, the design of cascaded metasurface

systems has been limited to the case in which there are no reflections in the cavity formed between the two metasurfaces. This increases the size of the cascaded metasurface system (i.e., the separation between the two metasurfaces). Herein, we use electromagnetic inversion to find the tangential fields on the second metasurface and then design a cascaded metasurface system that utilizes the multiple reflections between the two metasurfaces to reduce the overall size of the system. This is based on [33] and in particular using the implementation presented in [79].[11]

The cascaded metasurface system is designed to transform the incident field generated by a $\hat{z}$ polarized infinite line source with 2D assumption ($\frac{\partial}{\partial z} = 0$) to a desired far-field power pattern ($|E_z|$) as shown in red in Figure 5.15 at 10 GHz. The two metasurfaces lie in the xz plane, with a separation of 0.5λ. Each metasurface consists of 61 unit cells with the same width, and the resulting total width is 6λ. The line source is placed $\frac{\lambda}{3}$ away from the center of the first metasurface. For comparison purposes, a single metasurface is designed using the same set up as the cascaded metasurface system excluding the second metasurface. The inversion algorithm is then run twice, with the weighting parameters chosen as $w_{\text{Love}} = 10^{-3}$, $w_{\text{LPC}} = 1$ and $w_{\text{TV}} = 1 \times 10^{-7}$ for the single metasurface, and $w_{\text{Love}} = 10^{-4}$, $w_{\text{LPC}} = 0$ (LPC is satisfied by redistributing the incident power) and $w_{\text{TV}} = 1 \times 10^{-7}$ for the cascaded system. The far-field power pattern derived from the resulting equivalent currents are shown in black in Figure 5.15. The two designs are then simulated using Ansys HFSS, using Rogers RO3010 as substrates and the thickness of each substrate is 0.13 mm. The absolute value of the real part of the total electric field in the simulation domain is shown in Figure 5.16. Notice that no PEC baffle is used for both cases, which makes the design more practical. The far-field power pattern from the simulation result is shown blue in Figure 5.15. As can be seen in this figure, the far-field pattern from the simulation using the cascaded system

[11] The electromagnetic inversion has been performed by the author of this thesis and the design of the cascaded metasurface system employing multiple reflections has been done by Mr. Jayesh Gohel who is currently an MSc student in our group.

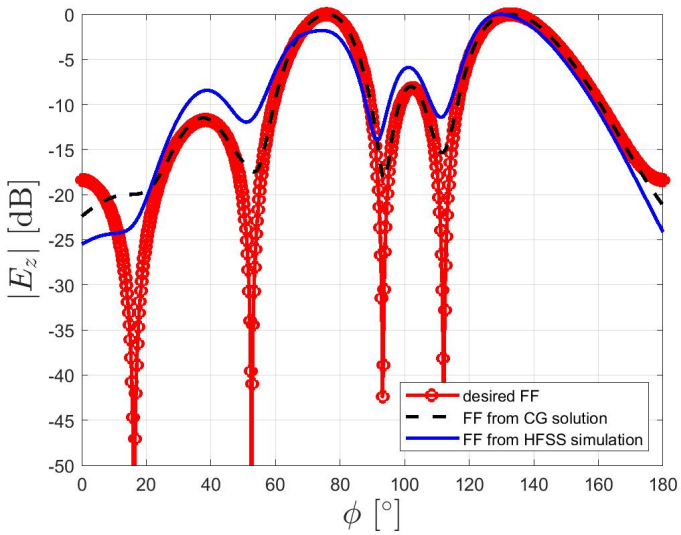

(a) Single metasurface

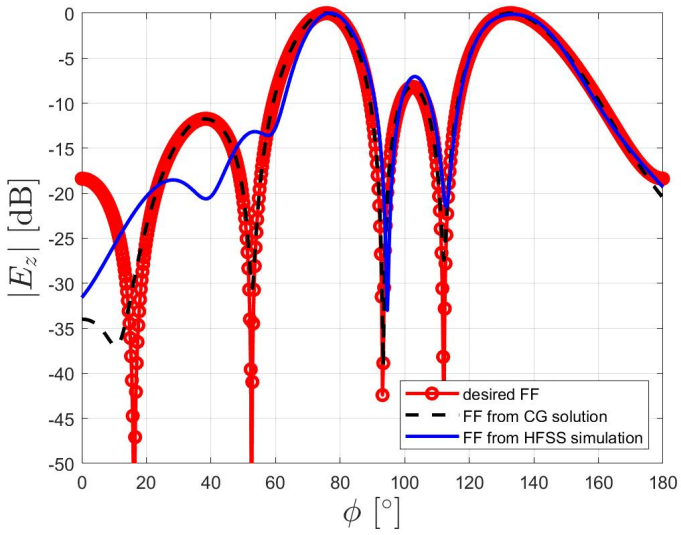

(b) Cascaded metasurface

Fig. 5.15: Far-field comparison between the use of a single metasurface and a cascaded metasurface system. The desired far-field power pattern is shown in red, the power pattern from the inversion solution is shown in black, and the power pattern from the Ansys HFSS simulation is shown in blue.

has a better match for the two main beams. This is because the equivalent currents for the cascaded system are spatially smoother and enforce Love's equivalent principle better, since

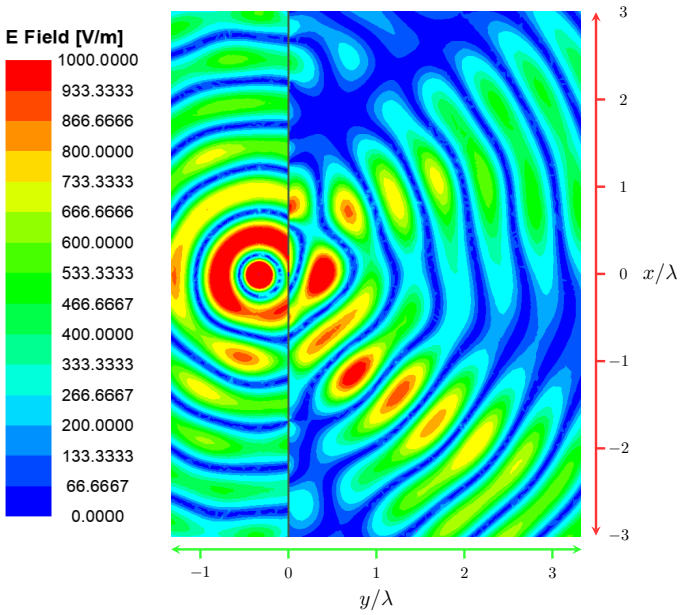

(a) Single metasurface

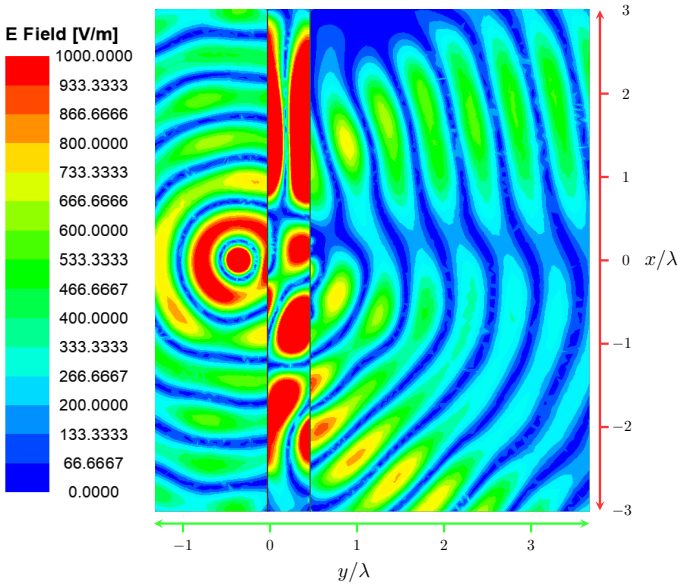

(b) Cascaded metasurface

Fig. 5.16: The absolute value of the real part of the electric field in the simulation domain using (a) a single metasurface and (b) cascaded metasurface system where the sepration between the two metasurfaces is 0.5λ.

no LPC is required during the inversion process in the cascaded metasurface design. This is due to the fact that the LPC in the cascaded metasurface design is satisfied via multiple reflections between the two metasurfaces, and thus the inversion algorithm does not need to enforce the LPC constraint $\mathcal{C}_{\text{LPC}}$ in (4.31). The calculated efficiencies are similar for the two cases, which are 96% for the single metasurface, and 94% for the cascaded system.

Chapter 6

Conclusions and Future Work

This chapter provide the overall conclusions of the thesis, along with some potential improvements that could be done in the future work.

6.1 Conclusions

Electromagnetic metasurfaces are capable of systematically transforming electromagnetic waves that impinge on them. Therefore, they can be used as a systematic means for beam shaping. Designing a metasurface to preform the desired transformation requires (1) obtaining the surface properties of the metasurface and (2) implementing unit cells that support those surface properties. These two step are often referred to as the macroscopic and the microscopic design steps respectively.

For the macroscopic design, the knowledge of the tangential fields on the both side of the metasurface are required. In this thesis, an inversion framework is presented as an approach to acquire the output tangential fields when they are not directly available. This is needed as the desired specifications are typically available in terms of, for example, far-field power patterns or performance criteria such as side lobe levels. The design problem can then be formulated as an inverse source problem where the inversion algorithm aims to

find the equivalent currents on the metasurface that produces the desired specifications. This optimization can be done by augmenting the cost functional to incorporate the Love's equivalence principle and the local power conservation constraint to support the design of lossless and passive metasurfaces. To this end, a total cost functional is constructed to quantify (1) the difference between the desired fields and the fields produced by the equivalent currents at the region of interest (the far-field zone in our case), (2) the fields produced by the equivalent where the null fields are required according to the Love's equivalence principle, (3) the difference between the input power and the output power for each unit cell, and (4) the spatial variation of the equivalent currents. This cost functional is then minimized using the nonlinear conjugate gradient method to find the equivalent currents that satisfy the assumptions and requirements for the metasurface. To validate the design, the three-layer impedance sheet topology for omega bianisotropic Huygens' metasurfaces is utilized to simulate the metasurface in a full-wave solver, which is Ansys HFSS in our case. It should be emphasized that the above formulation is a contribution presented by other authors [28, 30–32], which is utilized in this thesis and was presented for the sake of completeness.

In particular, the novelty of this thesis focuses on extending and improving the previous inversion approach for metasurface design [28,30–32]. The major improvement includes the derivation and implementation of the analytical step length. In the original work presented in [28, 30–32], trial and error for selecting a fixed step length is required, since a large step length might cause the algorithm to diverge, and a small step length results in slow convergence rate. The use of the analytical step length spare the trial and error stage, while the performance of the designed metasurface is not compromised according to the example. Moreover, the 2D assumption used in the previous works [28, 30–32] is now relieved and a 3D implementation of the inverse source approach is presented to handle desired patterns on two perpendicular cuts. In particular, the 3D implementation has been tested against a

practical incident field emanating from the horn antenna. It should be emphasized that the desired specifications considered in our implementation are in the form of power patterns as opposed to complex (magnitude and phase) field patterns. Due to the phaseless nature of power patterns, the associated inverse source problem will become nonlinear as opposed to a linear one when the desired complex field pattern is available. (Other forms of 3D inverse metasurface design for *complex* field pattern synthesis can be found for example in [80,81].) Finally, through the author's collaboration with two other team members, within the framework of our inversion algorithm, we have discussed the presence of surface waves in the utilized formulation that can be used for power redistribution along the metasurface as well as the use of two metasurfaces (i.e., cascaded metasurface systems) to help with power redistribution. These approaches can provide an extra means to satisfy the LPC constraint needed for the design of passive and lossless metasurfaces.

6.2 Future Work

There are several research directions that worth investigating based on the work presented in this thesis. First of all, although with the derivation of the analytical step length, the CG optimization algorithm is fully automated, the weightings of the LPC, TV and Love's cost functional are still need to be set by the user. Future work should investigate approaches to automate the choice of these weighting parameters. Currently, the weighting parameters are chosen in an *ad hoc* manner. If these values can self-adjust, then the whole inversion process is fully automated regardless of the problem. A promising approach is to dynamically change w_{Love}, w_{LPC} and w_{TV} as functions of the cost functionals, so that the resulting equivalent currents could fulfill the four aforementioned requirements and assumptions for all situations. (This will be similar to the concept of adaptive regularization described in [82] for the inverse scattering problem associated with electromagnetic imaging.)
Moreover, the validation stage right now uses the three layer admittance sheet topology

which is an ideal model. Although this could be physically implemented using the dogbone structure, the mutual coupling between the three layers could prevent the fabricated unit cell to have the same performance as the impedance model. One can develop an efficient and accurate transformation from the ideal admittance model to the physical dogbone structure, and eventually fabricate the metasurface based on the inversion frame work, and compare the measurements with the specifications. One approach to go from the impedance model to copper trace design (e.g., dogbone geometry design) is to use machine learning approaches as explained in [52]. In addition, the current design methodology addresses narrow-band scenarios. Both the macroscopic and microscopic design aspects need to be investigated for wideband applications if this is to be useful for wireless communications.

Bibliography

[1] V. G. Veselago, "The electrodynamics of substances with simultaneously negative values of ϵ and μ," *Soviet Physics Uspekhi*, vol. 10, no. 4, pp. 509–514, 1968.

[2] J. B. Pendry, A. J. Holden, W. J. Stewart, and I. Youngs, "Extremely low frequency plasmons in metallic mesostructures," *Phys. Rev. Lett.*, vol. 76, pp. 4773–4776, Jun 1996.

[3] J. Pendry, A. Holden, D. Robbins, and W. Stewart, "Magnetism from conductors and enhanced nonlinear phenomena," *IEEE Transactions on Microwave Theory and Techniques*, vol. 47, no. 11, pp. 2075–2084, 1999.

[4] R. Shelby, D. Smith, and S. Schultz, "Experimental verification of a negative index of refraction," *Science (American Association for the Advancement of Science)*, vol. 292, no. 5514, pp. 77–79, 2001.

[5] M. Albooyeh, "Electromagnetic characterization of metasurfaces," Ph.D. dissertation, Aalto University, Finland, 2015.

[6] C. L. Holloway, E. F. Kuester, J. A. Gordon, J. O'Hara, J. Booth, and D. R. Smith, "An overview of the theory and applications of metasurfaces: The two-dimensional equivalents of metamaterials," *IEEE Antennas and Propagation Magazine*, vol. 54, no. 2, pp. 10–35, 2012.

[7] N. Yu, P. Genevet, M. A. Kats, F. Aieta, J.-P. Tetienne, F. Capasso, and Z. Gaburro, "Light propagation with phase discontinuities: Generalized laws of reflection and refraction," *Science*, vol. 334, no. 6054, pp. 333–337, 2011. [Online]. Available: https://www.science.org/doi/abs/10.1126/science.1210713

[8] A. M. H. Wong and G. V. Eleftheriades, "Perfect anomalous reflection with a bipartite huygens' metasurface," *Phys. Rev. X*, vol. 8, p. 011036, Feb 2018. [Online]. Available: https://link.aps.org/doi/10.1103/PhysRevX.8.011036

[9] C. Pfeiffer and A. Grbic, "Metamaterial Huygens' surfaces," in *2013 IEEE MTT-S International Microwave Symposium Digest (MTT)*, 2013, pp. 1–4.

[10] Z. Liu, N. Bayat, and P. Mojabi, "On the use of absorbing metasurfaces in microwave imaging," *IEEE Transactions on Antennas and Propagation*, vol. 69, no. 12, pp. 9026–9031, 2021.

[11] C. Pfeiffer, N. K. Emani, A. M. Shaltout, A. Boltasseva, V. M. Shalaev, and A. Grbic, "Efficient light bending with isotropic metamaterial huygens surfaces," *Nano letters*, vol. 14, no. 5, pp. 2491–2497, 2014.

[12] C. Pfeiffer and A. Grbic, "Metamaterial Huygens surfaces: tailoring wave fronts with reflectionless sheets," *Physical review letters*, vol. 110, no. 19, p. 197401, 2013.

[13] V. G. Ataloglou, M. Chen, M. Kim, and G. V. Eleftheriades, "Microwave huygens metasurfaces: Fundamentals and applications," *IEEE Journal of Microwaves*, vol. 1, no. 1, pp. 374–388, 2021.

[14] M. Chen, "Design and applications of printed-circuit-board Huygens' metasurfaces," Ph.D. dissertation, University of Toronto, Canada, 2021.

[15] L. Martinez-Lopez, J. Rodriguez-Cuevas, J. I. Martinez-Lopez, and A. E. Martynyuk, "A multilayer circular polarizer based on bisected split-ring frequency selective surfaces," *IEEE Antennas and Wireless Propagation Letters*, vol. 13, pp. 153–156, 2014.

[16] A. Li, Z. Luo, H. Wakatsuchi, S. Kim, and D. F. Sievenpiper, "Nonlinear, active, and tunable metasurfaces for advanced electromagnetics applications," *IEEE Access*, vol. 5, pp. 27 439–27 452, 2017.

[17] N. Chamanara, Y. Vahabzadeh, and C. Caloz, "Simultaneous control of the spatial and temporal spectra of light with space-time varying metasurfaces," *IEEE Transactions on Antennas and Propagation*, vol. 67, no. 4, pp. 2430–2441, 2019.

[18] E. F. Kuester, M. A. Mohamed, M. Piket-May, and C. L. Holloway, "Averaged transition conditions for electromagnetic fields at a metafilm," *IEEE Transactions on Antennas and Propagation*, vol. 51, no. 10, pp. 2641–2651, 2003.

[19] M. M. Idemen, *Discontinuities in the electromagnetic field*. John Wiley & Sons, 2011, vol. 40.

[20] F. S. Cuesta, I. A. Faniayeu, V. S. Asadchy, and S. A. Tretyakov, "Planar broadband huygens metasurfaces for wave manipulations," *IEEE Transactions on Antennas and Propagation*, vol. 66, no. 12, pp. 7117–7127, 2018.

[21] K. Achouri, M. A. Salem, and C. Caloz, "General metasurface synthesis based on susceptibility tensors," *IEEE Transactions on Antennas and Propagation*, vol. 63, no. 7, pp. 2977–2991, 2015.

[22] K. Achouri, "Synthesis and applications of electromagnetic metasurfaces," Ph.D. dissertation, École Polytechnique de Montréal, Canada, 2017.

[23] Z. Liu, *On the use of absorbing and matching metasurfaces for microwave imaging*, Master's thesis, University of Manitoba, Manitoba, Canada, 2021 [available online].

[24] Y. Ra'di, V. S. Asadchy, and S. A. Tretyakov, "Tailoring reflections from thin composite metamirrors," *IEEE Transactions on Antennas and Propagation*, vol. 62, no. 7, pp. 3749–3760, 2014.

[25] C. Caloz and A. Sihvola, "Electromagnetic chirality, part 1: The microscopic perspective [electromagnetic perspectives]," *IEEE Antennas and Propagation Magazine*, vol. 62, no. 1, pp. 58–71, 2020.

[26] A. H. Dorrah, M. Chen, and G. V. Eleftheriades, "Bianisotropic huygens metasurface for wideband impedance matching between two dielectric media," *IEEE Transactions on Antennas and Propagation*, vol. 66, no. 9, pp. 4729–4742, 2018.

[27] G. Xu, S. V. Hum, and G. V. Eleftheriades, "Augmented huygens metasurfaces employing baffles for precise control of wave transformations," *IEEE Transactions on Antennas and Propagation*, vol. 67, no. 11, pp. 6935–6946, 2019.

[28] T. Brown, C. Narendra, Y. Vahabzadeh, C. Caloz, and P. Mojabi, "On the use of electromagnetic inversion for metasurface design," *IEEE Transactions on Antennas and Propagation*, vol. 68, no. 3, pp. 1812–1824, 2020.

[29] A. Epstein and G. V. Eleftheriades, "Arbitrary power-conserving field transformations with passive lossless omega-type bianisotropic metasurfaces," *IEEE Transactions on Antennas and Propagation*, vol. 64, no. 9, pp. 3880–3895, 2016.

[30] T. Brown, Y. Vahabzadeh, C. Caloz, and P. Mojabi, "Electromagnetic inversion with local power conservation for metasurface design," *IEEE Antennas Wirel. Propag. Lett.*, vol. 19, no. 8, pp. 1291–1295, 2020.

[31] T. Brown and P. Mojabi, "Cascaded metasurface design using electromagnetic inversion with gradient-based optimization," *IEEE Transactions on Antennas and Propagation*, vol. 70, no. 3, pp. 2033–2045, 2022.

[32] T. Brown, "Metasurface design using electromagnetic inversion," Ph.D. dissertation, University of Manitoba, Canada, 2020.

[33] V. G. Ataloglou, A. H. Dorrah, and G. V. Eleftheriades, "Design of compact huygens metasurface pairs with multiple reflections for arbitrary wave transformations," *IEEE Transactions on Antennas and Propagation*, 2020.

[34] C. L. Holloway, E. F. Kuester, and A. Dienstfrey, "Characterizing metasurfaces/metafilms: The connection between surface susceptibilities and effective material properties," *IEEE Antennas and Wireless Propagation Letters*, vol. 10, pp. 1507–1511, 2011.

[35] M. Dehmollaian, Y. Vahabzadeh, K. Achouri, and C. Caloz, "Limitations of the metasurface diluted-slab model," *IEEE Journal on Multiscale and Multiphysics Computational Techniques*, vol. 5, pp. 255–264, 2020.

[36] K. Achouri and C. Caloz, *Electromagnetic Metasurfaces: Theory and Applications*. Wiley-IEEE Press, 2021.

[37] M. Albooyeh, S. Tretyakov, and C. Simovski, "Electromagnetic characterization of bianisotropic metasurfaces on refractive substrates: General theoretical framework," *Annalen der Physik*, vol. 528, no. 9-10, pp. 721–737, 2016.

[38] X. Jia, Y. Vahabzadeh, C. Caloz, and F. Yang, "Synthesis of spherical metasurfaces based on susceptibility tensor gstcs," *IEEE Transactions on Antennas and Propagation*, vol. 67, no. 4, pp. 2542–2554, 2019.

[39] K. Achouri and O. J. F. Martin, "Angular scattering properties of metasurfaces," *IEEE Transactions on Antennas and Propagation*, vol. 68, no. 1, pp. 432–442, 2020.

[40] C. Simovski and S. Tretyakov, *An introduction to metamaterials and nanophotonics*. Cambridge University Press, 2020.

[41] K. Achouri, Y. Vahabzadeh, and C. Caloz, "Mathematical synthesis and analysis of a second-order magneto-electrically nonlinear metasurface," *Opt. Express*, vol. 25, no. 16, pp. 19 013–19 022, Aug 2017. [Online]. Available: http://opg.optica.org/oe/abstract.cfm?URI=oe-25-16-19013

[42] C. Caloz and Z.-L. Deck-Lger, "Spacetime metamaterialspart i: General concepts," *IEEE Transactions on Antennas and Propagation*, vol. 68, no. 3, pp. 1569–1582, 2020.

[43] M. Albooyeh, D.-H. Kwon, F. Capolino, and S. Tretyakov, "Equivalent realizations of reciprocal metasurfaces:role of tangential and normal polarization," *Physical Review B*, vol. 95, no. 115435, pp. 1–9, 2017.

[44] G. Lavigne, K. Achouri, V. S. Asadchy, S. A. Tretyakov, and C. Caloz, "Susceptibility derivation and experimental demonstration of refracting metasurfaces without spurious diffraction," *IEEE Transactions on Antennas and Propagation*, vol. 66, no. 3, pp. 1321–1330, 2018.

[45] V. S. Asadchy, M. S. Mirmoosa, A. Daz-Rubio, S. Fan, and S. A. Tretyakov, "Tutorial on electromagnetic nonreciprocity and its origins," *Proceedings of the IEEE*, vol. 108, no. 10, pp. 1684–1727, 2020.

[46] J. Kong, "Electromagnetic wave theory,. johnwiley & sons," *New York*, 1986.

[47] C. Pfeiffer and A. Grbic, "Millimeter-wave transmitarrays for wavefront and polarization control," *IEEE Transactions on Microwave Theory and Techniques*, vol. 61, no. 12, pp. 4407–4417, 2013.

[48] J. P. Wong, A. Epstein, and G. V. Eleftheriades, "Reflectionless wide-angle refracting metasurfaces," *IEEE Antennas and Wireless Propagation Letters*, vol. 15, pp. 1293–1296, 2015.

[49] T. Brown, Z. Liu, and P. Mojabi, "Full-wave verification of an electromagnetic inversion metasurface design method," in *2020 IEEE International Symposium on Antennas and Propagation and North American Radio Science Meeting*, 2020, pp. 971–972.

[50] A. Epstein and G. V. Eleftheriades, "Huygens metasurfaces via the equivalence principle: design and applications," *JOSA B*, vol. 33, no. 2, pp. A31–A50, 2016.

[51] M. Kelly, T. Brown, and P. Mojabi, "Toward an end-to-end metasurface design procedure for power pattern synthesis," in *2021 IEEE International Symposium on Antennas and Propagation and USNC-URSI Radio Science Meeting (APS/URSI)*, 2021, pp. 617–618.

[52] C. Niu and P. Mojabi, "A variational auto-encoder and transformer based approach for metasurface unit cell synthesis," in *2022 IEEE International Symposium on Antennas and Propagation and USNC-URSI Radio Science Meeting (APS/URSI)*, 2022, pp. 1–2.

[53] M. Chen, E. Abdo-Sánchez, A. Epstein, and G. V. Eleftheriades, "Theory, design, and experimental verification of a reflectionless bianisotropic huygens' metasurface for wide-angle refraction," *Physical Review B*, vol. 97, no. 12, p. 125433, 2018.

[54] P. Mojabi, N. Firoozy, N. Bayat, T. Brown, C. Narendra, P. Mojabi, C. Niu, T. Tiede, T. Neusitzer, X. Li, I. Jeffrey, J. LoVetri, and D. Barber, "Electromagnetic inversion for biomedical imaging, antenna characterization, and sea ice remote sensing applications," in *2016 URSI Asia-Pacific Radio Science Conference (URSI AP-RASC)*, 2016, pp. 586–589.

[55] P. Mojabi and J. LoVetri, "Microwave biomedical imaging using the multiplicative regularized Gauss-Newton inversion," *IEEE Antennas Wireless Propag. Lett.*, vol. 8, pp. 645–648, 2009.

[56] C. Narendra and P. Mojabi, "A combined inverse source and scattering technique for dielectric profile design to tailor electromagnetic fields," *IEEE Transactions on Antennas and Propagation*, vol. 70, no. 3, pp. 2149–2160, 2022.

[57] M. Phaneuf and P. Mojabi, "On the formulation and implementation of the loves condition constraint for the source reconstruction method," *IEEE Transactions on Antennas and Propagation*, vol. 70, no. 5, pp. 3613–3627, 2022.

[58] T. Brown, C. Narendra, C. Niu, and P. Mojabi, "On the use of electromagnetic inversion for near-field antenna measurements: A review," in *2018 IEEE Conference on Antenna Measurements Applications (CAMA)*, Sep. 2018, pp. 1–4.

[59] C. Narendra, T. Brown, and P. Mojabi, "Gradient-based electromagnetic inversion for metasurface design using circuit models," *IEEE Transactions on Antennas and Propagation*, vol. 70, no. 3, pp. 2046–2058, 2022.

[60] S. Schelkunoff, "Some equivalence theorems of electromagnetics and their application to radiation problems," *The Bell System Technical Journal*, vol. 15, no. 1, pp. 92–112, 1936.

[61] S. R. Rengarajan and Y. Rahmat-Samii, "The field equivalence principle: Illustration of the establishment of the non-intuitive null fields," *IEEE Antennas and Propagation Magazine*, vol. 42, no. 4, pp. 122–128, 2000.

[62] J. L. Araque Quijano and G. Vecchi, "Improved-accuracy source reconstruction on arbitrary 3-d surfaces," *IEEE Antennas and Wireless Propagation Letters*, vol. 8, pp. 1046–1049, 2009.

[63] R. F. Harrington, *Time-harmonic electromagnetic fields*. McGraw-Hill, 1961.

[64] W. C. Chew, J.-M. Jin, E. Michielssen, and J. Song, *Fast and Efficient Algorithms in Computational Electromagnetics*. Boston, USA: Artech House, 2006.

[65] P. C. Hansen, "Numerical tools for analysis and solution of Fredholm integral equations of the first kind," *Inverse Probl.*, vol. 8, pp. 849–872, 1992.

[66] T. Brown, I. Jeffrey, and P. Mojabi, "Multiplicatively regularized source reconstruction method for phaseless planar near-field antenna measurements," *IEEE Transactions on Antennas and Propagation*, vol. 65, no. 4, pp. 2020–2031, April 2017.

[67] C. Narendra and P. Mojabi, "Phaseless gauss-newton inversion for microwave imaging," *IEEE Transactions on Antennas and Propagation*, vol. 69, no. 1, pp. 443–456, 2021.

[68] M. Phaneuf, T. Qiu, and P. Mojabi, "On the importance of the love's condition for inverse equivalent-source metasurface design," in *2021 IEEE International Symposium on Antennas and Propagation and USNC-URSI Radio Science Meeting (APS/URSI)*, 2021, pp. 601–602.

[69] C. Niu, M. Kelly, and P. Mojabi, "An encoder-only transformer to generate power patterns from far-field performance criteria," in *2022 16th European Conference on Antennas and Propagation (EuCAP)*, 2022, pp. 1–4.

[70] A. Epstein and G. V. Eleftheriades, "Huygens' metasurfaces via the equivalence principle: design and applications," *J. Opt. Soc. Am. B*, vol. 33, no. 2, pp. A31–A50, Feb 2016.

[71] E. Polak and G. Ribiere, "Note sur la convergence de méthodes de directions conjuguées," *ESAIM: Mathematical Modelling and Numerical Analysis - Modélisation Mathématique et Analyse Numérique*, vol. 3, no. R1, pp. 35–43, 1969.

[72] T. Qiu, T. Brown, and P. Mojabi, "Choice of optimization parameters in an inverse metasurface design algorithm," in *2021 IEEE International Symposium on Antennas and Propagation and USNC-URSI Radio Science Meeting (APS/URSI)*, 2021, pp. 1449–1450.

[73] A. Epstein and G. V. Eleftheriades, "Synthesis of passive lossless metasurfaces using auxiliary fields for reflectionless beam splitting and perfect reflection," *Phys. Rev. Lett.*, vol. 117, p. 256103, Dec 2016. [Online]. Available: https://link.aps.org/doi/10.1103/PhysRevLett.117.256103

[74] V. G. Ataloglou and G. V. Eleftheriades, "Arbitrary wave transformations with huygens metasurfaces through surface-wave optimization," *IEEE Antennas and Wireless Propagation Letters*, vol. 20, no. 9, pp. 1750–1754, 2021.

[75] M. Phaneuf and P. Mojabi, "An integral equation approach to optimize surface waves for lossless and passive omega-bianisotropic Huygens' metasurfaces," in *2022 IEEE International Symposium on Antennas and Propagation and USNC-URSI Radio Science Meeting (APS/URSI)*, 2022, pp. 1–2.

[76] J. Budhu, L. Szymanski, and A. Grbic, "Design of planar and conformal, passive, lossless metasurfaces that beamform," *IEEE Journal of Microwaves*, vol. 2, no. 3, pp. 401–418, 2022.

[77] B. O. Raeker and A. Grbic, "Compound metaoptics for amplitude and phase control of wave fronts," *Physical Review Letters*, vol. 122, no. 11, p. 113901, 2019.

[78] M. Phaneuf and P. Mojabi, "An integral equation approach towards the design of compact metasurface pairs," in *2022 16th European Conference on Antennas and Propagation (EuCAP)*, 2022, pp. 1–4.

[79] J. Gohel, Z. Liu, and P. Mojabi, "A conjugate gradient algorithm with analytical expressions for compact metasurface pair design," in *2022 IEEE International Symposium on Antennas and Propagation and USNC-URSI Radio Science Meeting (APS/URSI)*, 2022, pp. 1–2.

[80] B. O. Raeker and S. M. Rudolph, "Arbitrary transformation of radiation patterns using a spherical impedance metasurface," *IEEE Transactions on Antennas and Propagation*, vol. 64, no. 12, pp. 5243–5250, 2016.

[81] J. W. Wu, Z. X. Wang, L. Zhang, Q. Cheng, S. Liu, S. Zhang, J. M. Song, and T. J. Cui, "Anisotropic metasurface holography in 3-d space with high resolution and efficiency," *IEEE Transactions on Antennas and Propagation*, vol. 69, no. 1, pp. 302–316, 2021.

[82] P. Mojabi and J. LoVetri, "Overview and classification of some regularization techniques for the Gauss-Newton inversion method applied to inverse scattering problems," *IEEE Transactions on Antennas and Propagation*, vol. 57, no. 9, pp. 2658–2665, Sept 2009.

[83] C. A. Balanis, *Antenna theory: analysis and design*, 4th ed. Hoboken: Wiley, 2016.

[84] Y. Rahmat-Samii, "Useful coordinate transformations for antenna applications," *IEEE Transactions on Antennas and Propagation*, vol. 27, no. 4, pp. 571–574, 1979.

Appendix A

Derivation of the 2D and 3D Forward Operators

First of all, consider a 2D ($\frac{\partial}{\partial z} = 0$) problem where the surface current densities exist on the x axis (currents are in fact on the xz plane but are invariant with respect to z). The currents are discretized as described in Section 4.4.1. The goal is then to create an operator $\mathbf{A}$ that maps the vector of unknown, $\mathbf{x}$, to E_z at the region of interest (ROI). According to (4.15), substituting the 2D Green's function, the electric field resulted from the z-polarized electric current source in the n^{th} unit cell can be expressed as

$$\boldsymbol{E}(\boldsymbol{r}) = -j\eta_0 k_0 \int_{\text{cell}_n} \frac{1}{4j} H_0^{(2)}\left(k_0|\boldsymbol{r}-\boldsymbol{r}'|\right)\hat{z}J_n f_n\left(\boldsymbol{r}'\right) + \frac{1}{k_0^2}\nabla\left(\nabla\cdot\frac{1}{4j}H_0^{(2)}\left(k_0|\boldsymbol{r}-\boldsymbol{r}'|\right)\hat{z}J_n f_n\left(\boldsymbol{r}'\right)\right)\mathrm{d}x', \quad \text{(A.1)}$$

where $H_0^{(2)}$ denotes the zeroth-order Hankel function of the second kind of. If the length of the n^{th} unit cell, l_n, is negligible[1] compared to $|\boldsymbol{r}-\boldsymbol{r}'|$, the equation above can be

[1] This is a reasonable approximation as l_n is typically in the order of $\lambda/6$ to $\lambda/10$.

approximated as

$$\boldsymbol{E}(\boldsymbol{r}) \approx -\hat{z}\frac{\eta_0 k_0 J_n l_n}{4} H_0^{(2)}\left(k_0\left|\boldsymbol{r}-\boldsymbol{r}_n'\right|\right) - \frac{\eta_0 J_n l_n}{4k_0}\nabla\left(\frac{\partial}{\partial z}H_0^{(2)}\left(k_0\left|\boldsymbol{r}-\boldsymbol{r}_n'\right|\right)\right), \tag{A.2}$$

where $\boldsymbol{r}_n'$ denotes the centroid of the n^{th} unit cell. Now the operator $\mathbf{A}_J$ can be created such that $\mathbf{A}_J\mathbf{J}$ produces a vector of electric field values due to the electric current source at the observation points. The elements of the matrix $\mathbf{A}_J$ can be calculated from the expression of the z component of the electric field at m^{th} testing point ($\boldsymbol{r}_m \in$ ROI) written as

$$E_{z,mn} = -\frac{\eta_0 k_0 J_n l_n}{4} H_0^{(2)}\left(k_0\left|\boldsymbol{r}_m-\boldsymbol{r}_n'\right|\right). \tag{A.3}$$

Similarly, the electric field due to the x-polarized magnetic current source in the n^{th} unit cell can be expressed as

$$\boldsymbol{E}(\boldsymbol{r}) = \int_{\text{cell}_n} \hat{x} M_n f_n\left(\boldsymbol{r}'\right) \times \nabla \frac{1}{4j} H_0^{(2)}\left(k_0\left|\boldsymbol{r}-\boldsymbol{r}'\right|\right) \mathrm{d}x', \tag{A.4}$$

which can be approximated as

$$\boldsymbol{E}(\boldsymbol{r}) \approx \hat{z}\frac{M_n l_n}{4j}\frac{\partial}{\partial y} H_0^{(2)}\left(k_0\left|\boldsymbol{r}-\boldsymbol{r}_n'\right|\right). \tag{A.5}$$

The z component of the electric field at m^{th} testing point due to the magnetic current source can then be calculated as

$$E_{z,mn} = -\frac{k_0 M_n l_n \left(y_m - y_n'\right)}{4j\left|\boldsymbol{r}_m-\boldsymbol{r}_n'\right|} H_1^{(2)}\left(k_0\left|\boldsymbol{r}_m-\boldsymbol{r}_n'\right|\right). \tag{A.6}$$

from which the operator $\mathbf{A}_M$ that maps the coefficients of the magnetic current density to E_z at ROI can be constructed. To create the operator $\mathbf{A}$ that acts on the unknown $\mathbf{x}$, first

a matrix $\mathbf{G}$ is formulated such that

$$\mathbf{Gx} = \begin{bmatrix} \mathbf{J} \\ \mathbf{M} \end{bmatrix}, \tag{A.7}$$

and the matrix $\mathbf{G}$ is created as

$$\mathbf{G} = \begin{bmatrix} \mathbf{I} & j\mathbf{I} & \mathbf{0} & \mathbf{0} \\ \mathbf{0} & \mathbf{0} & \mathbf{I} & j\mathbf{I} \end{bmatrix}, \tag{A.8}$$

where $\mathbf{I}$ denotes the $N \times N$ identity matrix and $\mathbf{0}$ denotes the $N \times N$ null matrix. Finally, the operator $\mathbf{A}$ is calculated as

$$\mathbf{A} = \begin{bmatrix} \mathbf{A}_J \\ \mathbf{A}_M \end{bmatrix} \mathbf{G}. \tag{A.9}$$

Notice that the second term in equation (A.2) is zero due to the 2D assumption. If the orientation of the 2D assumption is changed ($\frac{\partial}{\partial x} = 0$), equation (A.2) will become

$$\boldsymbol{E}(\boldsymbol{r}) = -\hat{z}\frac{\eta_0 k_0 J_n l_n}{4} H_0^{(2)}\left(k_0\left|\boldsymbol{r} - \boldsymbol{r}'_n\right|\right) + \frac{\eta_0 J_n l_n}{4}\nabla\left(\frac{z - z'_n}{|\boldsymbol{r} - \boldsymbol{r}'_n|} H_1^{(2)}\left(k_0\left|\boldsymbol{r} - \boldsymbol{r}'_n\right|\right)\right), \tag{A.10}$$

and the z component of the electric field can be calculated as

$$\begin{aligned} E_{z,mn} = &-\frac{\eta_0 k_0 J_n l_n}{4} H_0^{(2)}\left(k_0\left|\boldsymbol{r}_m - \boldsymbol{r}'_n\right|\right) + \frac{\eta_0 J_n l_n}{4}\frac{(z_m - z'_n)^2}{|\boldsymbol{r}_m - \boldsymbol{r}'_n|^3} H_1^{(2)}\left(k_0\left|\boldsymbol{r}_m - \boldsymbol{r}'_n\right|\right) \\ &+ \frac{\eta_0 k_0 J_n l_n}{8}\left(\frac{z_m - z'_n}{|\boldsymbol{r}_m - \boldsymbol{r}'_n|}\right)^2 \left(H_0^{(2)}\left(k_0\left|\boldsymbol{r}_m - \boldsymbol{r}'_n\right|\right) - H_2^{(2)}\left(k_0\left|\boldsymbol{r}_m - \boldsymbol{r}'_n\right|\right)\right). \end{aligned} \tag{A.11}$$

Now let us consider the 3D case, where the polarization at ROI is not necessarily $\hat{z}$ (for example, $\hat{\theta}$ component is specified and desired in Section 5.2). Using the same discretization scheme, the electric field caused by the z-polarized electric current source in the n^{th} unit

cell is calculated as

$$\boldsymbol{E}(\boldsymbol{r}) = -j\eta_0 k_0 \int_{\text{cell}_n} \frac{e^{-jk_0|\boldsymbol{r}-\boldsymbol{r}'|}}{4\pi|\boldsymbol{r}-\boldsymbol{r}'|}\hat{z}J_n f_n\left(\boldsymbol{r}'\right) + \frac{1}{k_0^2}\nabla\left(\nabla\cdot\frac{e^{-jk_0|\boldsymbol{r}-\boldsymbol{r}'|}}{4\pi|\boldsymbol{r}-\boldsymbol{r}'|}\hat{z}J_n f_n\left(\boldsymbol{r}'\right)\right)\mathrm{d}x'dz', \quad \text{(A.12)}$$

which can be approximated as

$$\boldsymbol{E}(\boldsymbol{r}) \approx -\hat{z}\frac{j\eta_0 k_0 J_n A_n e^{-jk_0|\boldsymbol{r}-\boldsymbol{r}'_n|}}{4\pi|\boldsymbol{r}-\boldsymbol{r}'_n|} - \frac{j\eta_0 J_n A_n}{4\pi k_0}\nabla\left(\frac{\partial}{\partial z}\frac{e^{-jk_0|\boldsymbol{r}-\boldsymbol{r}'_n|}}{|\boldsymbol{r}-\boldsymbol{r}'_n|}\right), \quad \text{(A.13)}$$

where A_n represents the area of the n^{th} unit cell. The calculation of the partial derivatives is rather tedious, but it could be accomplished using software like MATLAB. The electric field component values at m^{th} testing point are explicitly written as

$$E_{x,mn} = \frac{j\eta_0 J_n A_n\left(x-x'\right)\left(z-z'\right)\left(k_0^2|\boldsymbol{r}_m-\boldsymbol{r}'_n|^2 - 3jk_0|\boldsymbol{r}_m-\boldsymbol{r}'_n| - 3\right)e^{-jk_0|\boldsymbol{r}_m-\boldsymbol{r}'_n|}}{4\pi k_0|\boldsymbol{r}_m-\boldsymbol{r}'_n|^5}, \quad \text{(A.14a)}$$

$$E_{y,mn} = \frac{j\eta_0 J_n A_n\left(y-y'\right)\left(z-z'\right)\left(k_0^2|\boldsymbol{r}_m-\boldsymbol{r}'_n|^2 - 3jk_0|\boldsymbol{r}_m-\boldsymbol{r}'_n| - 3\right)e^{-jk_0|\boldsymbol{r}_m-\boldsymbol{r}'_n|}}{4\pi k_0|\boldsymbol{r}_m-\boldsymbol{r}'_n|^5}, \quad \text{(A.14b)}$$

$$E_{z,mn} = -\frac{j\eta_0 k_0 J_n A_n e^{-jk_0|\boldsymbol{r}_m-\boldsymbol{r}'_n|}}{4\pi|\boldsymbol{r}_m-\boldsymbol{r}'_n|} + \frac{j\eta_0 J_n A_n e^{-jk_0|\boldsymbol{r}_m-\boldsymbol{r}'_n|}}{4\pi k_0|\boldsymbol{r}_m-\boldsymbol{r}'_n|^5} \times\left(\left(z_m-z'_n\right)^2\left(k_0^2\left|\boldsymbol{r}_m-\boldsymbol{r}'_n\right|^2 - 3jk_0\left|\boldsymbol{r}_m-\boldsymbol{r}'_n\right| - 3\right) + jk_0\left|\boldsymbol{r}_m-\boldsymbol{r}'_n\right|^3 + \left|\boldsymbol{r}_m-\boldsymbol{r}'_n\right|^2\right). \quad \text{(A.14c)}$$

Similarly, if x-polarized magnetic current source exists in the n^{th} unit cell, the corresponding electric field can be calculated as

$$\boldsymbol{E}(\boldsymbol{r}) = \int_{\text{cell}_n}\hat{x}M_n f_n\left(\boldsymbol{r}'\right)\times\nabla\frac{e^{-jk_0|\boldsymbol{r}-\boldsymbol{r}'|}}{4\pi|\boldsymbol{r}-\boldsymbol{r}'|}\mathrm{d}x'\mathrm{d}z', \quad \text{(A.15)}$$

and then the electric field can be approximated as

$$\boldsymbol{E}(\boldsymbol{r}) \approx \hat{x}\frac{M_n A_n}{4\pi} \times \nabla \frac{e^{-jk_0|\boldsymbol{r}-\boldsymbol{r}'_n|}}{|\boldsymbol{r}-\boldsymbol{r}'_n|}. \tag{A.16}$$

At the m^{th} testing point, the electric field components due to magnetic current source can be explicitly expressed as

$$E_{x,mn} = 0, \tag{A.17a}$$

$$E_{y,mn} = \frac{M_n A_n \left(z_m - z'_n\right)\left(jk_0|\boldsymbol{r}_m - \boldsymbol{r}'_n| + 1\right) e^{-jk_0|\boldsymbol{r}_m-\boldsymbol{r}'_n|}}{4\pi|\boldsymbol{r}_m - \boldsymbol{r}'_n|^3}, \tag{A.17b}$$

$$E_{z,mn} = -\frac{M_n A_n \left(y_m - y'_n\right)\left(jk_0|\boldsymbol{r}_m - \boldsymbol{r}'_n| + 1\right) e^{-jk_0|\boldsymbol{r}_m-\boldsymbol{r}'_n|}}{4\pi|\boldsymbol{r}_m - \boldsymbol{r}'_n|^3}. \tag{A.17c}$$

Alternatively, the 3D operator can be derived in a more elegant way by considering each unit cell containing infinitesimal electric and magnetic dipoles. At the m^{th} testing point, the electric field components (in the spherical coordinate) caused by z-polarized infinitesimal electric dipole at centroid of the n^{th} unit cell having a electric moment of $J_n A_n$ are given as [83]

$$E_{r,mn} = \frac{\eta_0 J_n A_n \cos\theta}{2\pi|\boldsymbol{r}_m - \boldsymbol{r}'_n|^2}\left(1 + \frac{1}{jk_0|\boldsymbol{r}_m - \boldsymbol{r}'_n|}\right) e^{-jk_0|\boldsymbol{r}_m-\boldsymbol{r}'_n|}, \tag{A.18a}$$

$$E_{\theta,mn} = \frac{j\eta_0 k_0 J_n A_n \sin\theta}{4\pi|\boldsymbol{r}_m - \boldsymbol{r}'_n|}\left(1 + \frac{1}{jk_0|\boldsymbol{r}_m - \boldsymbol{r}'_n|} - \frac{1}{\left(k_0|\boldsymbol{r}_m - \boldsymbol{r}'_n|\right)^2}\right) e^{-jk_0|\boldsymbol{r}_m-\boldsymbol{r}'_n|}, \tag{A.18b}$$

$$E_{\phi,mn} = 0, \tag{A.18c}$$

where $\boldsymbol{r}'_n$ is used as the origin when measuring θ. Similarly, for a *z-polarized* infinitesimal magnetic dipole with magnetic moment of $M_n A_n$, the electric field components are calculated as

$$E_{r,mn} = 0, \tag{A.19a}$$

$$E_{\theta,mn} = 0, \tag{A.19b}$$

$$E_{\phi,mn} = -\frac{jk_0 M_n A_n \sin\theta}{4\pi|\boldsymbol{r}_m - \boldsymbol{r}'_n|}\left(1 + \frac{1}{jk_0|\boldsymbol{r}_m - \boldsymbol{r}'_n|}\right) e^{-jk_0|\boldsymbol{r}_m - \boldsymbol{r}'_n|}. \tag{A.19c}$$

To calculate the electric field due to a *x-polarized* infinitesimal magnetic dipole, one can apply the concept of Euler angles [84] to transform the values under local coordinate (z-polarized dipoles) to values under global coordinate (x-polarized dipoles). For this specific case, the Euler angles (not the unique combination) in radians are

$$\alpha = 0,\ \beta = -\frac{\pi}{2},\ \gamma = -\frac{\pi}{2}, \tag{A.20}$$

where α indicates the amount of first counterclockwise rotation that is about z axis, β indicates the amount of second counterclockwise rotation that is about x axis, and γ indicates the amount of third counterclockwise rotation that is about z axis. The Cartesian components of the electric field due to a x-polarized infinitesimal magnetic dipole can be then calculated as

$$\mathbf{E}^g = \left({}^g\mathbf{T}^l\right)\mathbf{E}^l, \tag{A.21}$$

where $\mathbf{E}^l$ is the vector containing the Cartesian components of the electric field due to a z-polarized infinitesimal magnetic dipole that can be easily derived from equation (A.19), $\left({}^g\mathbf{T}^l\right)$ is the transformation matrix from the local coordinate to the global coordinate calculated as

$$\left({}^g\mathbf{T}^l\right) = \begin{pmatrix} \cos\gamma & \sin\gamma & 0 \\ -\sin\gamma & \cos\gamma & 0 \\ 0 & 0 & 1 \end{pmatrix} \begin{pmatrix} 1 & 0 & 0 \\ 0 & \cos\beta & \sin\beta \\ 0 & -\sin\beta & \cos\beta \end{pmatrix} \begin{pmatrix} \cos\alpha & \sin\alpha & 0 \\ -\sin\alpha & \cos\alpha & 0 \\ 0 & 0 & 1 \end{pmatrix}. \tag{A.22}$$

Comparing to the first approach that deriving the operator straight from EFIE, this approach is more convenient. Moreover, the use of Euler angles could be easily extended to

deal with arbitrarily shaped metasurfaces where the polarization of the equivalent sources are location-dependent.